Ultrafast Laser Spectroscopy of Perovskite Solar Cells

Efthymios D. Serpetzoglou

Advisory Committee
Stratakis Emmanuel, *Research Director, IESL-FORTH, University of Crete* (**Supervisor**)
Charalambidis Dimitris, *Prof. University of Crete* (**Co-Supervisor**)
Costas Fotakis, *Prof. University of Crete*

Advisory Committee
Stratakis Emmanuel, *Research Director, IESL-FORTH, University of Crete* (**Supervisor**)
Charalambidis Dimitris, *Prof. University of Crete* (**Co-Supervisor**)
Costas Fotakis, *Prof. University of Crete*
Kioseoglou George, *Prof. University of Crete*
Kymakis Emmanuel, *Prof. Hellenic Mediterranean University*
Iliopoulos Eleftherios, *Assoc. Prof. University of Crete*
Rakitzis Theodore-Peter, *Prof. University of Crete*

Department of Physics
University of Crete

This dissertation is submitted for the degree of Doctor of Philosophy
February 2020

Dedication

To my parents

Table of Contents

Acknowledgements

First of all, I would like to express my sincere and heartily gratitude to Dr. Emmanuel Stratakis for his continuous support of my Ph.D. research, for his guidance, encouragement, patience and enthusiasm. His guidance and motivation were very important and crucial to the completion of this doctoral thesis throughout its duration. He has also supported me with his immerse knowledge, allowing me to work in on my way, while at the same time showing me how to increase my productivity. He really knows how to improve and keep my performance to the highest possible level. Since the relationship with your advisor is vital for a successful Ph.D., I wish any individual and new Ph.D. candidate to be blessed enough to have a mentor like him.

Moreover, I also want to express my special appreciation and thanks to my advisors, Prof. Dimitris Charalambidis and Prof. Costas Fotakis for giving me access to the laboratory and research facilities. Without his support, it would not be possible to conduct this research.

Besides my advisor, I would like to thank Dr. Ioannis Konidakis, for his daily help, guidance, perseverance, encouragement and motivation he showed to me, for the greatest possible result and his effort to solve any issue and query throughout my Ph.D. thesis.

Furthermore, I would like to thank our collaborators, Prof. Emmanuel Kymakis from Department of Electrical & Computer Engineering of the Hellenic Mediterranean University, Prof. George Kioseoglou from Department of Materials Science and Technology of the University of Crete, Dr. Christos Chochos from National Hellenic Research Foundation, Prof. Thomas Anthopoulos from Material Science Engineering at Kaust Solar Center, and finally Dr. Petra Pötschke from Functional Composites and Blends of the Leibniz Institut.

I want to heartily thanks the member of the committee of my thesis Prof. Eleftherios Iliopoulos and Prof. Peter Rakitzis, for doing me the honor of evaluating my Ph.D. thesis.

A special thanks to my parents. Words cannot express how grateful I am to my loving father, and my mother for all the sacrifices that they have made on my behalf and for their spiritual support in my life in general and encouragement to reach my goal.

I thank my fellow labmates and my colleagues in my office for being patient with me and for all the fun we have had. Special thanks to my friends Myron Krassas, George Kourmoulakis, Evangelia Gavgiotakis, Ioannis Paradisanos, Apostolis Panagiotopoulos, Vasilios Tsafas, Nikos Korakas, Evangelos Skoulas, Paraskevi Kavatzikidou, Andreas Lemonis, Eleftheria Babaliari, Ioanna Demeridou, Kyriaki Savva and Stella Maragkaki for all the amazing moments we have spent during these five years.

Abstract

During the last two decades, organic and inorganic lead halide perovskites have attracted tremendous scientific attention due to the extraordinary optical properties and their potential employment in various types of state-of-the-art applications, such as next-generation solar cells (PSCs), light-emitting diodes, lasers, etc. The continuous challenge for solar cells in particular, is to optimize the performance while at the same time improve the stability. In order to address both challenges, the roles of the crystalline quality of the perovskite absorber film, as well as the carrier transport and the recombination processes, between the perovskite absorber and the carrier transport layers, should be understood. Particularly, the physical mechanisms of carrier transport between the perovskite active layer and the hole transport layer (HTL), which is the layer that collects the holes, as well as the electron transport one (ETL), which is the layer that collects the electrons.

In this thesis, we shed light on such physical mechanisms by means of femtosecond time-resolved absorption spectroscopy. In particular, it is shown that the photo-excited carrier dynamics are strongly correlated with the surface properties of the employed transport layer as well as with the electrical characteristics of the devices. Furthermore, the charge carrier dynamics are monitored, in-situ, in order to observe their evolution during the perovskite absorber crystallization process in various temperatures, from 85 K up to 250 K, and extract useful information about the effect of the crystal structure on the carrier transport properties.

It is envisaged that the novel findings of this thesis could help to a better understanding of the physical phenomena that take place in PSCs after photoexcitation, with the ultimate aim to further enhance the device efficiency, while at the same time to improve the stability.

List of Figures

List of Tables

Preamble

Organic and inorganic lead halide perovskite have attracted tremendous scientific attention due to their potential for being the main component of next generation photovoltaic technology. Much of this attention originates from their outstanding properties, namely, the medium optical bandgap and strong absorption coefficients and the long carrier diffusion lengths, as well as, the low recombination losses and bandgap tunability. While the efficiency of perovskite solar cells has extremely increased in the last 5 years, from ~14% up to 26.7%, the major challenge for this type of solar cells, before they can really take over the silicon photovoltaic technology in the global industry, is to optimize the performance, while at the same time improve the stability.

A variety of single methylammonium lead halide perovskite absorbers of the formula $CH_3NH_3PbX_3$ have been employed, as well as, various mixed halide structures based on the same formula in which a second inorganic anion is introduced, i.e. $CH_3NH_3PbI_{3-x}X_x$, where X is Cl or Br. Moreover, many groups have focused in the importance of the fabrication procedures, such as one-step and two-step deposition protocols, crystal formation via solution and vapor deposition processes, and rapid laser annealing crystallization techniques. Additionally, notable attention has been paid on the selection of suitable hole transport layer (HTL) and electron transport layer (ETL) conductive materials, in order to enhance the efficiency while improving device lifetime.

Despite the strong efforts of the research community, there is still significant lack of understanding of the carrier transport phenomena that take place in PSCs after photoexcitation. Furthermore, there is no clear evidence on how the nature of the carrier

transport layers influences the crystallization of the perovskite film and the device performance and stability.

In this thesis, we probe the charge carrier transport and recombination processes of the perovskite film by means of femtosecond transient absorption spectroscopy (TAS). In particular, we monitor the excited carrier dynamics upon using two different HTL polymers, namely the super hydrophilic polymer poly (3,4-ethylenedioxythiophene)-poly (styrenesulfonate), known as PEDOT:PSS, and the non-wetting poly (triarylamine) semiconductor polymer, known as PTAA. Furthermore, we monitored, in-situ, the charge carrier dynamics during the perovskite layer crystallization process for two different hole transporting materials. Both approaches shed light on the effect of the transport layer properties on the perovksite crystallization process, the charge carrier dynamics, as well as the device electrical characteristics. Finally, we explored the carrier dynamics through temperature dependent TAS measurements, in order to understand how the different perovskite crystal structure is correlated with the carrier transport and recombination.

In **Chapter 1** of this thesis an introduction in energy production and consumption needs is presented, while the evolution of the solar cells and their electrical characteristics of the photovoltaics are reviewed. In the last section, an extended introduction to the wonderful world of the perovskite materials and their extraordinary properties are presented.

In **Chapter 2**, the introduction to the ultrafast TAS is presented. Moreover, the fundamental insights of this technique are described and the components of the set-up designed and built for the TAS measurements are shown. Finally, the state-of-the-art benefits of using this technique in the field of the PSCs is described.

In **Chapter 3**, the sample preparation protocols for the samples tested are summarized. In addition, the optical characterization techniques, such as the micro-photoluminescence (μ-PL) and the ultraviolet-visible (UV-Vis) absorption spectroscopy are explained. Finally, the characterization of the perovskite crystal structure and the measurements setups used for the devices electrical properties are presented

In **Chapter 4**, we investigate the carrier transport properties of PSCs by means of femtosecond time-resolved transient absorption spectroscopy (TAS). Using this study, we elucidate for the first time the mechanism behind the PSCs efficiency enhancement upon the use of a hole transport layer (HTL) with reduced hydrophilicity. It is evidenced that there is a unique correlation of carrier relaxation dynamics with the structural morphology of the HTL and the electrical characteristics of the devices.

In **Chapter 5**, we monitored, in-situ, for the first time, the evolution of the charge carrier dynamics during the thermal annealing crystallization process of the perovskite absorber, by means of time-resolved femtosecond TAS. It is evidenced that the thermal annealing time required for the formation of perovskite films with optimum charge extraction dynamics strongly depends on the nature of the employed HTL. More important, our results reveal that TAS is a powerful technique towards the identification of the best quality perovskite film (optimum crystallization period at specific temperature).

In **Chapter 6**, we investigate the charge carrier dynamics of PSCs with femtosecond time-resolved transient absorption spectroscopy upon two different hole transport layers in two different perovskite crystal phases. It is revealed that the charge carrier dynamics and the

recombination rates are strongly affected from the temperature, the pervoskite crystal phase and from the employing hole transport layer

Finally, **Chapter 7** contains the future plans of this Ph.D. thesis.

Chapter 1

Energy and Perovskite Solar Cells

In the first part of this Chapter, a brief introduction of the global energy consumption and the necessity for green energy production of renewable sources is presented. Subsequently, the development of the photovoltaic technologies, the device architecture, the principles of device operation, as well as the introduction to wonderful world of the perovskite materials are reviewed.

1.1 Energy Consumption and Production

As the world population rises, the global energy consumption is also increased. The estimation of the world population up to 2050 would to be around 9.5 billion people.[1] Due to this significant increase of world population, the energy consumption is excepted to boost up to around 800 quadrillion British thermal units (1quadrillion Btu = 2.93×10^{11} kWh) by the end of 2040.[2] The fossil fuel occupying the 80% of the world energy consumption[3] and while they are cheap and reliable sources of energy, contribute to the global warming and also, they are non-renewable and unsustainable.[4] For this reason, the necessity for a new type of energy, like renewable energy, is imperative to diminish the carbon emissions that are responsible for global temperature increase. To limit global temperature to a hypothetical 2 °C rise would demand a 70% decline in carbon emissions in industrial countries by 2050.[5] Thus, last decades the renewable sources have attracted considerable attention in order to replace the fossil fuels and to reduce the carbon dioxide emissions.[5]

The sun is the most abundant, clean and accessible renewable source. A year's worth of sun irradiation contains 1.5×10^{18} kWh of energy and cover a range of wavelength form 250 nm (ultraviolet – UV) up to 2500 nm (infrared – IR) as shown in **Figure 1.1**. By comparison, the energy of oil, coal, and gas which are 1.75×10^{15} kWh, 1.4×10^{15} kWh, and 5.5×10^{15} kWh, respectively, a year of sunlight irradiation provides more than a hundred times the energy of the world's entire known fossil fuel reserves.[6] While, the solar energy is enough to cover annual global consumption for a year, the difficulty exists in converting solar energy into electricity in an efficient and cost-effective way. The most promising technology for direct converting the photons to electricity is the photovoltaic solar cells. Nevertheless, in order this technology to become competitive with fossil fuels and to play an important role of the electricity market, it is crucial to reduce the cost of the solar cells or to enhance their power conversion efficiencies.

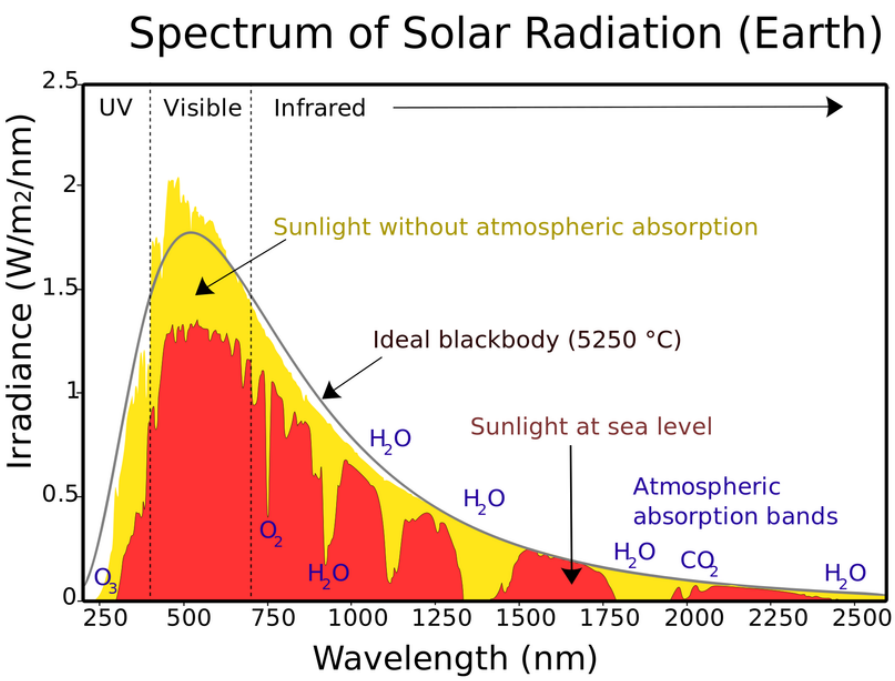

Figure 1.1: Solar Radiation Spectrum from 250 nm up to 2500 nm.[7]

1.2 Development of Solar Cells

The photovoltaic phenomenon was discovered from Alexandre-Edmond Becquerel,[8,9] a French physicist in 1839, while experimenting with an electrolytic cell consisting of two metal electrodes in conductive liquid. This phenomenon is the conversion of solar radiation into electricity. Namely, the explanation of the phenomenon is based on the quantum matter theory. The light consists of energy packs, the photons, the energy of which depends only on the frequency or the color of the light. The photon energy of the visible spectrum is sufficient to excite the electrons at higher energy levels, where they are able to contribute to the conductivity of the material.

Approximately half a century later in 1883, Charles Fritts developed the first solar cell. Fritts coated the semiconductor material selenium (Se) with an extremely thin layer of gold. The resulting cells had efficiency less than 1%. Since the first solar cell, the evolution of the photovoltaic technology was huge and is parted in three generations.

The first generation (1G) solar cells are large scale, single junction devices. The majority of the 1G solar cells are based on silicon wafers, including single crystal and multi-crystalline silicon (**Figure 1.2**). Nowadays, the 90% of the photovoltaics are based on first generation solar cells. The theoretical limit of the efficiency of the single junction cells is about 30% (the Shockley–Queisser limit);[10,11] at present, the common silicon wafer based devices show almost 20% efficiency with the highest reported efficiencies reaching 25%.[12] A crucial drawback of this technology is the high cost per produced Watt, that is around 4 times higher than other convention energy sources prices, due to the high cost of the materials that used (half of the cost of 1G devices is the silicon wafer), and high manufacturing and processing expenses. Even though, the cost of the 1G devices is decreasing along with the progress of

the technology, this generation of solar cells will probably reach their price limit before achieving the competitive level in the market.

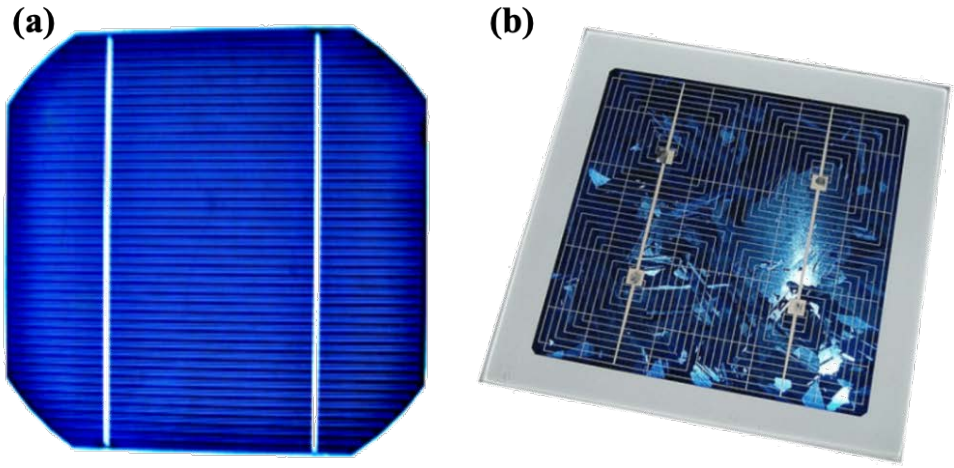

Figure 1.2: (a) Mono-crystalline PV cell, (b) Poly-crystalline PV cell.[13]

The second generation (2G) solar cells have been developed to address the energy requirements, while at the same time to decrease the amount of expensive materials that used and to keep the efficiency of the devices high. Alternative techniques have been employed for the production process, such as vapour deposition, solution deposition, electroplating, etc. The principal approach of this generation of solar cells has been to produce thin film solar cells on low cost substrates, such as glass and flexible substrates, i.e. PET. The most successful materials for 2G solar cells have been cadmium telluride/selenide (CdTe/CdS), copper indium gallium selenide (CIGS) and amorphous silicon, that are being deposited on thin substrates (**Figure 1.3**). The 2G solar cells can reach lab efficiency up to 19%, but the module can reach efficiencies up to 14%, due to the difficulties in producing large-scale uniform films.[12] Although the thin film technology can notable decrease the PVs fabrication cost, 2G solar cells will be constrained by certain cost ceilings per watt due to efficiency limits and the material costs.

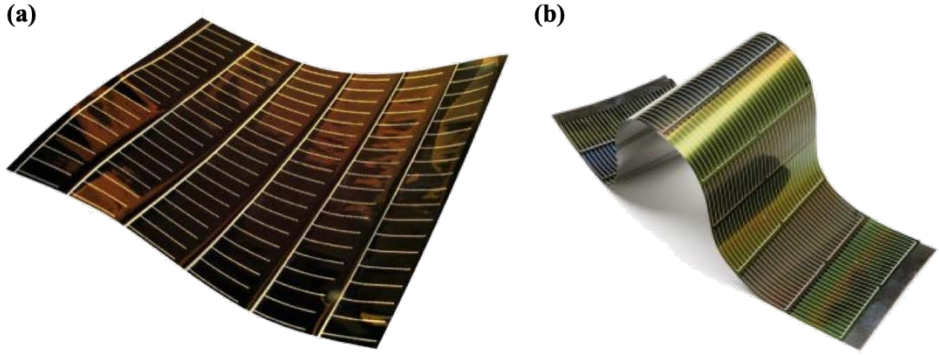

Figure 1.3: (a) CdTe Solar Panel,[14] (b) CIGS Solar Panel.[15]

The third generation (3G) solar cells have been developed to achieve high-efficiency devices by multiple stacking (sandwich), using thin-film, second generation deposition methods.[16] The idea was to do this with only a small increase of active area of the devices, resulting to harvest more photons and even overcome the Shockley-Queisser limit of 30%, and hence reduce the cost. Currently the highest efficiencies reported for multi-junction solar cells are over 33%, with the record for four-junction or more multi-junction solar cells to be 46%.[17] New device architectures and materials have been developed in this generation of solar cells. Namely, three typical approaches of 3G photovoltaics are the Dye-Sensitized Solar Cells (DSSCs),[18-20] Organic Photovoltaics (OPVs)[21,22] and Perovskite Solar Cells (PSCs).[23-25] A dye-sensitized solar cell, also known as Grätzel cell, is based on a combination of dyes with metal oxides and electrolyte, photoelectrochemical system. The efficiency of DSSCs is around 12% (**Figure 1.4**), with the highest record of the efficiency to be 12.6%,[17] while the lifetime of the devices is low compared with the inorganic solar cells. Moreover, the DSSC use liquid electrolyte which at low temperatures can freeze, halting power production and possibly leading to physical damage, while at higher temperatures, the liquid can expand, making sealing the panels a serious problem. Another disadvantage that expensive ruthenium (dye), platinum (catalyst) and conducting glass or plastic are required to produce a DSSC. A

third crucial drawback is that the electrolyte solution contains volatile organic compounds (or VOC's), solvents which are hazardous to human health and the environment and must be carefully sealed, because infiltrate plastics, and be prohibited for outdoor panels without robust encapsulation.[26]

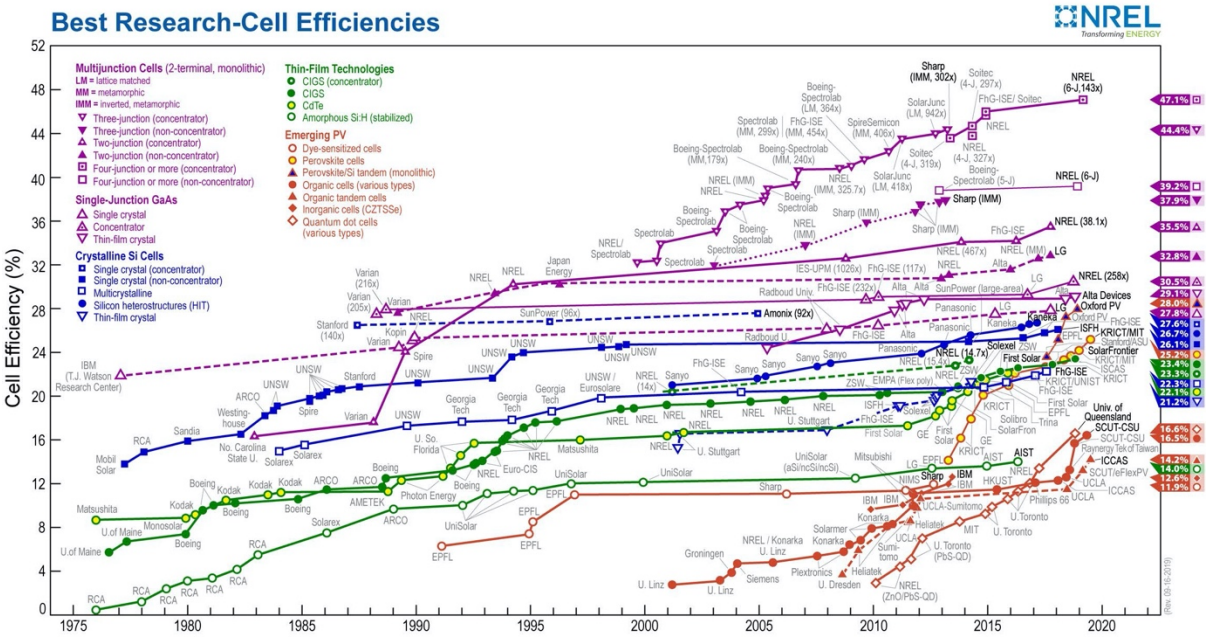

Figure 1.4: The chart with the best research-cell efficiencies for all photovoltaic generations.[17]

The OPV technology is based on organic compound, such as conjugated polymers and fullerenes, blended forming heterojunctions in the nanoscale. The efficiency of the OPVs has overcome the 10%,[17] using simple deposition techniques and low cost fabrication materials. The OPVs are flexible, semitransparent and eco-friendly devices. On the other hand, while the theoretical Shockley-Queisser limit for an optimum p-n junction solar cell is 30% with an optimum band gap of 1.1 eV, the record up to now is 16.6% (**Figure 1.4**) and the proposed maximum efficiency to be ~20%.[27] The main limitations are due to the narrow absorption, reduced charge carrier transport and mobility, and high recombination resulting to voltage

losses. The key in order to improve the efficiency is to avoid the non-radiative recombinations.[27]

Finally, for the PSCs the perovskite material operates as light absorber, and is deposited between the electron transport layer (ETL) and the hole transport layer (HTL), as shown in **Figure 1.5**. The power conversion efficiency (PCE) of the PSCs has already exceeding more than 20%, with the highest record to be 26.7% (**Figure 1.4**)[17] because the hybrid perovskite exhibits ambipolar carrier transport and long carrier lifetime. This architecture offers the advantages of simplified device configuration and facile fabrication. There are two types of planar architectures, the normal structure and the inverted structure (**Figure 1.5**). For the latter, the illumination takes place from the p-type side (glass/ITO/HTL/perovskite/ETL/metal) while for the normal structure the illumination takes place form the n-type side (glass/ITO/ETL/perovksite/HTL/metal).

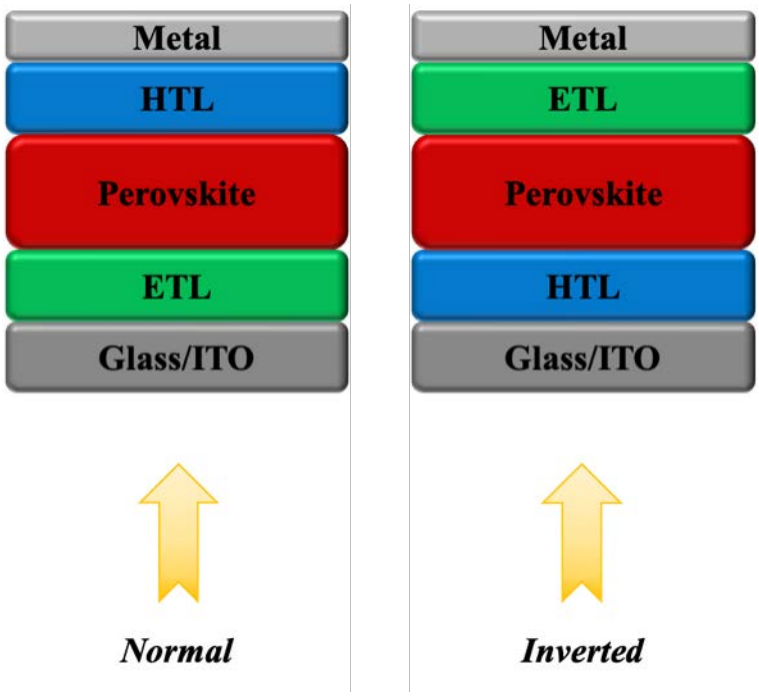

Figure 1.5: The schematic diagram of normal and inverted PSC device architectures. The arrow indicated the direction of the incident light.

On the contrary, these solar cells have many degradation issues of the perovskite layer due to the humidity, oxygen, light exposure and heat. Moreover, the film quality and thickness, as well as the interaction between the perovskite film and the transport layers are also crucial parameters improving the efficiency and stability of the devices. In order to overcome the drawbacks and to further increase the performance and improve the stability of the PSCs, is necessary to study and fully understand the ultrafast mechanisms that take place in these devices after photoexcitation; how they are affected by the transport layers and how these processes affect the efficiency and stability of the perovskite solar cells, which is the main objective of this Ph.D. thesis.

1.3 Principles of Photovoltaic Effect

In perovskite solar cells, the absorber layer is "sandwiched" between the ETL and HTL, for more efficient charge collection from the electrodes. More specifically, in **Figure 1.6** are depicted the five main mechanisms that take place in an inverted perovskite solar cell in order to convert the solar radiation to the electricity. Firstly, the light is absorbed from the perovskite and we have the exciton formation (1). Subsequently, the excitons are disrupted into free charges (2) and then the free carriers are diffused in the active layer in order to approach the interfaces between the transport layers and the perovskite (3). Finally, the carriers are injected in the appropriate layer (4). In particular, the holes are injected in the HTL and the electrons in the ETL and then, we have the free carriers' collection by the respective electrodes (5).[28]

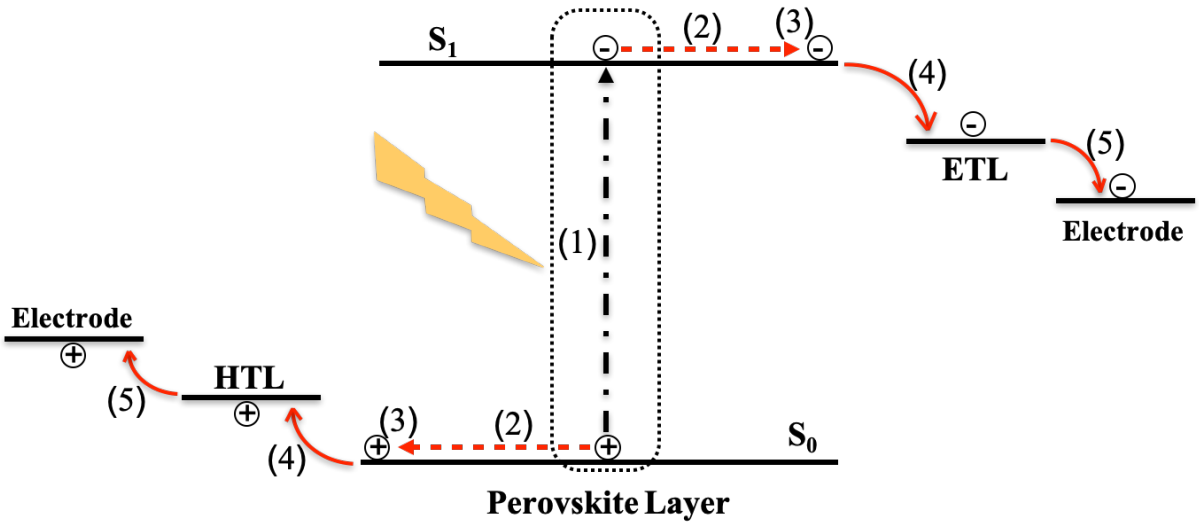

Figure 1.6: The energy conversion mechanism in an inverted perovskite solar cell.

The injection of the free carriers to the appropriate transport layer happening due to the energy alignment of ETL and HTL with the conduction band (CB or S_1) and the valence band (VB or S_0) of the perovskite, respectively. As a result, the electrons are injected to the anode, while the holes to the cathode, generating a current and a potential difference, which can be harnessed into electricity. In the devices of this thesis, indium tin oxide (ITO) was used as anode while aluminium is used as cathode. In order to reduce the carrier recombination at the interfaces, which affect to the open circuit voltage (V_{OC}), the ETL and HTL should be compact and not being heavily doped. Thus, both organic and inorganic materials have been identified that are suitable for charge transport layer (ETL and HTL), that are used for developing efficient perovskite solar cells (**Figure 1.7**).[29]

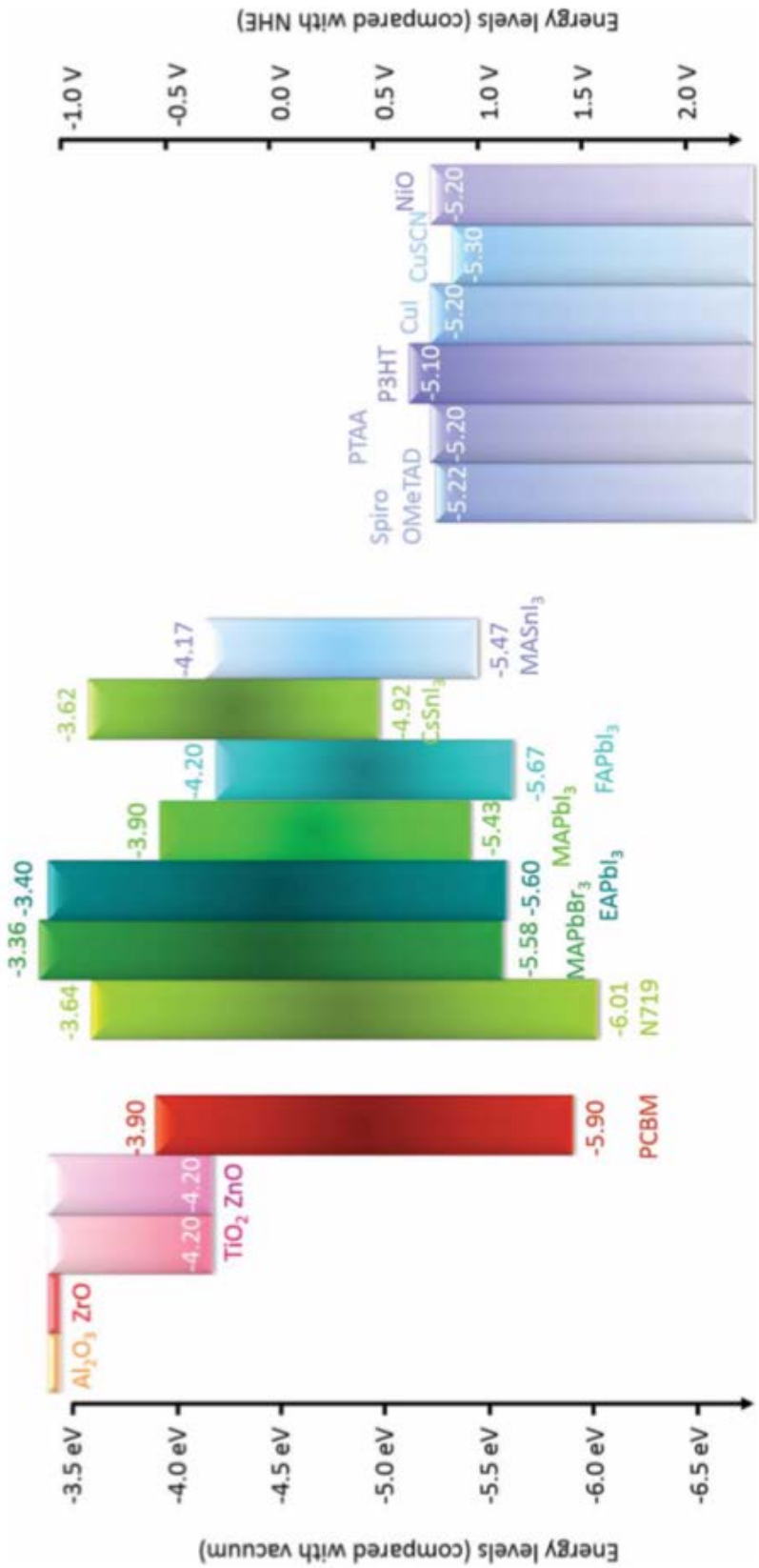

Figure 1.7: Energy levels for different electron transport layers (ETL) (left), absorbers (middle) and hole transport layers (HTL) (right) that used in the perovskite solar cells. Figure is taken from reference 29.

1.4 Electrical Parameters

Generally, a solar cell is a device that converts the solar radiation to the electricity. The power output under illumination is achieved by the ability of the photovoltaic device to generate voltage to an external load and current through the load at the same time. This is characterized by the cell-current (I-V) curve of the cell at certain lighting and temperature as depicted in **Figure 1.8**

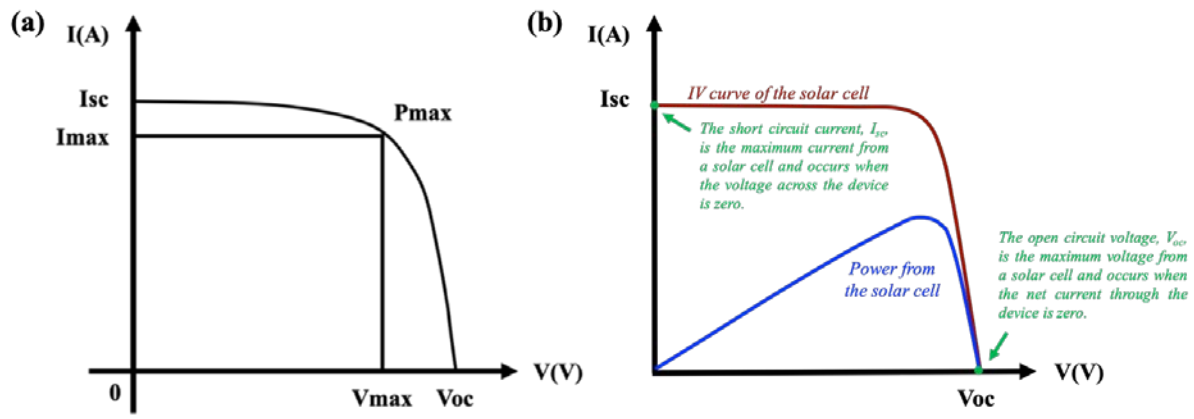

Figure 1.8: (a) The I-V curve of the solar cell and its maximum power, **(b)** Schematic of I-V curve of as solar cell showing the I_{SC}, V_{OC}.

The most important parameters for a solar cell in order to evaluate its performance are the Open Circuit Voltage (V_{OC}), Short Circuit Current (I_{SC}) and Power Conversion Efficiency (PCE) and are depicted in **Figure 1.8(b)**.[30] More specifically:

- **Open Circuit Voltage (V_{OC})**

The open-circuit voltage, V_{OC}, is the maximum voltage available from a solar cell, and this occurs at zero current. The open-circuit voltage corresponds to the amount of forward bias on the solar cell due to the bias of the solar cell junction with the light-generated current.[30] The equation for the V_{OC} is:

$$V_{OC} = \frac{nkT}{q}\frac{I_L}{I_0} ln(\frac{I_L}{I_0} + 1) \quad (1.1)$$

where, n is the carrier density, k is the Boltzmann's constant, T is the temperature, q is the electronic charge, I_L is the light generated current and I_0 is the reverse saturation current.

- **Short Circuit Current (I_{SC})**

The short-circuit current is the current through the solar cell when the voltage across the solar cell is zero (i.e., when the solar cell is short circuited). The equation for the I_{SC} is:

$$\boldsymbol{I_{SC} = qG(L_n + L_p)} \quad \textit{(1.2)}$$

where G is the generation rate, and Ln and Lp are the electron and hole diffusion lengths respectively.[30]

- **Fill Factor (FF)**

The FF is defined as the ratio of the maximum power from the solar cell to the product of V_{OC} and I_{SC}:

$$\boldsymbol{FF = \frac{P_{MAX}}{V_{OC} \times I_{SC}} = \frac{V_{MAX} \times I_{MAX}}{V_{OC} \times I_{SC}}} \quad \textit{(1.3)}$$

The FF describes the quality of the solar cell, i.e measure the "squareness" of the solar cell and is also the area of the largest rectangle which will fit in the IV curve.[30]

- **Power Conversion Efficiency (PCE)**

The efficiency of the solar cell is determined as the fraction of incident power that is converted to electricity and is defined as:

$$\boldsymbol{PCE = \frac{P_{MAX}}{P_{in}} = \frac{V_{OC} \times I_{SC} \times FF}{P_{in}}} \quad \textit{(1.4)}$$

1.5 Perovskite Solar Cells

In this Section, the history of the wonderful world of perovskite crystals, as well as the crystal structure and the optical and electronic properties of such materials are discussed.

1.5.1 Crystal Structure and Optoelectronic Properties

The term 'Perovskite' originates from the discovery of $CaTiO_3$ in the Ural Mountains of Russia by Gustav Rose in 1939 and is named after Russian mineralogist Lev Perovski. Later, many materials with the same crystal structure were discovered with two notable cases being $SrTiO_3$ and $BaTiO_3$. Perovskite presents AMX_3 crystals, where A is a cation ($CH_3NH_3^+$ or Cs^+ or Rb^+ or FA^+), M is a metal cation (Pb^{2+} or Sn^{2+} or Ge^{2+}) and X is an oxide or a halide anion (I^- or Cl^- or Br^-). The perovskite structure is extended in a three-dimensional network formed by an MX_6 corner-sharing octahedron. These materials are the archetypal systems for phases transitions with accessible cubic, tetragonal, orthorhombic, trigonal and monoclinic polymorphs depending on the tilting and rotation of the MX_3 polyhedra in the lattice.[31] The perovskites can self-assembly into zero-dimensional (0D), one-dimensional (1D), two-dimensional (2D) or three-dimensional (3D) structures (**Figure 1.9**); this process depends on the structure of the organic cation and the ratio between $[MX_6]^{4-}$ and A^+.

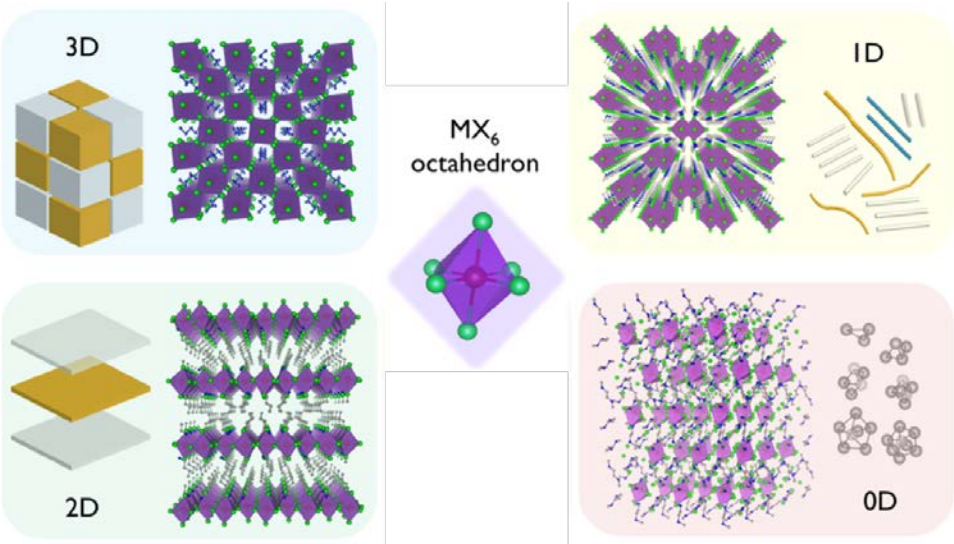

Figure 1.9: Typical structures of 3D, 2D, 1D, and 0D perovskites, as well as their corresponding conventional materials with different dimensionalities. The figure is taken from reference 32.

The lattice of the perovskite is never ideal and the distortions can affect into the physical and optical properties of the crystal. Additionally, the size of cation and metal ion influence the lattice structure and are crucial parameters to modulate the optical and electronic properties of the material.[33,34] Herein, we will focus on the family of lead halide perovskites $CH_3NH_3PbX_3$, where X = I, Cl, Br, and more specifically on methylammonium lead iodide perovskite ($CH_3NH_3PbI_3$ or $MAPI_3$), which exhibits the crystal structure shown on **Figure 1.10**.

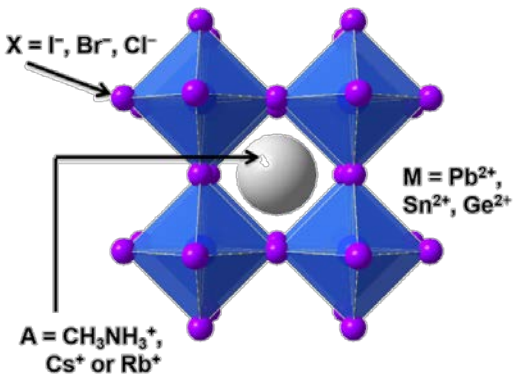

Figure 1.10: Crystal structure of methylammonium lead iodide perovskite - $CH_3NH_3PbI_3$. Figure is taken from reference 35.

The phase of $MAPI_3$ at room temperature is tetragonal with *I4/mcm* space group, while increasing the temperature above to 327 K leads to the cubic structure with *Pm3m* space group. Moreover, lowering the temperature below to 160 K the phase of $MAPI_3$ changes to orthorhombic with $Pna2_1$ space group, due to the freezing of the orientation of MA^+.[36-38] These three phases are usually referred to α (cubic), β (tetragonal) and γ (orthorhombic) phases.[39] In **Chapter 6** we will explore how the charge carrier dynamics of the perovskite change among these phases.

Hybrid organic-inorganic perovskites are of special interest for photovoltaic applications due to their extraordinary properties such as absorption in the entire visible range (**Figure 1.11(a)**), strong absorption coefficient (1.5×10^5 cm^{-1} at 500 nm), long carrier diffusion length (up to 1μm), low recombination rates and band gap tunability (**Figure 1.11(b)**).[40] The optical bandgap of $MAPI_3$ is 1.53 eV as illustrated in **Figure 1.11(c)**,[41] which is very close to 1.34 eV, the optimum bandgap for single junction cell.[42,43] The top of the valence band is found to consist mainly of the σ-antibonding states of Pb 6s and I 5p orbitals, and the bottom of the conduction band to be composed primarily of the σ-antibonding states of Pb 6p and I 5s orbitals (**Figure 1.11d**).[44]

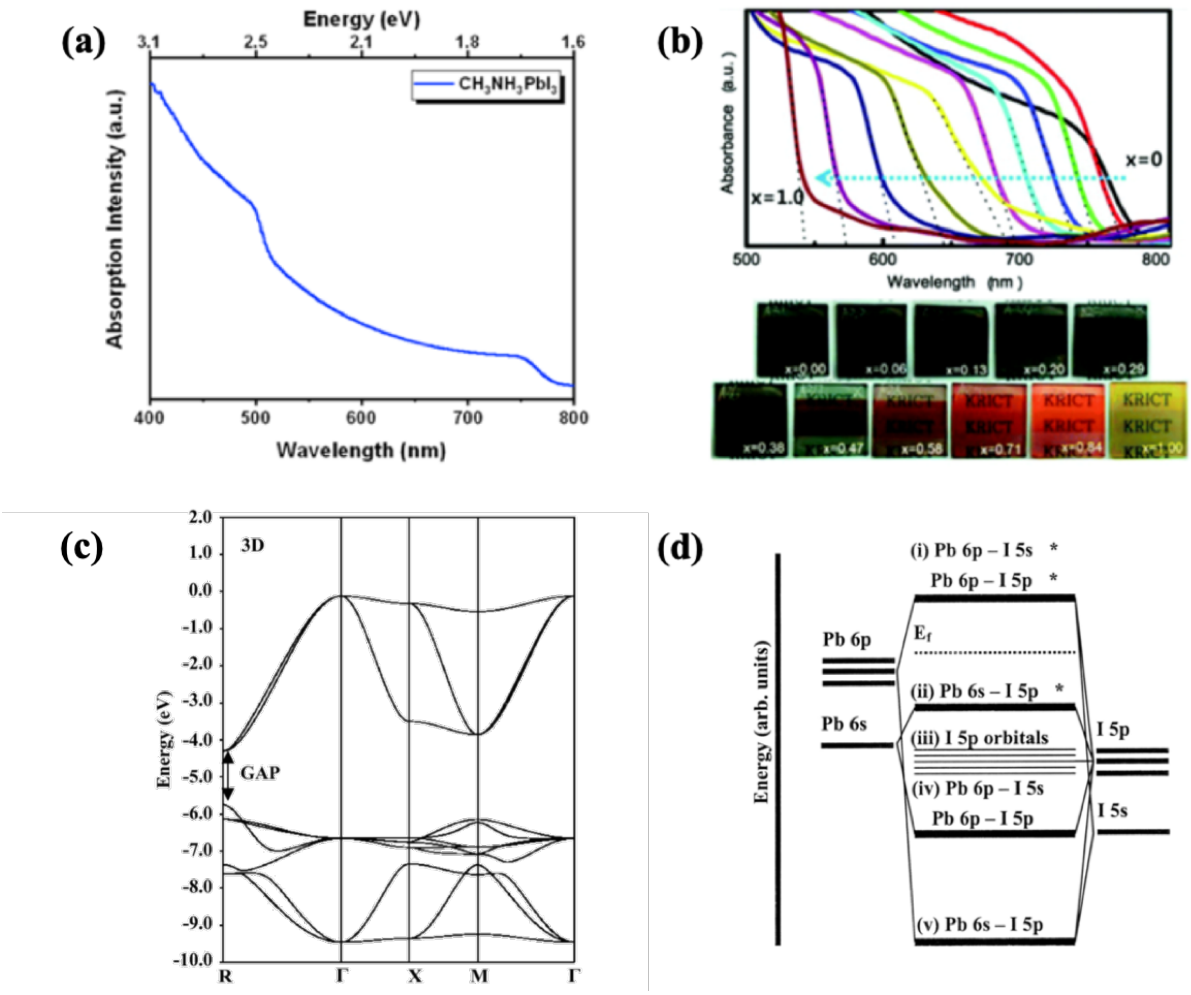

Figure 1.11: (a) The experimental absorption spectra of $CH_3NH_3PbI_3$, **(b)** The band gap tunability of $CH_3NH_3PbI_{3-x}Cl_x$.[40] **(c)** Calculated band structure for the 3D $hMAPbI_3$ along the high-symmetry lines in first Brillouin zone.[41] **(d)** Bonding diagram of a $[PbI_6]^{-4}$ cluster (zero-dimensional system) of 3D crystal $CH_3NH_3PbI_3$.[44] Figure 1.12(b), (c), (d) are taken from references 40, 41 and 44, respectively.

In addition to these extraordinary optical properties, the lead halide perovskites exhibit electron mobility of 66 $cm^{-2}V^{-1}s^{-1}$, while the tin halide perovskites exhibit electron mobility of 2320 $cm^{-2}V^{-1}s^{-1}$.[45] These values are comparable with the value of silicon (1400 $cm^{-2}V^{-1}s^{-1}$). Methylammonium lead iodide can be considered as an ionic compound with the permanent dipole moment, because of the presence of a $CH_3NH_3^+$ cation and a PbI_3^- anion, resulting to relatively high dielectric constant; initially to 6.5,[46] while recent reports given even higher values, up to 30.[47] The high dielectric constant also explains the low binding energies of the

exciton in $CH_3NH_3PbI_3$, since the photo-induced charges can be effectively screened by the dipoles of the lattice.

1.5.2 Free Carriers: The Major Photo-generated Species

A very crucial question that the researchers had to answer is if the excitons exist in the perovskite solar cells following photo-excitation! After 2 years of extensive study on the photo-dynamics in lead halide perovskites, the scientists agree that the major photo-generated species are the free charge carriers instead of excitons.[48-53]

When a photon with the appropriate energy, equal with the band gap of the semiconductor, is absorbed by the perovskite, an electron move from the valence band to the conduction band and leaves behind a positively charged, called electron-hole. The excited electron and the electron-hole are attracted by the electrostatic Coulomb force and this bound state is called exciton. The exciton is an electrically neutral quasi-particle and exists in regarded as elementary excitation of condensed matter that can transport energy without transporting net electric charge.[54,55] The excited electron is effectively attracted to the localized hole by the repulsive Coulomb force and this attraction provides a stabilizing energy balance; thus, the exciton has less energy than the unbound electron and hole. While the wave function of the exciton is said to be hydrogenic, the binding energy is much smaller and the particle's size much larger than a hydrogen atom. The Coulomb attraction results in a series of hydrogen-like states:[56]

$$\boldsymbol{E_{ex}(n_B, K) = E_g - R_y \cdot \frac{1}{n_B^2} + \frac{\hbar^2 K^2}{2M}} \quad \textit{(1.5)}$$

where:

n_B = 1, 2, 3 …. (principle quantum number)

R_y^* = 13.6 eV $\frac{\mu}{m_0}\frac{1}{\varepsilon^2}$ (exciton Rydberg energy)

$M = m_e + m_h$, $K = k_e + k_h$ (translational mass and wave vector of the exciton)

$\mu = \frac{m_e m_h}{m_e + m_h}$ (reduced exciton mass)

So, the exciton is considered as a hydrogen-like quasi-particle, which Rydberg Bohr radius (the radius of the lowest excitonic state) can be estimated by equation $\alpha_B^{ex} = \alpha_B^H \varepsilon \frac{m_0}{\mu}$.

It is well known that the narrow gap semiconductors have smaller exciton binding energy and vice versa. This is the result of the fact that larger band gap leads to smaller bandwidth, and thus small dispersion and carriers with large effective mass. The first studies showed that the binding energy of the lead halide perovskite was ~50 meV, one order of magnitude larger than GaAs, while the band gap of the perovskite is ~1.5 eV, which is fairly similar to GaAs.[52,57-59] In this case the main photo-generated species should be the excitons instead of the free charge carriers due to the large binding energy. Moreover, later experiments revealed lower estimation of the exciton binding energy[60-63] until the lowest value of 2 meV that Lin et al. reported, which derived from the measured real static dielectric constant of 70,[64] which is very close to the exciton binding energy of the GaAs (5 meV). At room temperature (RT) there are no excitons because the thermal energy is enough to break the excitons to free charge carriers.

Moreover, the fitting of the ground state absorption edge at different temperatures to Elliot's theory of Wannier exciton present exciton binding energy of 25 ± 3 meV (**Figure 1.12(a)** and **(b)**) and the PL intensity right after laser pulse excitation was found to be quadratic with injected carrier density (**Figure 1.12(c)**).[49] The former indicates exciton transition dose enhance band-edge transition while the latter shows that bound-excitons are not actually populated.

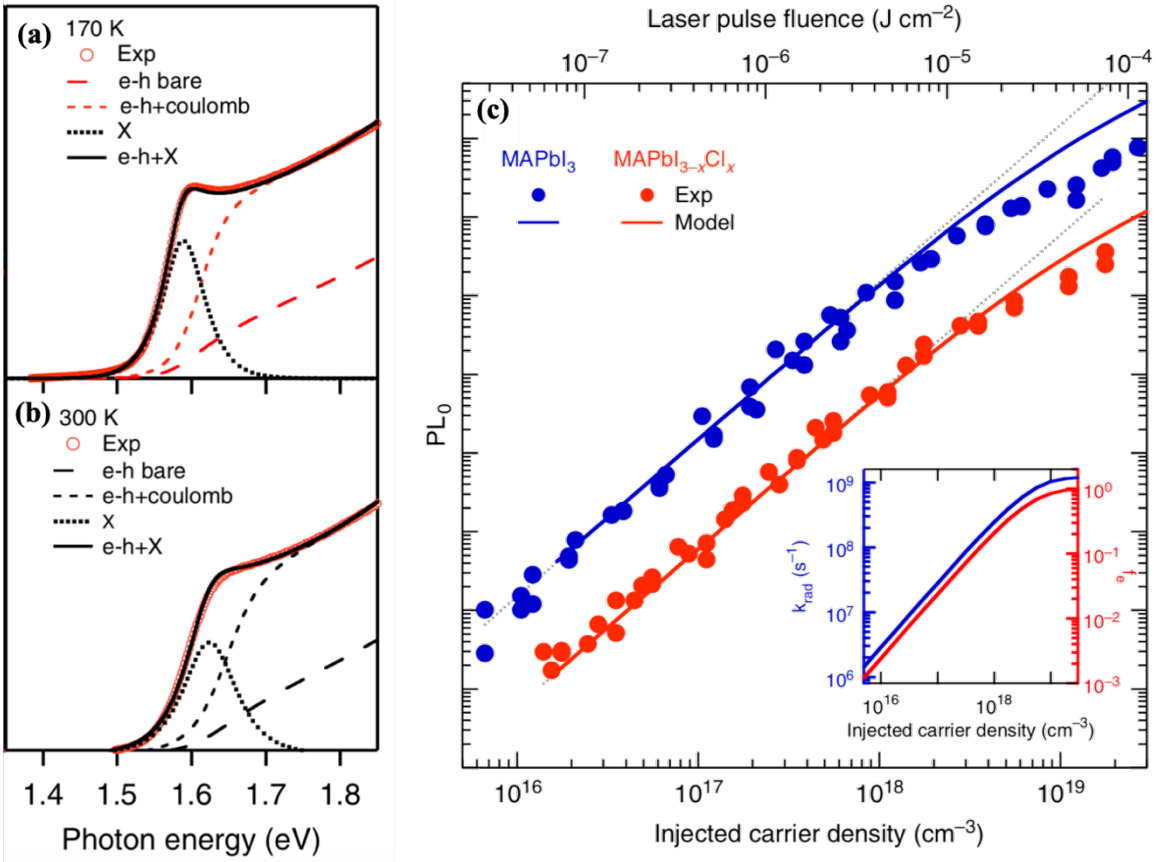

Figure 1.12: (a) and **(b)** Theoretical fits (lines) to the experimental absorption spectra at 170 and 300 K, respectively. Dotted lines: exciton transitions. Short-dashed (long-dashed) lines: band-to-band contributions with (without) the inclusion of Coulomb interactions and **(c)** Photoluminescence emission intensity estimated at t = 0 (PL_0) as a function of injected electron–hole density (lower axis) and laser pulse fluence (upper axis). Inset: calculated spontaneous photon emission per electron–hole pair (k_{rad}, blue line) and occupation number of the lowest electron (hole) states in a non-interacting plasma based on Fermi–Dirac statistics ($f_{e(h)}$, red line). Figures are reproduced from reference 49.

1.5.3 Long Diffusion Length and Low Bimolecular Recombination Rates

Even though the main photo-generated species in perovskite solar cells are the free carriers, they are able to recombine each other. In order to extract useful information about the carrier lifetime, it is necessary to analyze the Photoluminescence (PL) and Time Resolved Absorption Spectroscopy (TAS) carrier lifetimes. Stranks et al. have reported that the diffusion length is greater than 1μmin mixed halide perovskite,[65] while in triiodide absorber the electron-hole diffusion length is around 100 nm[65,66] In contrast, for $MAPbI_3$ single

crystal, a recent study, showed much longer carrier diffusion length of 175 μm to a few mm.[67] Furthermore, with time-resolved absorption spectroscopy, presented in **Figure 1.13 (a)** and **(b)**, Wehrenfennig et al. have shown high carrier mobility for lead halide perovskite of about 10 cm^2 V^{-1} s^{-1} and low bimolecular recombination rate (second order recombination rate) of 8.7×10^{-11}.[48]

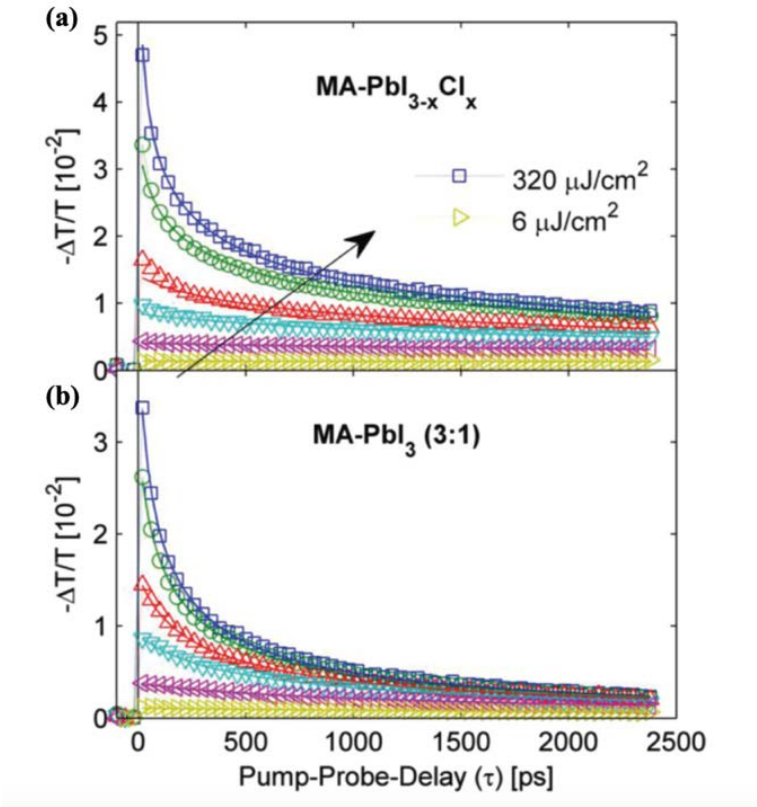

Figure 1.13: (a) THz photo-induced absorption transient of (a) $CH_3NH_3PbI_{3-x}Cl_x$ and **(b)** $CH_3NH_3PbI_3$ (3:1) after excitation at 550 nm for fluences between 6 μJ cm^{-2} and 320 μJ cm^{-2}. Solid lines are fits based on second- and third- order charge recombination. Figures are taken from reference 48.

Later in the same year, Manser and Kamat, reported the Burstein-Moss band filling effect (**Figure 1.14**) from transient absorption spectroscopy (TAS) measurements on methylammonium lead halide perovskite films, giving a blue-shift of the high energy edge of the ground state bleaching peak with increasing pump fluence.[50] By fitting the decay

dynamics of the bleaching peak, they obtained a bimolecular recombination rate of (2.3 ± 0.6) × 10−9 cm^3 s^{-1}.[50] The accumulation of the carriers in the conduction band along with the two-body recombination is representative of an excited state composed primarily of free carriers, and these free charges can potentially limit exciton formation by coulombic screening effects.

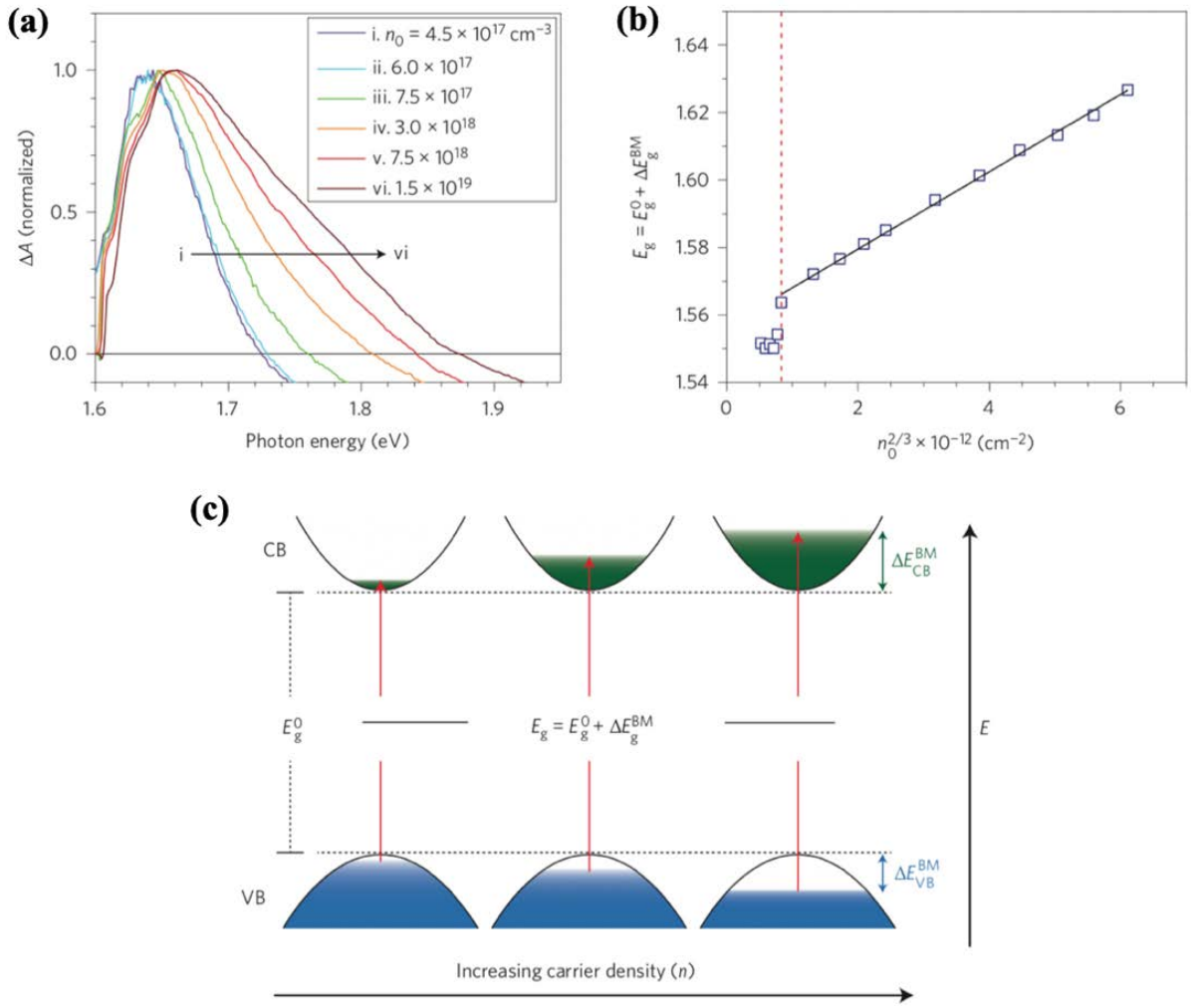

Figure 1.14: (a) Normalized transient absorption spectra of the band-edge transition in $CH_3NH_3PbI_3$ recorded at the maximum bleach signal (5 ps) after 387 nm pump excitation of varying intensity, **(b)** Modulation of the intrinsic bandgap of $CH_3NH_3PbI_3$ according to the Burstein–Moss model and **(c)** Schematic representation of the Burstein–Moss effect showing the contribution from both electrons in the conduction band (CB) and holes in the valence band (VB) due to their similar effective masses. Figures are taken from reference 50.

References:

1. Available at http://www.worldometers.info/world-population/
2. Available at https://www.eia.gov/outlooks/aeo/pdf/AEO2018.pdf
3. Available at https://www.instituteforenergyresearch.org/fossil-fuels/global-energy-demand-and-fossil-fuel-consumption-rose-in-2018-increasing-carbon-dioxide-emissions/
4. Available at https://energyinformative.org/fossil-fuels-pros-and-cons/
5. Available at http://www.climateaction.org/news/renewables_can_reduce_co2_emission_by_70_by_2050
6. Sum, T. C., Mathews, N. Advancements in Perovskite Solar Cells: Photophysics Behind the Photovoltaics. *Energy Enviro. Sci.* **2014**, *7*, 2518-2534.
7. Available at https://en.wikipedia.org/wiki/Solar_irradiance
8. Becquerel, A. E. Recherches sur les effets de la radiation chimique de la lumiere solaire au moyen des courants electriques. *Comptes Rendus Acad. Sci.* **1839**, *9*, 145-149.
9. Becquerel, A. E. On Electron Effects under the Influence of Solar Radiation. *Comptes Rendus Acad. Sci.* **1839**, *9*, 561-567.
10. Shockley, W., Queisser, H. J. Detailed Balance Limit of Efficiency of p-n Junction Solar Cells. *J. Appl. Phys.* **1961**, *32*, 510-519.
11. Hanna, M. C., Nozik, A. J. Solar Conversion Efficiency of Photovoltaic and Photoelectrolysis Cells with Carrier Multiplication Absorbers. *J. Appl. Phys.* **2006**, *100*, 074510.
12. Green, M. A., Emery, K., Hishikawa, Y., Warta, W. Solar Cell Efficiency Tables (Version 34) *Prog. Photovolt: Res. Appl*. **2009**, *17*, 320-326.
13. Available at https://www.powerfromsunlight.com/photovoltaic-solar-cells-main-types-solar-panels-guide-choose-convenable-solar-panel-type/
14. Available at https://phys.org/news/2011-06-efficiency-flexible-cdte-solar-cell.html
15. Available at https://www.greenoptimistic.com/cigs-manufacturing-technology-20100719/ - .XD291i2B28o
16. Conibeer, G. Third-generation photovoltaics. *Mater. Today* **2007**, *10*, 42-50.
17. Available at https://www.nrel.gov/pv/assets/pdfs/pv-efficiency-chart.20190103.pdf
18. Nazeeruddin, M. K., Kay, A., Rodicio, I., Humphry-Baker, R., Müller, E., Liska, P., Vlachopoulos, N., Grätzel, M. Conversion of Light to Electricity by cis-X2bis (2, 2'-bipyridyl-4, 4'-dicarboxylate) Ruthenium (II) Charge-Transfer Sensitizers (X= Cl-, Br-, I-, CN-, and SCN-) on Nanocrystalline Titanium Dioxide Electrodes. *J. Am. Chem. Soc.* **1993**, *115*, 6382-6390.
19. Grätzel, M. Photoelectrochemical Cells. *Nature* **2001**, *414*, 338-344.
20. Hardin, B. E., Snaith, H. J., McGehee, M. D. The Renaissance of Dye-sensitized Solar Cells. *Nat. Photonics* **2012**, *6*, 162
21. Liang, Y., Xu, Z., Xia, J., Tsai, S. T., Wu, Y., Li, G., Ray, C., Yu, L. For the Bright Future - Bulk Heterojunction Polymer Solar Cells with Power Conversion Efficiency

of 7.4%. *Adv. Mater.* **2010**, *22*, E135–E138.
22. Scharber, M. C., Koppe, M., Gao, J., Cordella, F., Loi, M. A., Denk, P., Morana, M., Egelhaaf, H. J., Forberich, K., Dennler, G., Gaudiana, R., Waller, D., Zhu, Z., Shi, X., Brabec, C. J. Influence of the Bridging Atom on the Performance of a Low-Bandgap Bulk Hetero-junction Solar Cell. *Adv. Mater.* **2010**, *22*, 367–370.
23. Kojima, A., Teshima, K., Shirai, Y., Miyasaka, T. Organometal Halide Perovskites as Visible-light Sensitizers for Photovoltaic Cells. *J. Am. Chem. Soc.* **2009**, *131*, 6050-6051.
24. Im, J. H., Lee, C. R., Lee, J. W., Park, S. W., Park, N. G. 6.5% Efficient Perovskite Quantum-dot-sensitized Solar Cell. *Nanoscale* **2011**, *3*, 4088-4093.
25. Lee, M. M., Teuscher, J., Miyasaka, T., Murakami, T. N., Snaith, H. J. (2012). Efficient Hybrid Solar Cells Based on Meso-superstructured Organometal Halide Perovskites. *Science* **2012**, *338*, 643-647.
26. Bai, Y., Cao, Y., Zhang, J., Wang, M., Li, R., Wang, P., Zakeeruddin, S. M., Grätzel, M. High-performance dye-sensitized solar cells based on solvent-free electrolytes produced from eutectic melts. *Nat. Mater.* **2008**, *7*, 626.
27. Gruber, M., Wagner, J., Klein, K., Hörmann, U., Opitz, A., Stutzmann, M., Brütting, W. Thermodynamic efficiency limit of molecular donor-acceptor solar cells and its application to diindenoperylene/C_{60}-based planar heterojunction devices. *Adv. Energy Mater.* **2012**, *2*, 1100-1108.
28. Zhou, Z., Pang, S., Liu, Z., Xu, H., Cui, G. Interface engineering for high-performance perovskite hybrid solar cells. *J. Mater. Chem. A* **2015**, *3*, 19205-19217.
29. Gao, P., Graetzel, M., Nazeeruddin, M. Organohalide Lead Perovskites for Photovoltaic Applications. *Energy Environ. Sci.* **2014**, *7*, 2448-2463.
30. Available at https://www.pveducation.org/
31. Glazer, A.M.: The Classification of Tilted Octahedra in Perovskites. *Acta Crystallogr. Sect. B* **1972**, *28*, 3384–3392.
32. Lin, H., Zhou, C., Tian, Y., Siegrist, T., Ma, B. Low-dimensional Organometal Halide Perovskites. *ACS Energy Lett.* **2017**, *3*, 54-62.
33. Cheng, Z., Lin, J. Layered Organic–inorganic Hybrid Perovskites: Structure, Optical Properties, Film Preparation, Patterning and Templating Engineering. *Cryst Eng Comm.* **2010**, *12*, 2646–2662.
34. Mitzi, D. B., Chondroudis, K., Kagan, C. R. Organic-inorganic Electronics. *IBM J. Res. & Dev.* **2001**, *45*, 29–45.
35. Available at https://research.cbc.osu.edu/woodward.55/research/halide-perovskites/
36. Poglitsch, A., Weber, D. Dynamic Disorder in Methylammoniumtrihalogenoplumbates (II) Observed by Millimeter-wave Spectroscopy. *J. Chem. Phys.* **1987**, *87*, 6373-6378.
37. Onoda-Yamamuro, N., Matsuo, T., Suga, H. Dielectric study of $CH_3NH_3PbX_3$ (X= Cl, Br, I). *J. Phys. Chem. Solids* **1992**, *53*, 935-939.
38. Ball, J. M., Lee, M. M., Hey, A., Snaith, H. J. Low-temperature Processed Meso-superstructured to Thin-film Perovskite Solar Cells. *Energy Environ. Sci.* **2013**, *6*, 1739-1743.

39. Liu, M., Johnston, M. B., Snaith, H. J. Efficient Planar Heterojunction Perovskite Solar Cells by Vapour Deposition. *Nature* **2013**, *501*, 395.
40. Gao, P., Graetzel, M., Nazeeruddin, M. Organohalide Lead Perovskites for Photovoltaic Applications. *Energy Environ. Sci.* **2014**, *7*, 2448-2463.
41. Umebayashi, T.; Asai, K.; Kondo, T.; Nakao, A. Electronic Structures of Lead Iodide Based Low-dimensional Crystals. *Phys. Rev. B* **2003**, *67*, 155405.
42. Available at https://en.wikipedia.org/wiki/Shockley%E2%80%93Queisser_limit
43. Rühle, S. Tabulated Values of the Shockley–Queisser Limit for Single Junction Solar Cells. *Solar Energy* **2016**, *130*, 139-147.
44. Umebayashi, T., Asai, K., Kondo, T., Nakao, A. Electronic structures of lead iodide based low-dimensional crystals. *Phys. Rev. B* **2003,** 67, 155405.
45. Stoumpos, C. C., Malliakas, C. D., Kanatzidis, M. G. Semiconducting Tin and Lead Iodide Perovskites with Organic Cations: Phase Transitions, High Mobilities, and Near-infrared Photoluminescent Properties. *Inorg. Chem.* **2013**, *52*, 9019-9038.
46. Hirasawa, M., Ishihara, T., Goto, T., Uchida, K. Miura, N. Magnetoabsorption of the Lowest Exciton in Perovskite-type Compound $(CH_3NH_3)PbI_3$. *Phys. B* **1994**, *201*, 427–430.
47. Pellet, N., Gao, P., Gregori, G., Yang, T. Y., Nazeeruddin, M. K., Maier, J., Grätzel, M. Mixed-Organic-Cation Perovskite Photovoltaics for Enhanced Solar-Light Harvesting. *Angew. Chem. Int. Ed. (English)* **2014**, *53*, 3151–3157.
48. Wehrenfennig, C., Eperon, G. E., Johnston, M. B., Snaith, H. J. Herz, L. M. High Charge Carrier Mobilities and Lifetimes in Organolead Trihalide Perovskites. *Adv. Mater.* **2013**, *26*, 1584–1589.
49. Saba, M., Cadelano, M., Marongiu, D., Chen, F., Sarritzu, V., Sestu, N., Figus, C., Aresti, M., Piras, R., Lehmann, A. G., Cannas, C., Musinu, A., Quochi, F., Mura, A., Bongiovanni, G. Correlated Electron-hole Plasma in Organometal Perovskites. Nat. Commun. **2014**, *5*, 5049.
50. Manser, J. S. Kamat, P. V. Band Filling with Free Charge Carriers in Organometal Halide Perovskites. *Nat. Photonics* **2014**, *8*, 737–743.
51. Trinh, M. T., Wu, X., Niesner, D. Zhu, X. Many-Body Interactions in Photo- Excited Lead Iodide Perovskite. *J. Mater. Chem. A* **2015**, *3*, 9285-9290.
52. D'Innocenzo, V., Grancini, G., Alcocer, M. J., Kandada, A. R. S., Stranks, S. D., Lee, M. M., Lanzani, G., Snaith, H. J., Petrozza, A. Excitons Versus Free Charges in Organo-lead Tri-halide Perovskites. *Nat. Commun.* **2014**, *5*, 3586.
53. Yamada, Y., Nakamura, T., Endo, M., Wakamiya, A. Kanemitsu, Y. Photocarrier Recombination Dynamics in Perovskite $CH_3NH_3PbI_3$ for Solar Cell Applications. *J. Am. Chem. Soc.* **2014**, *136*, 11610–11613.
54. Liang, W. Y. Excitons. *Phys. Educ.* **1970**, *5*, 226.
55. Knox, R. S. *Theory of excitons*; Academic Press, 1963.
56. Klingshirn, C. F. *Semiconductor Optics*; Springer, 2012.
57. Grancini, G., Kandada, A. R. S., Frost, J. M., Barker, A. J., De Bastiani, M., Gandini, M., Marras, S., Lanzani, G., Walsh, A., Petrozza, A. Role of Microstructure in the Electron–hole Interaction of Hybrid Lead Halide Perovskites. *Nat. Photonics* **2015**, *9*, 695-701.

58. Manser, J. S., Kamat, P. V. Band Filling with Free Charge Carriers in Organometal Halide Perovskites. *Nat. Photonics* **2014**, *8*, 737-743.
59. Kim, H. S., Im, S. H., Park, N. G. Organolead Halide Perovskites: New Horizons in Solar Cell Research. *J. Phys. Chem C* **2014**, *118*, 5615-5625.
60. Miyata, A., Mitioglu, A., Plochocka, P., Portugall, O., Wang, J. T. W., Stranks, S. D., Snaith, H. J., Nicholas, R. J. Direct Measurement of the Exciton Binding Energy and Effective Masses for Charge Carriers in Organic–inorganic Tri-halide Perovskites. *Nat. Physics* **2015**, *11*, 582.
61. Green, M. A., Jiang, Y., Soufiani, A. M., Ho-Baillie, A. Optical Properties of Photovoltaic Organic–inorganic Lead Halide Perovskites. *J. Phys. Chem. Lett.* **2015**, *6*, 4774-4785.
62. Sun, S., Salim, T., Mathews, N., Duchamp, M., Boothroyd, C., Xing, G., Sum, T. C., Lam, Y. M. The Origin of High Efficiency in Low-temperature Solution-processable Bilayer Organometal Halide Hybrid Solar Cells. *Energy Environ. Sci.* **2014**, *7*, 399-407.
63. Koutselas, I. B., Ducasse, L., Papavassiliou, G. C. (1996). Electronic Properties of Three-and Low-dimensional Semiconducting Materials with Pb Halide and Sn Halide Units. *J. Phys, Condens. Matter* **1996**, *8*, 1217.
64. Lin, Q., Armin, A., Nagiri, R. C. R., Burn, P. L., Meredith, P. (2015). Electro-optics of Perovskite Solar Cells. *Nat. Photonics* **2015**, *9*, 106.
65. Stranks, S. D.; Eperon, G. E.; Grancini, G.; Menelaou, C.; Alcocer, M. J.; Leijtens, T.; Herz, L. M.; Petrozza, A.; Snaith, H. J. Electron-Hole Diffusion Lengths Exceeding 1 micrometer in an Organometal Trihalide Perovskite Absorber. *Science* **2013**, *342*, 341-344.
66. Xing, G; Mathews, N.; Sun, S.; Lam, Y. M.; Graetzel, M.; Mhaisalkar, S.; Sum, T. C. Long-range Balanced Electron- and Hole-Transport Lengths in Organic-inorganic $CH_3NH_3PbI_3$. *Science* **2013** *342*, 344–347.
67. Dong, Q.; Fang, Y.; Shao, Y.; Mulligan, P.; Qiu, J.; Cao, L.; Huang, J. Electron-hole Diffusion Lengths >175 um in Solution Grown $CH_3NH_3PbI_3$ Single Crystals. *Science* **2015**. 347, 967–970.

Chapter 2

Time-resolved Absorption Spectroscopy

In this Chapter, we focus on the principle, theory and implementation of the TAS technique that is used in this dissertation for the study of the charge carrier dynamics and recombination processes in PSCs.

2.1 Introduction to Transient Absorption Spectroscopy

Nanosecond Transient Absorption (also known as Flash Photolysis) is the simplest form of the pump-probe technique and was developed before the invention of lasers. *Manfred Eigen*, *Ronald George Wreyford Norrish* and *George Potter* received the **1967 Nobel Prize in Chemistry** for the invention of this technique and its application *for studies of extremely fast chemical reactions, effected by disturbing the equilibrium by means of very short impulses of energy*.[1]

The basic principles of the Flash Photolysis techniques, relies on short laser pump pulses exciting a sample, while a continuous light source probes the response of the sample to the excitation event (**Figure 2.1**).

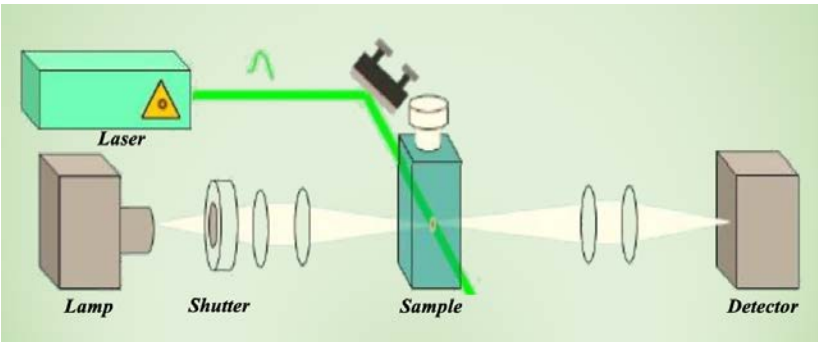

Figure 2.1: Schematic illustration of a Flash Photolysis technique.[2]

2.2 Femtosecond Transient Absorption Spectroscopy

2.2.1 Fundamentals of the fs-TAS

The ultrafast version of the typical Flash Photolysis technique is the Femtosecond Transient Absorption Spectroscopy. When the signal is faster than the nanosecond, it is difficult to detect it electronically, and it is necessary to exploit the properties of optical delays of the light pulses. This is based on the different optical paths between the pump and the probe beam that used for the pump-probe measurements. Thus, we are able to control the time that the probe reach the sample with respect to the pump beam. The light in air travels 300 nm in 1 fs, so the desired time interval can be selected by adjusting the travelling distance with mirrors on a moving translation stage (delay line).

Femtosecond transient absorption technique is composed of two beams, the pump and the probe, as shown in **Figure 2.2**. The fundamental beam (1026 nm) was split at the pump beam (90% of the initial beam) and the probe beam (10% of the initial beam). The pump beam is used for the sample excitation, while the other part of the fundamental beam, the probe beam, is passed through the delay line and then is focused on a non-linear crystal (YAG crystal), generating a supercontinuum white light. The intensity of both beams can be controlled by a reflective neutral density filter. The pump beam after the excitation is blocked, while the probe beam, after the sample, was coupled through an optical fiber to the spectrograph and monitored as a function of wavelength at various delay time after photoexcitation. The pump spot size is always larger than the probe spot size to ensure that all the detected area is already excited. The pump beam is not focused on the sample in order to have homogeneous excitation, while the probe beam is focused on the sample. The detected signal is the delta optical density (ΔOD) between the optical density only with the probe ($O.D._{probe}$) and the optical density after excitation ($O.D._{pump+probe}$). By changing the delay line between the two

beams, we can follow ΔOD profile as a function of time (τ) and wavelength (nm). The delta optical density is expressed as:[3]

$$\boldsymbol{\Delta OD = log\left(\frac{blocked}{unblocked}\right) = log(blocked) - log(unblocked) =}$$
$$\boldsymbol{= O.D._{probe} - O.D._{pump+probe}} \quad \textbf{(2.1)}$$

All TAS measurements for the perovskite solar cells were performed entirely under inert conditions within a specially designed homemade cell (**Figure 2.2**) in order to exclude any degradation effects throughout measurement.

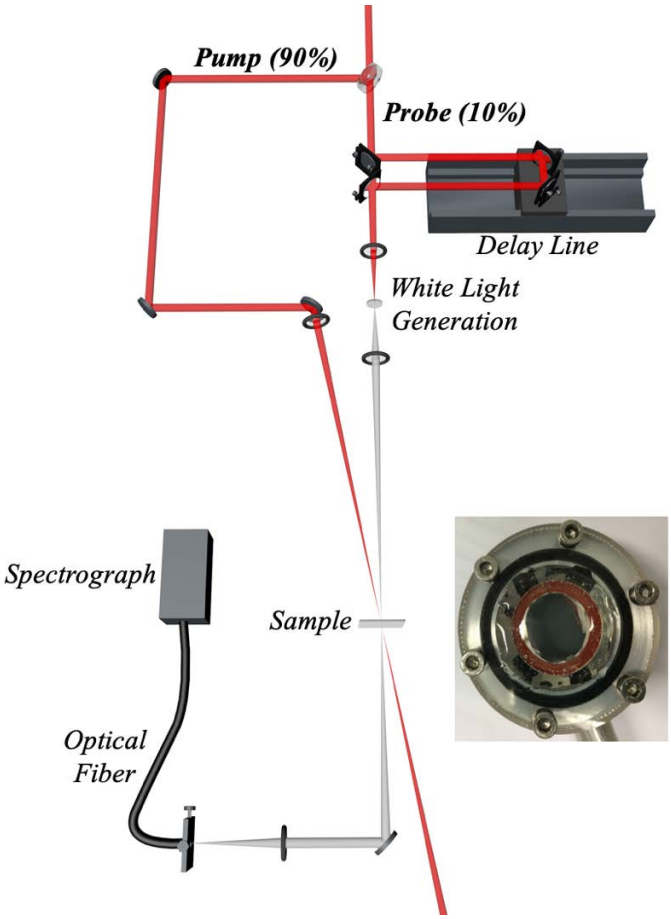

Figure 2.2: Schematic representation of Newport transient absorption spectrometer (TAS-1),[3] **(inset)** The specially designed homemade cell employed for all TAS measurements in order to maintain inert conditions throughout measurements (extra pure nitrogen gas as in the fabrication glove box).

The typical TAS plot, as shown in **Figure 2.3(a)** consists of 2D contour plot with color scale representing the ΔOD of methylammonium lead iodide perovskite ($CH_3NH_3PbI_3$) and x and y axes depict the time-delay (τ) and wavelength (λ) respectively. From the TAS spectra we are able to extract useful information for the dynamics processes after photoexcitation occurring on semiconductor materials. **Figure 2.3(b)** shows the corresponding ΔOD vs wavelength plots at various time delays and **Figure 2.3(c)** depicts the transient band edge bleach kinetics following photoexcitation.

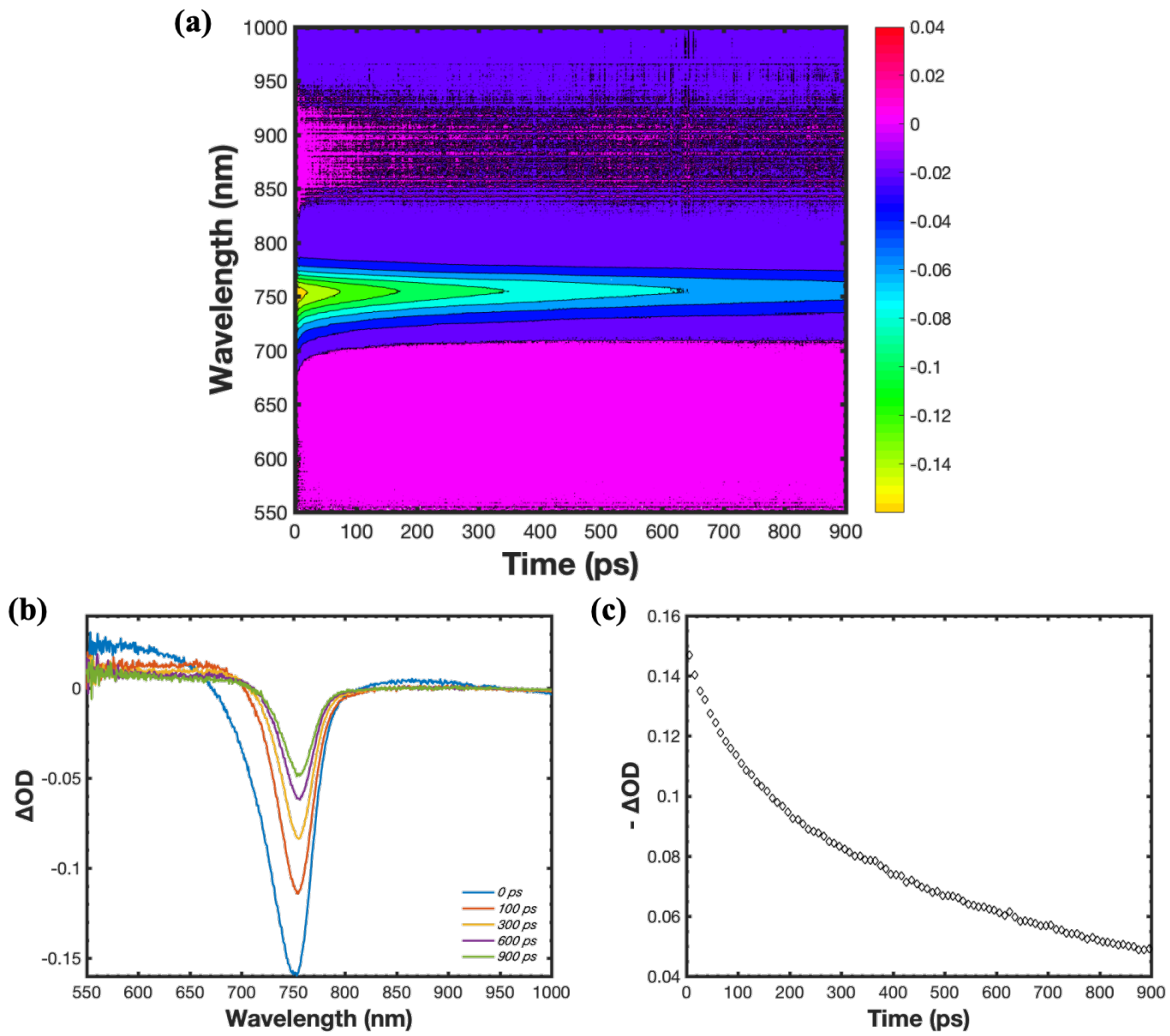

Figure 2.3: (a) Typical 2D contour plot of ΔOD (color scale) of a $CH_3NH_3PbI_3$ perovskite film on top of PTAA at various delay times and wavelengths, **(b)** ΔOD vs wavelength plots at various time delays and **(c)** Transient band edge bleach kinetics following photoexcitation.

In a typical 2D contour plot of ΔOD at various delay times and wavelengths or in ΔOD vs wavelength plot at various time delays, we observe various features that are attributed to different dynamics processes that occur in a perovskite absorber layer (or in semiconductors, generally). In particular:

Ground State Photo-bleaching (GSB): The most common feature in a TAS spectrum is the so-called ground state photo-bleaching. It is illustrated as a strong negative signal near to the band edge transition. The origin for this negative peak is attributed to excitation of valence band electrons to the conduction band by the pump pulse, indicating that there are fewer photoreceptors in the ground state available to absorb the probe light (**Figure 2.4(a-c)**). **Figure 2.3(a)** and **(b)** show this negative peak at ~750 nm, which corresponds to absorption wavelength of the lead halide perovskite.

Photo-induced Absorption (PIA): The other most usual characteristic in a TAS spectrum is the photo-induced absorption. It is depicted as a positive signal either below or above the band edge transition. This positive signal is the result of the photoexcitation carriers from the valance band to the conduction band, that may absorb photons and be further excited to higher excited states (**Figure 2.4(d-f)**). Excited state absorption provides us valuable information for intra-band/inter-band transitions or polaron transitions. This feature depicted in **Figure 2.3(b)** in the range of ca. 550-700 nm.

Stimulated Emission (SE): The second possible negative feature in TAS spectrum is the stimulated emission. The Einstein coefficients, for a two-level system, for excitation from the ground state to excited state (A_{12}) with absorption of a photon and for stimulated recombination form the excited state to ground state (A_{21}) with emission of a photon, are the

same. SE occurs only for optically allowed transitions (bright states) and look likes with the fluorescence spectrum. A photon, form the probe beam stimulate the emission of another photon from the sample with the same energy and momentum. SE is usually Stokes shifted from the ground state absorption, increasing the photons and resulting to negative signal in TAS spectrum.

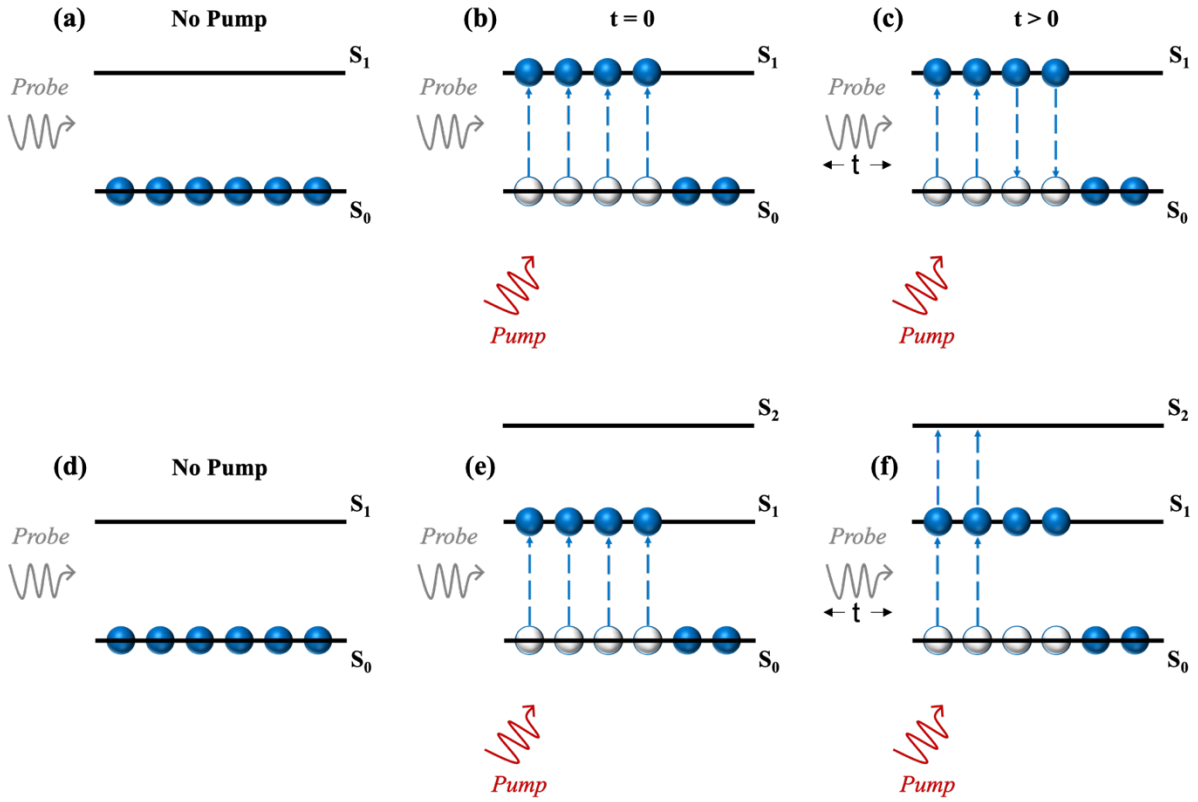

Figure 2.4: Schematic representation of mechanisms for ground state photo-bleaching **(a-c)** and photo-induced absorption **(d-f)**.

2.2.2 Excitation Source

The excitation source is, a compact solid state pulsed laser with ytterbium doped with potassium, gadolinium and tungsten (Yb:KGW) active medium, the 'Pharos' laser system from Light Conversion.[4] It emits at a central wavelength of 1026 nm and it supports harmonic generation of the fundamental at 513 nm. The maximum pulse energy is 1.5 mJ and

the repetition rate ranges from 1 kHz up to 200 kHz. The pulse width can vary from 170 fs to 10 ps. For our experiments, we preferred to use the minimum of the pulse duration in order to higher resolution and also to be able to generate the supercontinuum white light.

2.2.3 Supercontinuum White Light Generation

In ultrafast time-resolved absorption spectroscopy as probe beam, we use the supercontinuum white light. In order to generate the white light, we use a non-linear sapphire or YAG crystal. The laser beam is focused into the crystal and due to the self-focusing and self-phase modulation we generate the white light. The self-focusing (**Figure 2.5**) is the process that due to the high intensity of the laser pulse the refractive index of the material is changed and act as focusing lens.

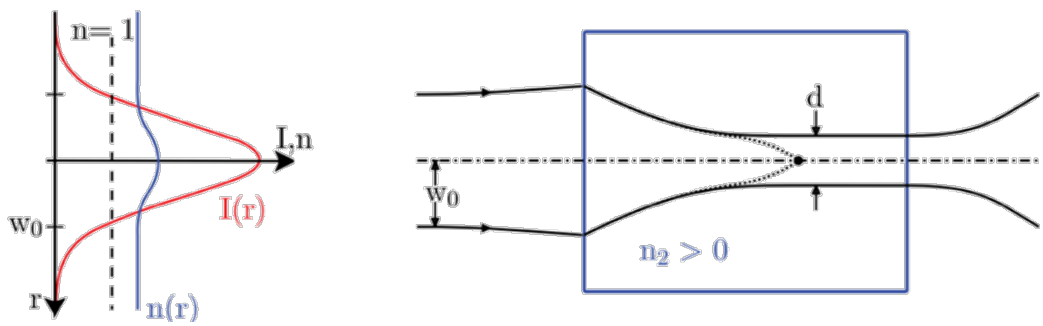

Figure 2.5: Schematics of the intensity profile of a real laser beam and the corresponding refraction index n. Beam diameter and self-focusing effect in a nonlinear optical medium.[5]

The total refractive index is calculated from the equation:

$$\mathbf{n = n_0 + n_2 I}$$

where: n_0, is the fundamental refractive index of the optical medium,

n_2, is the induced refractive index, and

I, is the intensity

Moreover, the self-phase modulation (SPM) (**Figure 2.6**) is a nonlinear optical effect of light-matter interaction. An ultrashort pulse of light, when travelling in a non-linear medium with variation in refractive index will produce a phase shift in the pulse, leading to a change of the pulse's frequency spectrum.

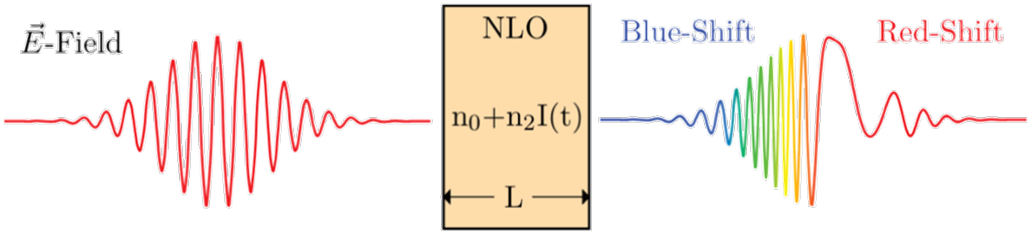

Figure 2.6: SPM of a pulse (left) in a NLO-medium, results in a linear chirped output pulse (right).[5]

2.2.4 Detection

The probe beam after the sample is coupled through an optical fiber to the spectrograph and monitored as a function of wavelength at various delay times after excitation. The MS260i spectrograph of our TAS system, supports automatic adjustment of spectral range and resolution. This is due to the spectrograph's support for up to two output and three gratings. In our TAS system a near infrared (NIR) option is also added. The infrared camera is installed on one output system and the standard UV-Vis camera is installed on the other. The switch between the two output ports can be done automatically by the software, selecting also the most appropriate grating for the task. There are two available gratings:[3]

a) 150 l/mm, 300 nm blaze, resolution 1.95nm

b) 121.6 l/mm, 410 nm blaze, resolution 2.39nm

2.3 State-of-the-art of Transient Absorption Spectroscopy in PSCs

Although in recent decades, the increase of the efficiency in the PSCs has been notable, a full understanding of the ultrafast phenomena that take place in the devices has not been achieved. Indicatively, the charge carrier dynamics, in particular the hole/electron injection from the perovskite film to the transport layers (HTL and ETL, respectively), as well as the recombination pathways of photoexcited charge species have a direct bearing on how effectively light will be converted into electrical current, and vice versa. Furthermore, the crystalline quality of the absorber film and the interaction between the perovskite and HTL and ETL are two crucial parameters that can affect the PCE of the devices. A powerful tool in order to study and explore these ultrafast phenomena is the time-resolved absorption spectroscopy. TAS is a benchmark technique for exploring, understanding and shed light on the carrier transport mechanisms in perovskite solar cells and constitutes a figure-of-merit tool toward their efficiency improvement.

Many groups have already used this technique in order to examine these ultrafast phenomena occurring after the photoexcitation of the PSCs. In particular, Wang et al. observed that the perovskite films with excess PbI_2 show slower recombination rates of the charge-carrier trapping at the perovskite grain boundaries due to the passivation effect of the PbI_2 excess.[6] Latter, Zhu et al. reported faster electron injection in the perovskite film with graphene quantum dots (CQDs), which could effectively compete with carrier trapping and enhance the efficiency of the devices.[7] Furthermore, Zhai et al. have shown that in case of lead halide perovskite both excitons and free carriers are photogenerated at short time unravelling the excitons/photocarries duality nature of neat perovskites with relatively small binding energy at room temperature (RT) (less than k_BT). Moreover, the free carriers following the thermalization process and the transient polarization memory of $MAPbI_3$ are used to estimate

the exciton's diffusion constant.[8] The long exciton diffusion length that Zhai and co-workers obtained indicates that excitons may dissociate at grain boundaries and interfaces at a later time.[8]

Corani et al. have reported that the hole injection form the perovskite layer to the NiO nanoparticles ($NiO_{(np)}$) occur on the sub-ps timescale due to the favorable band alignment between the valence band of the perovskite and $NiO_{(np)}$. The recombination between the holes injected into $NiO_{(np)}$ and the electrons in the perovskite material is shown to be hundreds of ps to few ns. Because the $NiO_{(np)}$ have low conductivity, holes re pinned at the interface and thus, the electrons determine the recombination rate.[9] Ishioka and co-workers study the influence of the employed HTL to the hole injection at the interface of the perovskite layer to the HTL. They found that the hole injection occurs in some picoseconds and is strongly correlated with the enhancement of the efficiency of the devices.[10] Finally, Ghosh et al. reported that the generation of localized hot excitons exhibits a sharp red-shift of the excitonic peak in transient absorption spectra, immediately after photoexcitation. Then, these localized hot excitons are dissociated to the free carrier in ~ 20 fs followed by thermalization, which is compete within 100 fs and the hot carriers cool to lattice temperature through scattering with optic phonons within 0.5 ps.[11]

Except the charge carrier transport, the recombination rates occurring in the PSCs are also crucial and affect the device's performance. For solar cells, the charge carrier lifetime limits the available time of the charges to extract to contacts before one of the recombination occur, making it of the most examined parameter. Wehrenfennig et al. point out the hybrid lead halide perovskites are highly effective materials for photovoltaic application because they combine the high charge-carrier mobilities and low charge-carrier recombination rates.[12] The

combination of these very important parameters leads to unexpectedly long carrier diffusion length due to non-Langevin charge carrier recombination.[12]

Manser et al. have shown that in semiconducting organometal halide perovskites the dominant relaxation pathway is the free electrons and holes recombination following second-order kinetics. In addition, charge accumulation in the perovskite films resulting to an increase in the bandgap following the Burstein-Moss band filling model.[13] The two-body recombination with carrier accumulation is characteristic of an excited states mainly of free carrier, and these free carriers can potentially limit exciton formation by coulombic screening effects.[13] Later, Stranks and co-workers have reported that the charge trapping pathways limit the photoluminescence quantum efficiency (PLQE) at low fluencies, while at high fluencies the traps are predominantly filled and relaxation pathway of the photogenerated species is dominated by radiative recombination processes.[14] Furthermore, they proposed that the high PLQE values at low fluencies can be achieved by filling or removing the traps, and the free carriers versus excitons can be increased from 90% to 100% by minimising the photodoping density occurring due to the presence of subgap states.[14]

Piatkowski et al. attributed the initial ultrafast processes to the exciton-perovskite lattice interactions affected by charge-carrier transfer to the ETL and HTL, preceding the exciton diffusion into free carrier that occur in the sensitizer.[15] Also, they reveal that the contribution of the internal trap states in the recombination is small, thus increasing the probability the charges to survive in the excited perovskite. Furthermore, the nonlinear dependence of the optical band gap on the excited charge density (Burstein-Moss model) suggest the presence presence of the exciton–exciton Auger recombination and ultrafast charge-carrier injection to the ETL and HTL. Finally, they proposed that the optimization in the interface between the

perovskite film and the transporters layers (ETL and HTL) will improve the efficiency of the devices.[15] La-o-vorakiat and co-workers referred that the performance of perovskite devices is governed by the density and mobility of the photogenerated charge-carriers. These parameters show how many free carriers will move away from their origin and how fast, before recombination processes occur.[16] Additionally, their data reveal changes of kinetics from two-body recombination at RT to three-body recombination at low temperatures (LT), as well as the perovskite solar cells can perform well even at LT if the three-body recombination is not predominant.[16] Klein et al. reported that the efficient carrier cooling on a 300 fs timescale after excitation, was observed at low fluencies (~2 mJ cm^{-2}) and this relaxation slow down to around 2.8 ps at high fluencies (50 mJ cm^{-2}). This can be explained by the "hot phonon effect".[17] Finally, Draguta el al. shown that the electron traps in the perovskite film limit the efficiency of the devices, while enhanced carrier trapping resulting to decrease in excited state lifetimes.[18]

In this thesis, for the first time we will correlate the effect of the nature of the HTL surface in the crystallization of the methylammonium lead iodide layer with the dynamic and recombination processes and the efficiency of the perovskite solar cells by means of TAS (**Chapter 4**). Furthermore, we will monitor in-situ the effect of the nature of the HTL surface into the charge carrier dynamics and recombination processes during the crystallization process of the perovskite film (**Chapter 5**) in order to extract useful information for the absorber layer without the entire device being fabricated. Finally, we will perform temperature dependent TAS measurements to obtain information of how the different crystal structures and phases of the $CH_3NH_3PbI_3$ influence the charge carrier dynamics which are strongly related to the power conversion efficiency of the devices (**Chapter 6**).

References:

1. Available at https://old.nobelprize.org/nobel_prizes/chemistry/laureates/1967/
2. Available at http://photobiology.info/Nonell_Viappiani.html
3. Available at https://www.newport.com/f/transient-absorption-spectrometer
4. Available at http://lightcon.com/Product/PHAROS.html
5. Uhlig, S. *Self-organized surface structures with ultrafast white-light: First investigation of LIPSS with supercontinuum.* Springer **2015**.
6. Wang, L.; McCleese, C.; Kovalsky, A.; Zhao, Y.; Burda, C. Femtosecond Time-Resolved Transient Absorption Spectroscopy of $CH_3NH_3PbI_3$ Perovskite Films: Evidence for Passivation Effect of PbI_2. *J. Am. Chem. Soc.* **2014**, *136*, 12205-12208.
7. Zhu, Z.; Ma, J.; Wang, Z.; Mu, C.; Fan, Z.; Du, L.; Yang B.; Fan L.; Yan H.; Phillips D. L.; Yang, S. Efficiency Enhancement of Perovskite Solar Cells Through Fast Electron Extraction: The Role of Graphene Quantum Dots. *J. Am. Chem. Soc.* **2014**, 136, 3760-3763.
8. Zhai, Y.; Sheng; C. X.; Zhang, C.; Vardeny, Z. V. Ultrafast Spectroscopy of Photoexcitations in Organometal Trihalide Perovskites. *Adv. Funct. Mater*. **2016**, *26*, 1617.
9. Corani, A.; Li, M. H.; Shen, P. S.; Chen, P.; Guo, T. F.; El Nahhas, A.; Zheng, K.; Yartsev, A.; Sundstrom, V.; Ponseca Jr, C. S. Ultrafast Dynamics of Hole Injection and Recombination in Organometal Halide Perovskite Using Nickel Oxide as p-Type Contact Electrode. *J. Phys. Chem. Lett* **2016**, *7*, 1096.
10. Ishioka, K.; Barker, B. G.; Yanagida, M.; Shirai, Y.; Miyano, K. Direct Observation of Ultrafast Hole Injection from Lead Halide Perovskite by Differential Transient Transmission Spectroscopy. *J. Phys. Chem. Lett.* **2017**, *8*, 3902.
11. Ghosh, T.; Aharon, S.; Etgar, L.; Ruhman, S. Free Carrier Emergence and Onset of Electron–Phonon Coupling in Methylammonium Lead Halide Perovskite Films. *J. Am. Chem. Soc*. **2017**, *139*, 18262.
12. Wehrenfennig, C.; Eperon, G. E.; Johnston, M. B.; Snaith, H. J.; Herz, L. M. High Charge Carrier Mobilities and Lifetimes in Organolead Trihalide Perovskites. *Adv. Mater*. **2014**, *26*, 1584.
13. Manser, J. S.; Kamat, P. V. Band Filling with Free Charge Carriers in Organometal Halide Perovskites. *Nat. Photonics* **2014** *8*, 737.
14. Stranks, S. D.; Burlakov, V. M.; Leijtens, T.; Ball, J. M.; Goriely, A.; Snaith, H. J. Recombination Kinetics in Organic-Inorganic Perovskites: Excitons, Free Charge, and Subgap States. *Phys. Rev. Appl.* **2014**, *2*, 034007.
15. Piatkowski, P.; Cohen, B.; Ramos, F. J.; Di Nunzio, M.; Nazeeruddin, M. K.; Grätzel, M.; Ahmad, S.; Douhal, A. Direct Monitoring of Ultrafast Electron and Hole Dynamics in Perovskite Solar Cells. *Phys. Chem. Chem. Phys*. **2015**, *17*, 14674.
16. La-o-vorakiat, C.; Salim, T.; Kadro, J.; Khuc, M. T.; Haselsberger, R.; Cheng, L.; Xia, H.; Gurzadyan, G. G.; Su, H.; Lam, Y. M.; Marcus, R. A.; Michel-Beyerle, M. E.; Chia, E. E. M. Elucidating the Role of Disorder and Free-Carrier Recombination Kinetics in $CH_3NH_3PbI_3$ Perovskite Films. *Nat. Commun*. **2015**, *6*, 7903.

17. Klein, J. R.; Flender, O.; Scholz, M.; Oum, K.; Lenzer, T. Charge Carrier Dynamics of Methylammonium Lead Iodide: from PbI_2-rich to Low-Dimensional Broadly Emitting Perovskites. *Phys. Chem. Chem. Phys*. **2016**, *18*, 10800.
18. Draguta, S.; Christians, J. A.; Morozov, Y. V.; Mucunzi, A.; Manser, J. S.; Kamat, P. V.; Luther, J. M.; Kuno, M. A Quantitative and Spatially Resolved Analysis of the Performance-Bottleneck in High Efficiency, Planar Hybrid Perovskite Solar Cells. *Energy Environ. Sci.* **2018**, *11*, 960.

Chapter 3

Sample Preparation and Techniques

In this Chapter, the sample fabrication and the employed characterization techniques are presented. In particular, in **Section 3.1** it is described the fabrication procedure for the perovskite solar cells, while in **Sections 3.2** and **3.3** the fabrication procedures for the samples that were used in in-situ TAS annealing studies, and for the temperature dependent TAS measurements, respectively, are described. The main technique of this thesis is described extensively in **Chapter 2**. Finally, in **Section 3.4** the additional techniques that were used are explained. The fabrication of the samples and the electrical characterization were taken place in "Emerging Nanomaterials & Devices Group" of Prof. Emmanuel Kymakis in Department of Electrical & Computer Engineering of the Hellenic Mediterranean University.

3.1 Fabrication of PSC Devices

Perovskite films were prepared on 20 x 15 mm pre-patterned indium tin oxide (ITO) coated glass substrates (Naranjo Substrates) and a sheet resistance of ~20 Ω sq^{-1}. A three-step cleaning procedure with deionized water, acetone, isopropanol was followed to clean the substrates from any impurities.[1] Following this, the substrates were transferred inside an ultraviolet ozone cleaner in order to increase the hydrophilicity on the surface of ITO/glass substrate and to remove organic residues. Subsequently, the ITO/glasses were ready for the deposition of the PEDOT:PSS or PTAA HTL polymers.

For the samples where PEDOT: PSS was used as HTL, the polymer was spin coated on the ITO surface from aqueous solution (4000 rpm for 60 s), followed by a thermal annealing at

120 ^{o}C for 15 minutes in ambient conditions and 30 more minutes inside a nitrogen-filled glovebox at 120 °C. A result of this spin-coated process was a ~30 nm layer thickness.[1-3] For samples with the other employed HTL polymer, a solution of PTAA powder in toluene (7mg ml^{-1}) doped with 1.5 % wt tetrafluoro-tetracyanoquinodimethane was prepared and spin coated (4000 rpm for 35 s) on the ITO surface and annealed at 110 ^{o}C for 10 minutes. After the HTL deposition in both cases, the substrates were left to cool down to room temperature (RT).

Perovskite film fabrication took place inside the nitrogen-filled glove box. The methylammonium lead iodide ($CH_3NH_3PbI_3$) films were prepared by a typical solution-based two-step procedure. For this purpose, two anhydrous solution were prepared separately. The first solution was prepared by dissolving lead iodide (PbI_2) in dimethylformamide (DMF) and stirred overnight at 75 ^{o}C, while the second one, by dissolving methylammonium iodide (CH_3NH_3I) in isopropanol and stirring at room temperature. In step one, the solution (PbI_2) (450mg ml^{-1}) was spin coated on the HTL and heated at 100 ^{o}C for 10 minutes. For the thermal annealing configurations, in step two the CH_3NH_3I solution (45mg ml^{-1}) was spin coated on top of the surface of PbI_2 and heated immediately at 100 ^{o}C for 30 minutes. This was the final step for the preparation of HTL/$CH_3NH_3PbI_3$ architectures synthesized upon following the typical thermal annealing (TA) crystallization procedure (TA samples). The thickness of the perovskite layer for TA was measured to be ~350 ± 50 nm when PEDOT:PSS is used and ~450 ± 50 nm when PTAA is employed. Before ETL deposition, the samples were once more allowed to cool down to room temperature. For the formation of the ETL, PCBM powder was dissolved in chlorobenzene and stirred for at least 5 h at 75 ^{o}C, with a concentration of 20 mg ml^{-1}. The PCBM solution was spin coated on the perovskite surface at 1000 rpm for 45 s, and left to

dry for 30 min in a closed petri dish under inert atmosphere. Next, an as-prepared PFN solution of 0.4 mg ml^{-1} in methanol with a small amount of acetic acid (0.4 μl ml^{-1}) was spin coated at 2000 rpm for 45 s for the formation of an ultrathin interlayer. Finally, 100 nm of aluminum was deposited through a shadow mask by thermal evaporation to provide active area electrodes of 4 mm^2 for each component device. The device architecture of the planar inverted perovskite solar cells that used to the electrical measurements is depicted in **Figure 3.1(a)**, while **Figure 3.1(b)** shows the device components that used for the TAS measurements.

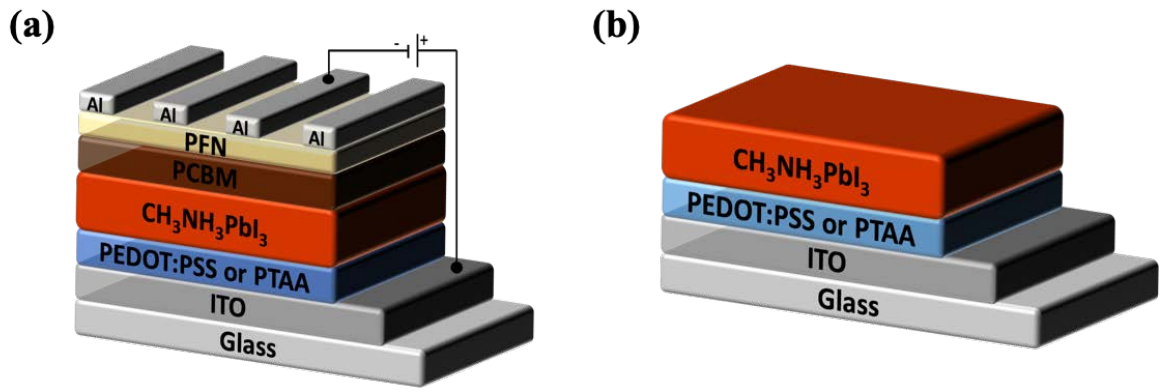

Figure 3.1: (a) Device architecture used for the electrical characteristics and **(b)** Device components that used for TAS measurements.

3.2 Development of Perovskite/HTL Architectures for In-situ TAS Studies

For this set of samples, the procedure until the spin coating of the methylammonium iodide solution upon the lead iodide, was the same as it is described in the previous section. For the corresponding samples prepared for the in-situ TAS (IS samples), after the CH_3NH_3I solution was casted (step 2), the samples remained at RT for 30 minutes in inert conditions, before heated at the desired temperatures of 90, 100 and 110 ^oC, with a heating rate of 20 ^oC/minute, while TAS measurements were performed every 10 minutes after the selected annealing temperature was reached. For the sake of convenience, all crystallization

parameters for the fabricated HTL/$CH_3NH_3PbI_3$ samples are summarized in Table 1. The thickness of the perovskite layer for IS samples at 100 ^oC was measured to be ~350 ± 50 nm when PEDOT:PSS is used and ~450 ± 50 nm when PTAA is employed. We assume that the thickness of the perovskite layer will be equal also at 90 ^oC and 110 ^oC, as the concentration of the solution and the deposition conditions remained the same. In the set of IS samples, we have changed the crystallization temperature and the same time the annealing period. The perovskite precursors/HTL architecture that used for the in-situ TAS study is presented **Figure 3.2**.

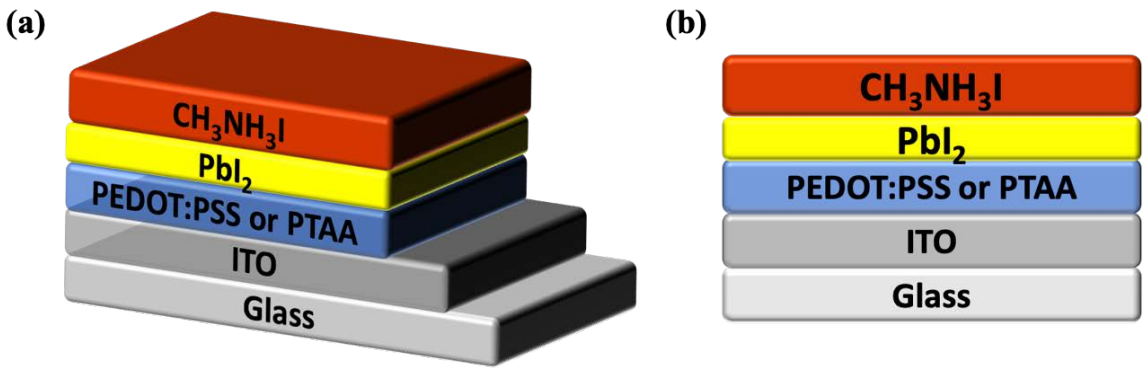

Figure 3.2: (a) Perovskite precursors/HTL architecture and **(b)** Cross-section of this architecture for in-situ TAS study.

Table 3.1: HTL/$CH_3NH_3PbI_3$ Sample Configurations and Corresponding Synthesis Parameters.

Samples	HTL polymers	Crystallization parameters	Annealing Temperature
1	PEDOT:PSS	Thermal Annealing	100 ^oC
2	PEDOT:PSS	In-situ TAS Annealing	90 ^oC
3	PEDOT:PSS	In-situ TAS Annealing	100 ^oC
4	PEDOT:PSS	In-situ TAS Annealing	110 ^oC
5	PTAA	Thermal Annealing	100 ^oC
6	PTAA	In-situ TAS Annealing	90 ^oC
7	PTAA	In-situ TAS Annealing	100 ^oC

8	PTAA	In-situ TAS Annealing	110 ^{o}C

3.3 Development of Perovskite/HTL Architectures for Temperature Dependent TAS Study

For this set of samples, the procedure until the final step for the preparation of HTL/$CH_3NH_3PbI_3$ architectures through the typical thermal annealing (TA) crystallization procedure (TA samples), was the same as it is described in **Section 3.1** and is depicted in **Figure 3.1(b)**. After this final step the samples were allowed to cool down to room temperature. Then the HTL/perovskite configurations were placed in the Janis VPF-100 Cryostat (Figure), which have its own liquid nitrogen 400 ml storage dewar in order to perform the temperature dependent TAS measurements. Firstly, using a combination of a mechanical and a turbo pump, we evacuate the chamber of the cryostat to a pressure of 10^{-5} Torr which is sufficient for LN measurements. Then, the temperature of the samples is controlled with a two-channel temperature controller (Model 335, Lake Shore Cryotronics) with configurable heater outputs delivering a total 75W of low noise heater power. The total cryogenic system is depicted in **Figure 3.3**. The temperature dependent TAS measurements were performed from 85 K up to 250 K.

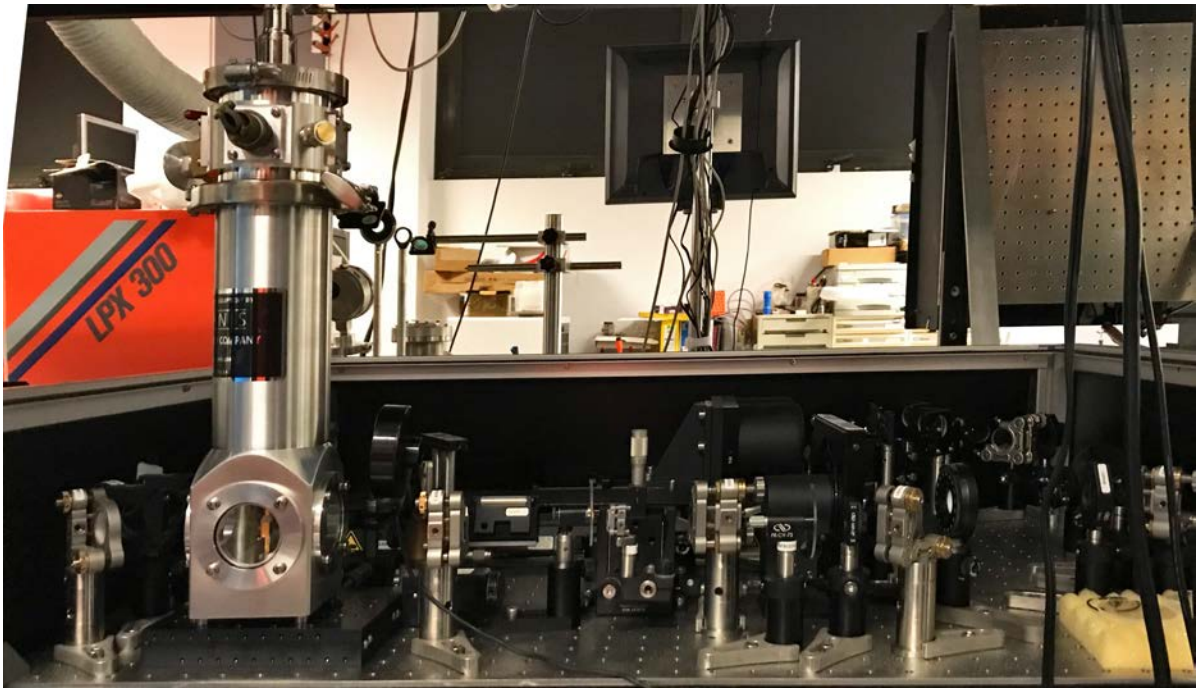

Figure 3.3: Janis VPF-100 cryostat, integrated into the TAS setup.

3.4 Device and Perovskite/HTL Architecture Characterization

3.4.1 Electrical Measurements

The performances of the fabricated devices were measured under inert atmosphere with an Air Mass 1.5 Global (A. M. 1.5 G) solar simulator at an intensity of 100 mW cm^{-2} using an Agilent B1500A Semiconductor Device Analyzer. The external quantum efficiency measurements were conducted immediately after device fabrication at encapsulated PSCs using an integrated system (Enlitech, Taiwan) and a lock-in amplifier with a current preamplifier under short-circuit conditions. The light spectrum was calibrated using a monocrystalline photodetector of known spectral response. The PSCs were measured using a Xe lamp passing through a monochromator and an optical chopper at low frequencies (≈200 Hz) in order to maximize the signal/noise (S/N) ratio.

3.4.2 Crystal Structure

X-ray Diffraction (XRD): The crystal structure of the fabricated $CH_3NH_3PbI_3$ perovskite films were studied by an X-Ray Rigaku (RINT-2000) Diffractometer operating with a continuous scan of Cu Ka1 radiation with λ = 1.54056 Å. All XRD measurements were performed with a scan rate of 0.1^o/s in the range of $2\theta = 5^o - 60^o$.[4]

Atomic Force Microscopy (AFM): The topography and roughness of the HTLs were examined by means of atomic force microscopy (AFM), by employing a Park XE-7 instrument in tapping mode. All AFM measurements were performed with a scan rate of 0.3 Hz, while the total area of each scan was 1x1μm. A field emission scanning electron microscope (JEOL, JSM-7000F), was used to examine the morphology of the perovskite structures.[5]

3.4.3 Optical Measurements

Micro-photoluminescence (μ-PL): The spectra were collected in a backscattering setup shown in **Figure 3.4**. Two different excitation sources were used: a) continuous wave (CW) He- Ne 543nm (photon energy: 2.28eV) which is not resonant with the optical gap of monolayer WS2 and b) He-Ne 594nm (photon energy: 2.09eV) which produces resonant excitation. Both laser beams have an s-polarization and pass through a spatial filter (KT310, Thorlabs) for two reasons: the first is to clean the Gaussian beam from its spatially varying intensity noise and acquire a uniform energy distribution. The second is to expand the beam size in order to fit through the aperture of the objective and achieve diffraction limited spot size. After the spatial filter, the beams pass through a short pass (SP) filter (FESH550 for the 543nm laser beam and FESH600 for the 594nm laser beam, Thorlabs) to reduce the noise at higher wavelengths. The power of the laser beams is controlled via a neutral density (ND) filter (0-2 OD, NE520B-A, Thorlabs). A 50:50 beam splitter (BS 50:50, BSW10, Thorlabs) is

used to reflect and drive the beam to the objective lens. A Mitutoyo 50x (NA:0.42, f=200mm) focuses down to ~1μm the spot size for the sample excitation. The position of the sample is controlled with a XYZ mechanical translation stage (PT3, Thorlabs) and the excitation procedure is continuously monitored and controlled via a CCD optical setup. Following the excitation, the emitted PL signal passes through a long pass (LP) filter (FELH550 for the 543nm laser and FELH600 for the 594nm laser, Thorlabs) to eliminate the emission of the laser.[6]

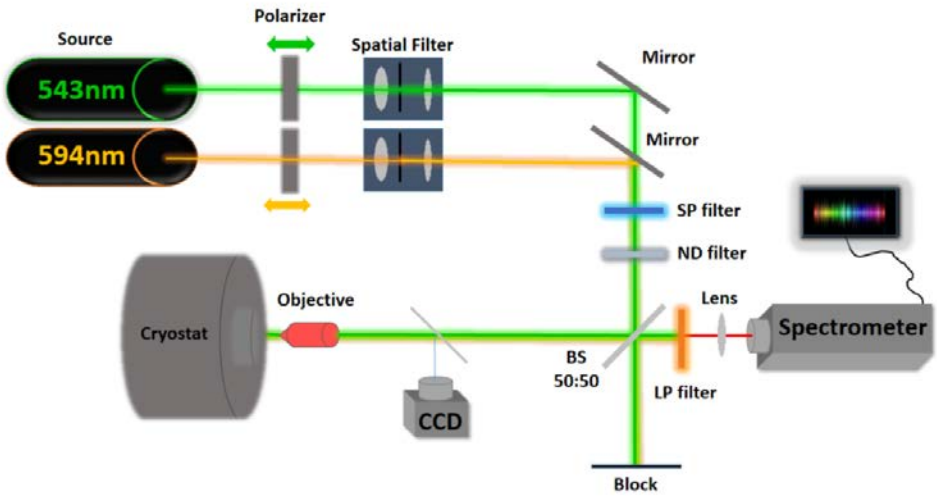

Figure 3.4: Schematic representation of the μPL configuration. Figure is taken from reference 6.

<u>Ultraviolet-Visible Spectroscopy (UV-Vis) – Transmittance:</u> A PerkinElmer UV/vis (Lambda 950) spectrometer was used to measure the absorption of the fabricated HTL/$CH_3NH_3PbI_3$ films over the wavelength range of 430−900 nm.[7] The transmittance spectra were recorded using a Shimadzu UV-2401 PC spectrophotometer over the wavelength range of 300–800 nm.[8]

References:

1. Kakavelakis, G.; Maksudov, T.; Konios, D.; Paradisanos, I.; Kioseoglou, G.; Stratakis, E.; Kymakis, E. Efficient and Highly Air Stable Planar Inverted Perovskite Solar Cells with Reduced Graphene Oxide Doped PCBM Electron Transporting Layer. *Adv. Energy Mater.* **2016**, *7*, 1602120.
2. Serpetzoglou, E.; Konidakis, I.; Kakavelakis, G.; Maksudov, T.; Kymakis, E; Stratakis, E. Improved Carrier Transport in Perovskite Solar Cells Probed by Femtosecond Transient Absorption Spectroscopy. *ACS Appl. Mater. Interfaces*, **2017**, *9*, 43910.
3. Konidakis, I.; Maksudov, T.; Serpetzoglou, E.; Kakavelakis, G.; Kymakis, E.; Stratakis, E. *ACS Appl. Energy Mater.* **2018**, *1*, 5101.
4. Available at https://www.rigaku.com/
5. Available at https://www.parksystems.com/index.php/products/small-sample-afm/park-xe7/overview
6. Paradisanos, I. (2018). *Excitons in atomically thin tungsten disulfide (WS_2) layers.* (Doctoral Dissertation) University of Crete, Physic Department, Heraklion, Greece.
7. Available at http://www.perkinelmer.com/
8. Available at https://www.shimadzu.com/

Chapter 4

Improved Carrier Transport in PCSs Probed by fs-Transient Absorption Spectroscopy

For the samples of this Chapter, the $CH_3NH_3PbI_3$ perovskite thin films have been deposited on glass/indium tin oxide (ITO)/Hole Transport Layer (HTL) substrates, utilizing two different materials as the HTLs (**Figure 4.1**).

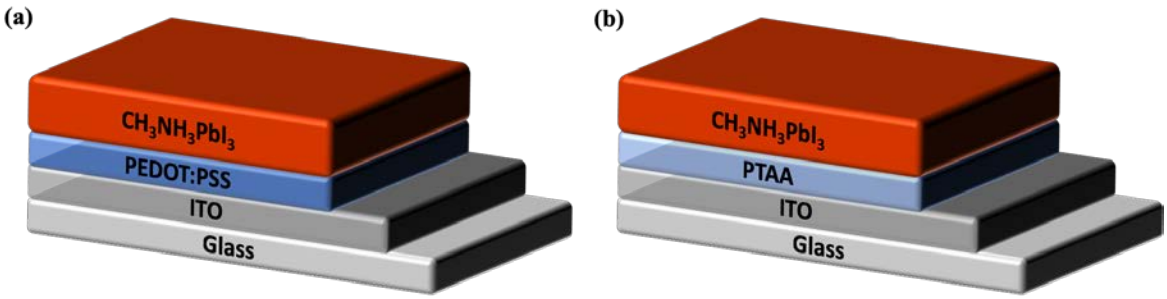

Figure 4.1: Schematic illustration of the two configurations **(a)** PEDOT:PSS/$CH_3NH_3PbI_3$ and **(b)** PTAA/$CH_3NH_3PbI_3$ that used in this study.

In the first configuration, the super hydrophilic polymer poly (3,4-ethylenedioxythiophene)-poly (styrenesulfonate), known as PEDOT:PSS, was employed as the HTL material, while on the second case the non-wetting poly (triarylamine) semiconductor polymer, known as PTAA was used. It was found that when PTAA is used as HTL material the averaged power conversion efficiency (PCE) of the perovskite solar cells remarkably increases from 12.60% to 15.67%. In order to explore the mechanism behind this enhancement, the aforementioned perovskite/HTL arrangements were investigated by time resolved transient absorption spectroscopy (TAS) performed under inert conditions. By means of TAS, the charge transfer,

carrier trapping and holes injection dynamics from the photo-excited perovskite layers to the HTL can be directly monitored via the characteristic bleaching profile of the perovskite at ~750 nm. TAS studies revealed faster relaxation times and decay dynamics when the PTAA polymer is employed, that potentially account for the enhanced PCE observed. The TAS results are correlated with the structure and crystalline quality of the corresponding perovskite films, investigated by scanning electron microscopy (SEM), X-ray diffraction (XRD), atomic force microscopy (AFM), microphotoluminescence (μPL) and transmittance spectroscopy.

4.1 Introduction

Recent scientific approaches focus on two major aspects. First, introduce ways and cell architectures in order to maximize the PCEs of PSCs, while at the same time, overcome the drawbacks of the perovskite.[1-4] Numerous studies focus on the composition and synthesis protocols of the perovskite itself, as it is generally acknowledged that the crystalline quality and the interface between the absorber film and the transport layers play a fundamental role on the device performance.[5-12] Along similar lines, other studies emphasize the importance of various fabrication procedures that include among others, one-step and two-step deposition protocols,[13-15] crystal formation via solution and vapor deposition processes,[16-20] and rapid laser annealing crystallization techniques.[11,12]

On a rather different manner, aiming to enhance efficiency while improving device lifetime, significant attention has been paid on the selection of suitable hole transport layer (HTL) and electron transport layer (ETL) conductive materials. Among the available choices for the HTL component, are the polymers poly (3,4-ethylenedioxythiophene)-poly (styrenesulfonate), known as PEDOT:PSS, and the poly (triarylamine), known as PTAA,

while [6,6]-Phenyl-C61-butyric acid methyl ester, known as PCBM, is widely used as an ETL. The interactions between HTL/perovskite and perovskite/ETL interfaces are crucial in terms of minimizing factors that are known to reduce PSCs efficiency, such as the formation of light activated charge states and ion migration in the perovskite crystal lattice.[4,21,22] Aiming to resolve these alarming degradation sources, recent studies report on the appropriate doping of PTAA and PCBM polymeric conductors with ingredients that increase conductivity properties while improving stability.[23,24] For the same objective, other studies focus directly on the effect of HTL and ETL material properties and characteristics on the device performance and stability.[6,25-27] Among other reports, it was recently highlighted by Bi et al. that the employment of the non-wetting PTAA polymer as HTL significantly improves the efficiency of the PSC devices.[27] However, no clear evidence on the origins of such efficiency improvement has been reported to date.

In this Chapter, we thoroughly correlate the obtained morphological differences of the perovskite active layer film upon employing different HTLs with the charge extraction processes and the corresponding transient decay dynamics that are probed by means of femtosecond time-resolved transient absorption spectroscopy (TAS). These processes are well-acknowledged to play a fundamental role on the performance of PSC devices of this configuration. It is firstly revealed, that the morphology of the perovskite film strongly depends on the type of HTL material. More importantly, it is discovered that upon using a more hydrophobic HTL polymer, not only the morphology of the perovskite film improves, but even more strikingly, the HTL/perovskite charge extraction processes are accelerated, while on the same time the corresponding recombination processes become slower. Both these factors favor significantly the PCE of the PSCs in question, and thus, our recent findings point out one plausible approach towards maximizing the efficiency of such devices.

Although TAS has been recently employed for the study of the transport properties in PSCs,[25,28-33] the measurements were performed in ambient air, which are known to be detrimental for the perovskite layer, mostly due to its instability against humidity.[1,2] In the present case, however, TAS measurements were performed entirely under inert conditions. In particular, we compare two types of PSC devices using identical $CH_3NH_3PbI_3$ absorber, but a hydrophilic, PEDOT:PSS, and a more hydrophobic PTAA HTL respectively. TAS measurements reveal faster charge carrier dynamics and relaxation component times and slower recombination processes for the PTAA/perovskite, relatively to the corresponding PEDOT:PSS/perovskite architecture, which could account for the enhanced PCE of the device in which the former configuration is used. The TAS findings are further complemented by electron and atomic force microscopy, as well as photoluminescence and transmittance spectroscopy studies, aiming to shed light on the effect of the applied HTL material on the perovskite layer structure and morphology. It is evidenced that such unique correlation of carrier relaxation dynamics and structural morphology, demonstrated here, could be beneficial towards efficiency enhancement of state-of-the-art PSCs.

4.2 Results and Discussion

4.2.1 Structural and Morphological characterization

The efficiency of PSCs is always correlated with the proper formation of the hybrid perovskite absorber and differences in the crystal structure, grain size and grain boundaries, of the perovskite could significantly affect the devices performance.[33] In this way, the structural and morphological characteristics of the $CH_3NH_3PbI_3$ perovskite layer upon its growth on the two different types of HTL polymers (PEDOT:PSS and PTAA) was investigated. In a first step, the change of the crystalline structure of the perovskite film was investigated by XRD. Both XRD profiles are dominated by two main peaks at 14° and 28.4^o,

corresponding to the (110) and (220) lattice planes of the $CH_3NH_3PbI_3$ perovskite, respectively.[11,19,25,34] While, the much weaker signatures at 24.4° and 31.8° are respectively attributed to the (202) and (310) crystal reflections. It can be concluded that XRD patterns (**Figure 4.2**) reveal no obvious changes on the quality of the $CH_3NH_3PbI_3$ perovskite crystal upon using HTL substrates of reduced wettability.

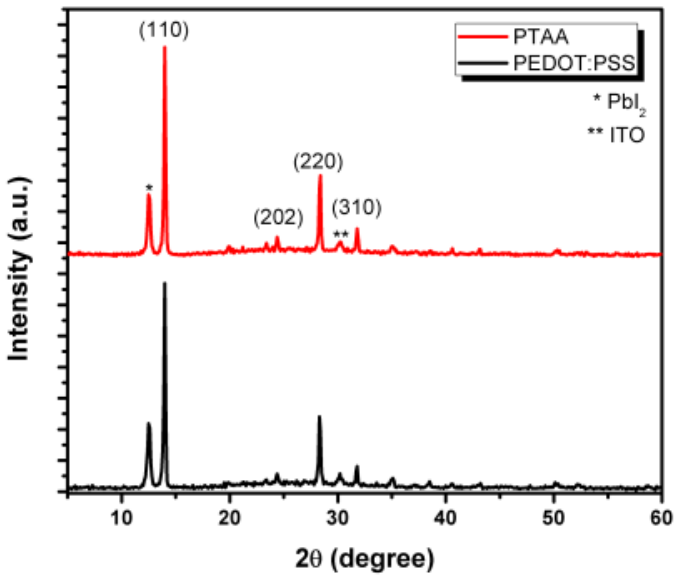

Figure 4.2: XRD patterns for PEDOT:PSS/$CH_3NH_3PbI_3$ (black line) and PTAA/$CH_3NH_3PbI_3$ (red line) architectures.

Considering the lack of differences between the XRD patterns of the perovskite films onto PTAA and PEDOT:PSS layers, scanning electron microscopy (SEM) was employed to further shed light on the morphology of the perovskite structure, while atomic force microscopy (AFM) was performed to reveal the nature of the employed HTL surfaces. In particular, **Figure 4.3(a-b)** present the AFM images of PEDOT:PSS and PTAA polymer surfaces, prior to the growth of the perovskite layer, while corresponding analysis reveals average roughness values of 0.942 and 0.580 nm, for the PEDOT:PSS and PTAA surfaces,

respectively. Furthermore, **Figure 4.3(c-d)** show SEM photos of the $CH_3NH_3PbI_3$ perovskite grown onto PEDOT:PSS and PTAA layers, respectively. Strikingly enough, it becomes apparent from SEM images inspection, that the perovskite formed on the smoother PTAA layer exhibits considerably larger grains, which are known to favor the electric performance of the PSC device, mainly due to reduced trap assisted recombination, which significantly affects the V_{oc} value.[11,27] Notably, it appears that such differences in the perovskite crystalline morphology were not traceable by means of XRD analysis, in agreement with recent findings of Bi et al.,[27] where it is also reported the identical XRD patterns for both PEDOT:PSS/$CH_3NH_3PbI_3$ and PTAA/$CH_3NH_3PbI_3$ designs, while having dissimilar crystal grains morphology.

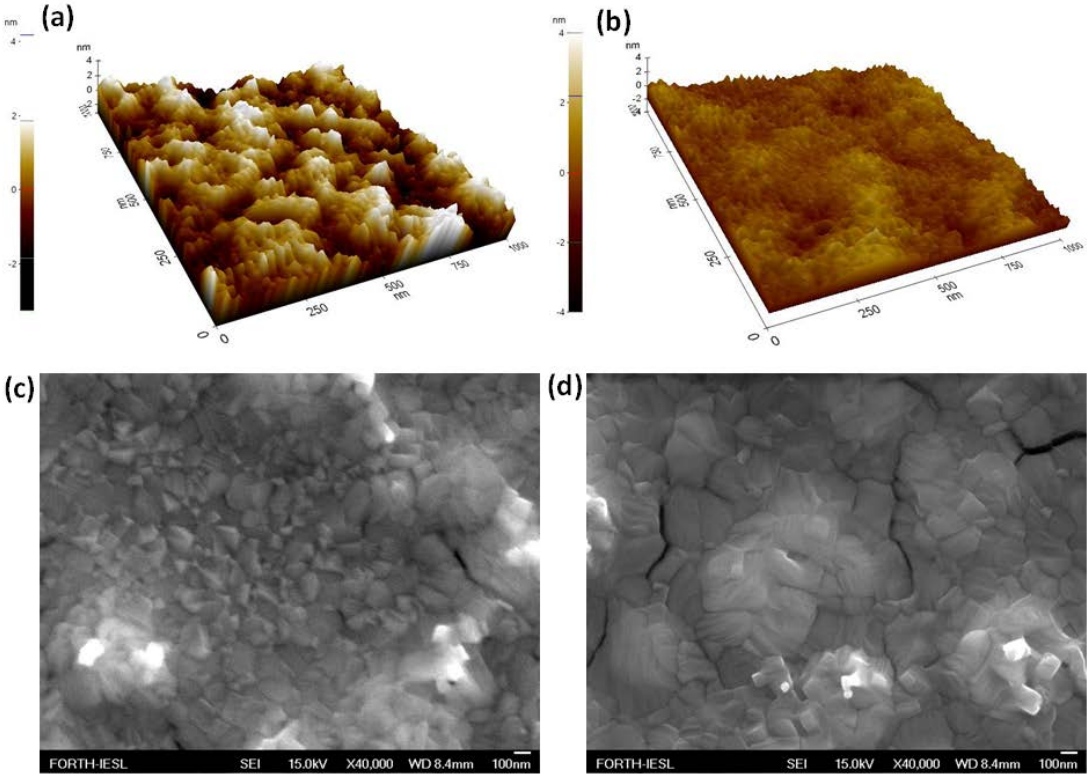

Figure 4.3: Atomic force microscopy (AFM) surface profiles of PEDOT:PSS **(a)** and PTAA **(b)** polymers prior to $CH_3NH_3PbI_3$ perovskite deposition. Scanning electron microscopy (SEM) photos of the $CH_3NH_3PbI_3$ perovskite structure grown on PEDOT:PSS **(c)** and PTAA **(d)** hole transport layers.

Moreover, the contact angles of water on PEDOT:PSS and PTAA polymers synthesized for the needs of the present study following standard synthetic protocols were measured several times and found to be equal to 20° and 40° ($\pm 1^o$) respectively (**Figure 4.4**), i.e. both well within the hydrophilic regime. While the recent report by Bi et al. attributes the formation of larger perovskite grains on surfaces with reduced wettability and good smoothness, there was no evidence, to date, about which of the two factors plays the more fundamental role on prompting the formation of larger perovskite crystal grains. However, findings of the present study reveal clear evidence that the HTL surface smoothness is indeed the dominant factor for granting a better substrate for the formation of larger and more uniform grains, and thus, for the realization of PSCs with enhanced performances. Thus, it is widely accepted that the HTL surface roughness strongly correlates with the recombination rates, with surfaces of higher roughness exhibiting slower recombination dynamics being the typical behavior.[35,36]

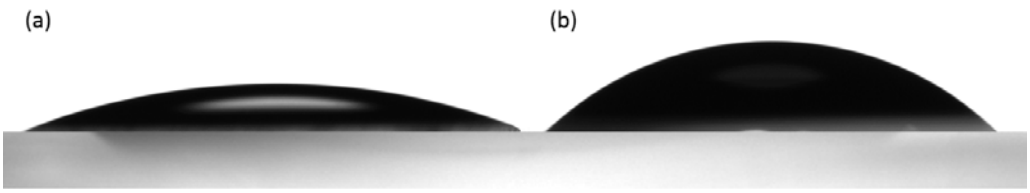

Figure 4.4: Photographs of the shape of a 5 μL de-ionized water droplet on PEDOT:PSS **(a)** and PTAA **(b)** polymer substrates that provide the corresponding contact angles.

4.2.2 Optical and Electrical characterization of the PSCs

The most important role of the HTL in PSC, which is illustrated in **Figure 4.5(a**), is to prevent the recombination at the semiconductor/electrode interface, and in turn to facilitate the hole extraction at the respective electrode of the device. Thus, prior to the fabrication and characterization of PSCs, we studied the PL characteristics of PEDOT:PSS or

PTAA/$CH_3NH_3PbI_3$ in order to have an indication regarding the hole extraction among the two different samples. **Figure 4.5(b)** presents the μ-PL spectra of both systems, where one can observe significant quenching (~20%) for the PTAA architecture relatively to the PEDOT:PSS one, accompanied with negligible shift of the μPL peak. This finding suggests that upon introducing the smoother and more hydrophobic PTAA polymer, the charge transport dynamics at the HTL/perovskite interface are accelerated,[24,28] and an enhancement in the device short circuit current (J_{sc}) density is expected. It should be noted that identical μPL spectra were recorded at several spots across the samples surface, suggesting homogeneous PL characteristics.

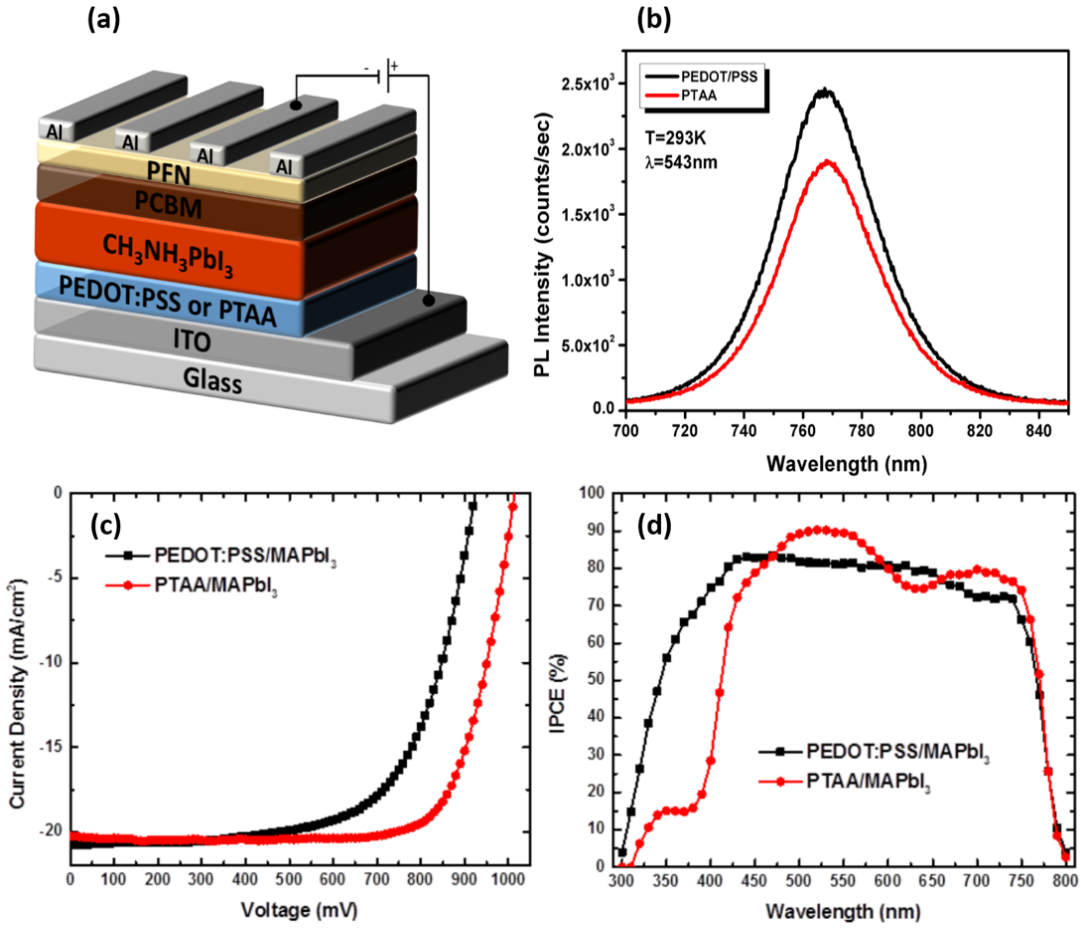

Figure 4.5: (a) Device architecture of the fabricated planar inverted perovskite solar cells (PSCs). **(b)** Microphotoluminescence (μPL) spectra following excitation at 543 nm of PEDOT:PSS/$CH_3NH_3PbI_3$ and PTAA/$CH_3NH_3PbI_3$ architectures. **(c)** Current density-voltage (J-V) curves of PSCs measured under A. M. 1.5 G (100 mW cm^{-2}) illumination, and **(d)** corresponding external quantum efficiency (EQE) spectra.

Figure 4.5(c) presents the current density-voltage (J-V) curves for the two types of fabricated PSCs, i.e. with PEDOT:PSS and PTAA polymers as HTL. The J–V characteristics plotted for forward and reverse bias scan (**Figure 4.6**), indicate the absence of the hysteresis effect for both types of devices tested. The averaged PV characteristics together with the standard deviations, extracted from 24 identical cells for each case, are summarized in **Table 4.1**.

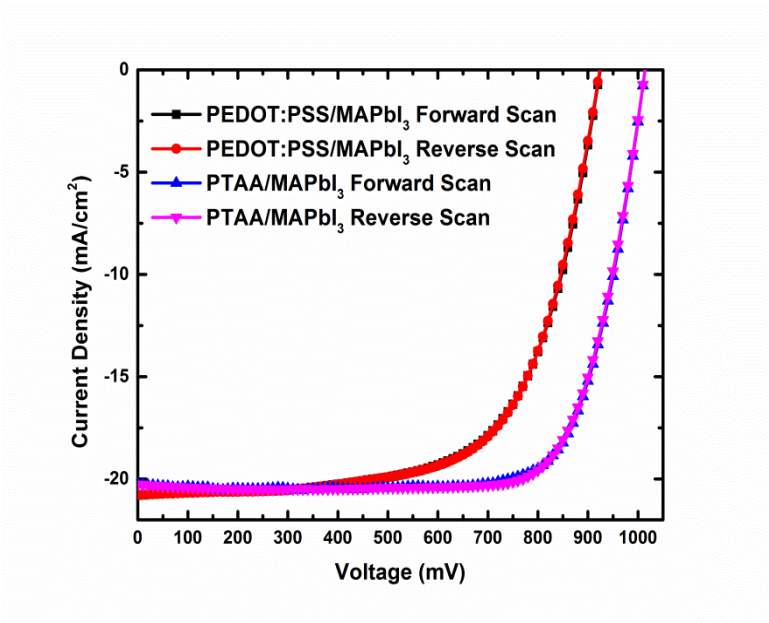

Figure 4.6: J-V curves of the PEDOT:PSS and PTAA HTM based PSCs with both forward (black and blue) and reverse (red and magenta) scan of the applied voltage.

Table 4.1: Summary of the average photovoltaic characteristics of $CH_3NH_3PbI_3$ based perovskite solar cells with PEDOT:PSS and PTAA polymers as hole transport layer.

HTL polymer	J_{sc} (mA cm^{-2})	J_{sc} Calculated IPCE	V_{oc} (mV)	FF (%)	PCE (%)
PEDOT:PSS	20.79±0.39	19.88	926±19	65.46±1.03	12.60±0.71
PTAA	20.24±0.44	19.15	1010±11	76.67±0.69	15.67±0.66

Surprisingly, and in contradiction to the PL characteristics, the J_{sc} of the PTAA based devices was comparable with the J_{sc} of the PEDOT:PSS based devices. On the other hand, upon PTAA incorporation, a noteworthy improvement in the V_{oc} is observed as it increases from

926 to 1010 mV, accompanied by a remarkable enhancement in the fill factor (FF) from 65.5% to 76.7%. The significant enhancement in the open circuit voltage (V_{oc}) value of PTAA based devices can be directly correlated with the higher formed grains size of the $CH_3NH_3PbI_3$ compared to the lower grains formed when PEDOT:PSS is used as HTL.[19] However, one cannot exclude the contribution to the observed V_{oc} enhancement, attributed to the improved PTAA-perovskite energy alignment, compared to the PEDOT:PSS-perovskite one, as depicted in **Figure 4.7**. While, the enhancement in the fill factor (FF) can be directly correlated with the importantly decreased series resistance (R_s) values of the PTAA based devices (5.83 Ω cm) compared with the PEDOT:PSS based devices (7.23 Ω cm). A notable improvement of V_{oc} (~9%) and FF (~17%) leads to a considerable PCE enhancement of ~24% (**Table 4.1**), with final averaged PCEs of 15.67 and 12.60% for the PTAA and PEDOT:PSS based devices, respectively. The detailed statistics clearly display that the power conversion efficiency for all devices were improved when the PTAA was used as HTL.

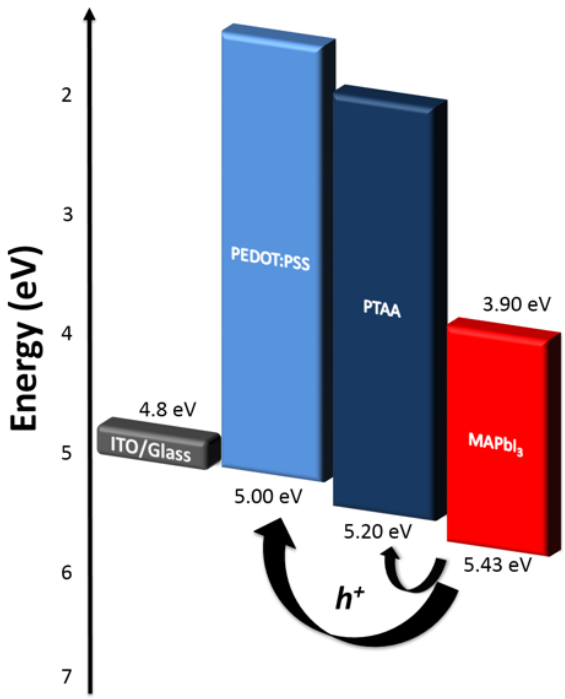

Figure 4.7: Schematic representation of energy levels of the studied HTL polymers, PEDOT:PSS and PTAA, and $CH_3NH_3PbI_3$ perovskite as designed from values extracted from the literature.

Figure 4.2(d) displays the corresponding external quantum efficiency (EQE) spectra for the PTAA and PEDOT:PSS HTL based devices. In particular, compared to the PEDOT:PSS, the EQE of the PTAA HTL is enhanced in the ranges 470 to 600 nm and 670 to 770 nm, while it is reduced from 300 to 470 nm and 600 to 670 nm. Notably, the calculated J_{sc} obtained from the EQE measurements, matches well to the actual measured J_{sc} for the two devices (**Table 4.1**) indicating the good accuracy of the electrical measurements performed. By carefully comparing the shape of the EQE spectra of the two different based HTL PSCs, we detected an unexpected lower response of the PTAA PSCs at wavelengths below 470 nm, as compared to PEDOT:PSS based devices. The EQE results triggered us to study and compare the transmittance spectra of the PTAA and PEDOT:PSS coated glass/ITO substrates, since it is the only way to explain this important difference at lower wavelengths of the EQE spectra and could possibly explain the mismatch of the I-V and PL measurements. However, before comparing the transmittance spectra of PTAA and PEDOT:PSS, it is vital to emphasize the practical difference on how the I-V and PL measurements were conducted; on the one hand for the I-V measurements, the solar light passes through the glass/ITO/HTL substrates before reaches the $CH_3NH_3PbI_3$ absorber, while for the PL measurements, the monochromatic light used as excitation source, directly passes through $CH_3NH_3PbI_3$ absorber (without passing through the ITO/HTL substrates). Based on the above, the contradiction between the I-V and PL measurements in the systems studied, is due to an increased parasitic absorption induced in the front surface of the cell upon incorporation of the PTAA instead of PEDOT:PSS HTL, reducing in this way the amount of photons reaching the $CH_3NH_3PbI_3$ absorber, that is present only for the I-V measurements. In this way, we measured and presented the comparison between the transmittance spectra of ITO/PTAA or ITO/PEDOT:PSS substrates. As it can be easily observed in Figure S6, by using the PTAA hole transporter the transmission of the light is significantly decreased if compared with the PEDOT:PSS hole

transporter. Taking this into account, the introduction of PTAA as the HTL indeed increases the parasitic absorption of the front surface, the J_{sc} of the respective devices could be significantly higher if PTAA and PEDOT:PSS polymers exhibited similar transparency, i.e. which is indeed not the case (**Figure 4.8**).

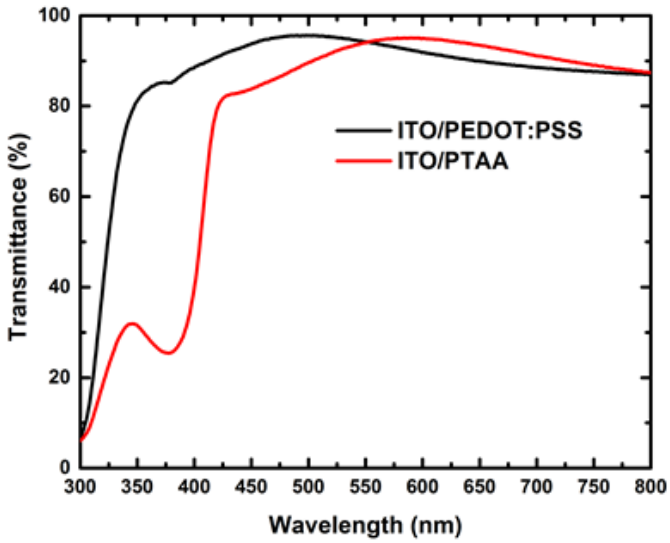

Figure 4.8: Comparison of transmittance spectra between the PTAA and PEDOT:PSS coated glass/ITO substrates.

4.2.3 Transient absorption spectroscopy (TAS) studies

In order to identify the origins of the enhanced performance upon using PTAA instead of PEDOT:PSS as HTL, the carrier transport dynamics of the PEDOT:PSS/$CH_3NH_3PbI_3$ and PTAA/$CH_3NH_3PbI_3$ systems were thoroughly investigated by TAS and correlated with the photovoltaic characteristics, i.e. J_{sc}, V_{oc} and FF. The TAS technique is considered to be a powerful tool for extracting information regarding charge carrier transfer, recombination dynamics and relaxation times in PSCs.[25,28,29-32,37-41] However most of TAS studies reported to date have been performed in ambient air conditions. On the contrary, all TAS measurements we report here were performed using a specially designed homemade cell, enabling us to maintain inert atmospheric conditions throughout the whole measurement

duration, i.e. 30 min. Thus, the humidity degradation effects and oxygen contamination of the perovskite layer are excluded in the present study.

Figure 4.9 displays typical 3D graphs of the relative optical density (ΔOD) as a function of wavelength and time for the two systems studied, as well as typical ΔOD versus wavelength plots at various time delays, following photo-excitation at 1026 nm with a pump fluence of 1.5 mJ cm^{-2}. The main ΔOD peak at ~750 nm, while a photo-induced transient absorption (TA) in the range of 600-700 nm is also observed and found to attenuate with time.[26,28] It should be noted here that a linear dependence of ΔOD against pump fluence was observed and depicted in **Figure 4.10**.

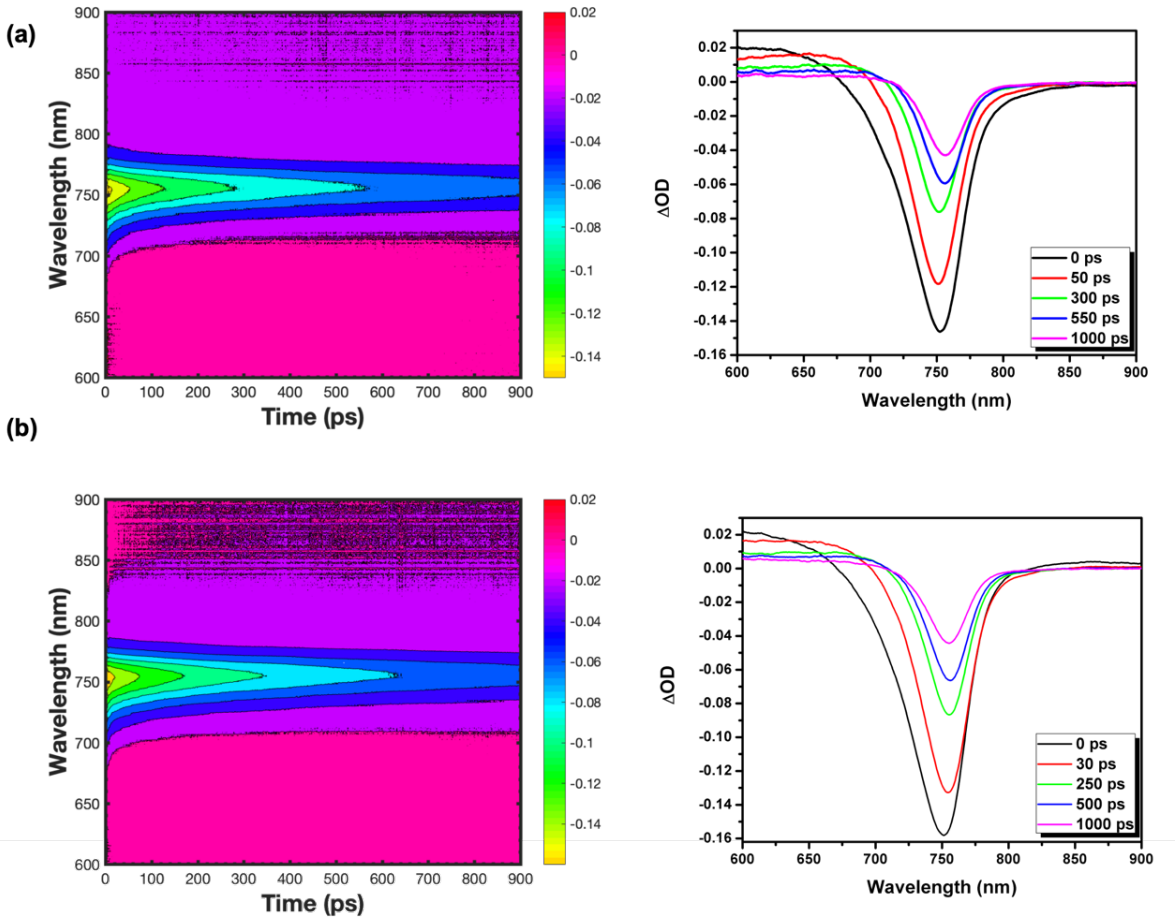

Figure 4.9: Typical transient absorption spectroscopy (TAS) 3D spectra of relative optical density (ΔOD) as a function of wavelength and time of PEDOT:PSS/$CH_3NH_3PbI_3$ (a) and PTAA/$CH_3NH_3PbI_3$ (b) structures, and corresponding ΔOD vs. wavelength plots at various time delays following photoexcitation at 1026 nm with a pump fluence of 1.5 mJ cm^{-2}.

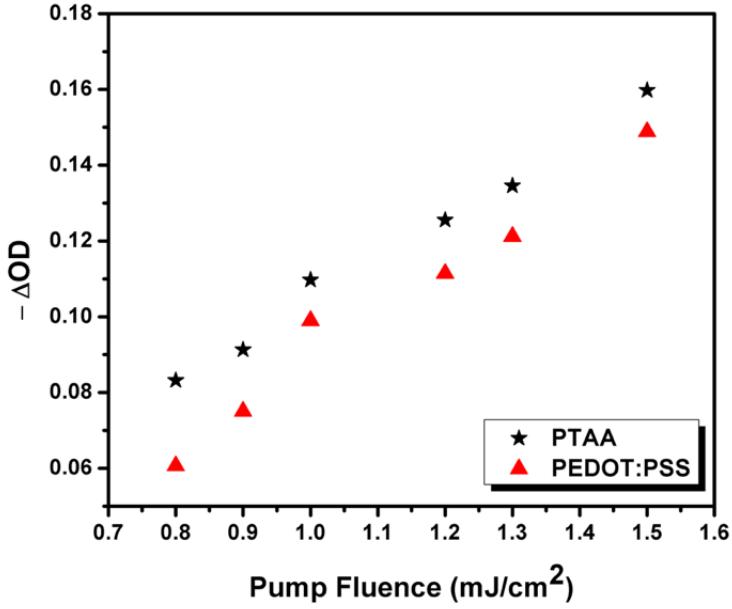

Figure 4.10: Relative optical density (ΔOD) dependence on pump fluence for PEDOT:PSS/$CH_3NH_3PbI_3$ and PTAA/$CH_3NH_3PbI_3$ structures.

The relaxation dynamics of the transient photo-induced bleaching, measured at various excitation fluencies, as well as the corresponding decay kinetics were thoroughly investigated following both exponential and polynomial fitting analysis. The first fitting approach allows us to determine critical time components of the charge carrier transport processes between the perovskite film and the employed hole transport layers,[25,41] i.e. PEDOT:PSS and PTAA, while the higher-order polynomial model provides important kinetic rates for charge carrier recombination processes occurring within the perovskite film. [29,30,37-40] **Figure 4.11** presents three-exponential fittings based on the equation

$$\boldsymbol{y = y_0 + A_1 exp\,(-x/\tau_1) + A_2 exp\,(-x/\tau_2) + A_3 exp\,(-x/\tau_3)} \quad \textbf{(4.1)}$$

for all pump fluences studied. All kinetic fit parameters and the corresponding errors, obtained for the two architectures, are summarized in **Table 4.2**; while the analysis for the error bars is describe in the **Appendix**. In particular, the fast time component (τ_1) is attributed

to charge carrier trapping at perovskite grain boundaries and perovskite/HTL interfaces.[25] This component is observed even at the lowest pump fluence, however, for that fluence τ_1 is too slow and comparable to τ_2; this possibly indicates a difference in the decay kinetics at the lowest fluence, compared to higher fluences (i.e two-versus three-exponential kinetic model respectively). However, regardless the pump fluence employed, i.e. 0.8, 1.3 and 1.5 mJ cm^{-2}, the respective time decay components, τ_1, are found to be significantly faster for the PTAA architecture, i.e. 218, 22 and 10 ps compared to 305, 57 and 43 ps, respectively. This time component represents the time that an excited electron needs to move from the conduction band to the trap states. Thus, smaller τ_1 times suggest quicker traps filling, that leads to larger splitting in the quasi-Fermi energy levels that account plausibly for the observed enhanced V_{oc} of the PTAA devices (**Table 4.1**). In the meantime, free charge carriers are injected more easily to the HTL, leading to enhanced FF and PCE.[42,43] Notably, this time component is not solely affected by the density of trap states, but it also depends on the trap states depth.[44]

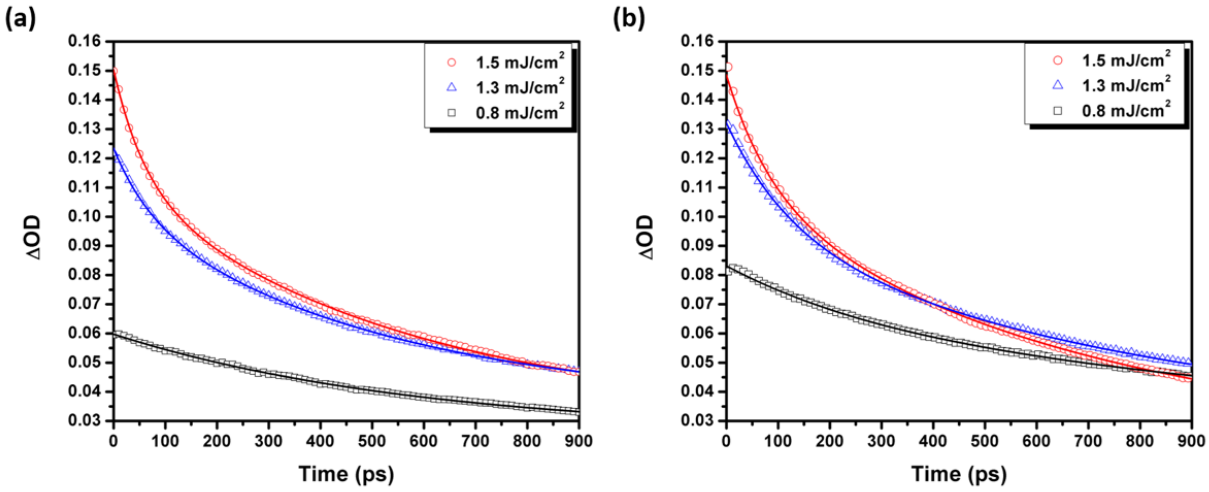

Figure 4.11: Transient band edge bleach kinetics (symbols) and their corresponding decay exponential fits (lines) for PEDOT:PSS/$CH_3NH_3PbI_3$ **(a)** and PTAA/$CH_3NH_3PbI_3$ **(b)** configurations, photoexcited at 1026 nm with various pump fluencies.

Table 4.2: Time components for PEDOT:PSS/$CH_3NH_3PbI_3$ and PTAA/$CH_3NH_3PbI_3$ architectures following exponential fitting (see text).

Fluence	**PEDOT:PSS**				**PTAA**			
(mJ cm^{-2})	**λ_{max} (nm)**	**$\tau_1 \pm 2$ (ps)**	**$\tau_2 \pm 8$ (ps)**	**$\tau_3 \pm$ 0.5x10^7 (ps)**	**λ_{max} (nm)**	**$\tau_1 \pm 2$ (ps)**	**$\tau_2 \pm 8$ (ps)**	**$\tau_3 \pm 13$ (ps)**
0.8	755	305	596	3.9x10^6	755	218	523	3957
1.3	753	57	335	1.5x10^5	751	22	125	790
1.5	753	43	257	1.2x10^5	750	10	101	717

In addition, the second component (τ_2) is assigned to the hole injections from the perovskite into HTL.[25,41] As is the case for τ_1, inspection of data in **Table 4.2** reveals considerably quicker τ_2 decay components also when the PTAA is employed as HTL for all studied fluencies, suggesting faster hole transport dynamics. Indicatively, for the highest pump fluence, τ_2 drops from 257 to 101 ps when PEDOT:PSS is replaced with PTAA. The faster τ_2 decay is in agreement with the obtained PL characteristics, in which significant quenching upon addition of PTAA as the HTL indicates a faster hole extraction. Regarding the electrical performance of the devices in question, the as determined faster hole injection dynamics of the PTAA device, result to better electrical characteristics (**Table 4.1**).[41,45] Nevertheless, as explained earlier, while V_{oc}, FF, and PCE of the PTAA solar cell improve considerably, a comparable J_{sc} is found due to the lower transmittance of the PTAA film compared to the PEDOT:PSS, that appears to compensate the faster hole dynamics, i.e. suppressing the J_{sc} for further improvement. Despite the comparable J_{sc}, the obtained V_{oc}, FF, and PCE of the PTAA device, τ_2 component plays a dominant role on the electrical performance of the device, due to the faster hole injection. Moreover, the revealed τ_2 faster decay component complies well with the higher HOMO level of the PTAA polymer, compared to the PEDOT:PSS, as shown in the corresponding energy level diagram depicted in **Figure 4.7**.[6,7]

Finally, **Table 4.2** lists the third long-life time component (τ_3), which is representative of the exciton recombination time.[25,41] Likewise τ_1 and τ_2 components, τ_3 is also found to be significantly faster for the PTAA architecture at all pump fluences. Remarkably, for the highest employed pump fluence, τ_3 reduces from 120 ns to 717 ps when PTAA is used instead of PEDOT:PSS. In general, the primary recombination processes taking place in perovskite solar cells are as follows. Following photo-excitation, the faster recombination process that occurs, is the exciton recombination with typical lifetime values in the order of 10 ps–10 ns.[53] A slower recombination mechanism is the recombination at the grain boundaries that occurs in the ns time scale.[46,47] This study cannot provide information on the trap-assisted recombination processes (i.e. at grain boundaries and interfaces), since these mechanisms lie out of the delay range employed. This is not the case for the exciton (electron-hole) recombination kinetics, represented by τ_3 in our experiments. The characteristic time components τ_1 and τ_2 are faster in the case of PTAA-based perovskite system compared to the PEDOT:PSS-based one, indicating the superiority of the former. It should be mentioned here though, that the efficient charge transfer from the perovskite to PTAA will benefit the solar cell efficiency, provided also that the back-electron transfer is much slower.[48] Furthermore, we consider that the changes observed in time constants due to the different fluences are the result of more photons per pulse per cm^2 excited. By increasing the pump fluence, the higher initial carrier density results in more efficient exciton formation[49] and the excess energy probably leads to faster exciton dissociation[50]. The result of faster exciton dissociation is the mechanisms that have already mentioned in the manuscript in exponential fitting model to occur faster.

Following this exponential fitting approach, we employ another well-established polynomial fitting model based on the following rate equation:

$$dn(t)/dt = -k_3n^3 - k_2n^2 - k_1n \quad (4.2)$$

where n is the charge carrier density and k_1, k_2 and k_3 the rate constants corresponding respectively to, trap-assisted recombination, bimolecular recombination, and Auger tri-molecular recombination processes (**Figure 4.12**).[29,37-40] On a recent report, Wehrenfennig et al.[29] related the rate of bimolecular recombination (k_2) with the PCE of PSC devices. Namely, it was proposed that slower k_2 rates, are indicative of larger free charge carriers diffusion lengths that favor the performance of planar-heterojunction devices. **Table 4.3** presents the kinetic rate constants as determined for the two architectures in question. Inspection of **Table 4.3**, reveals that for all studied pump fluencies, the PTAA polymer architecture exhibits slower k_2 rates when compared to the corresponding of PEDOT:PSS. Such findings provide additional explanation for the enhanced photovoltaic performance (**Table 4.1**) of the former device.

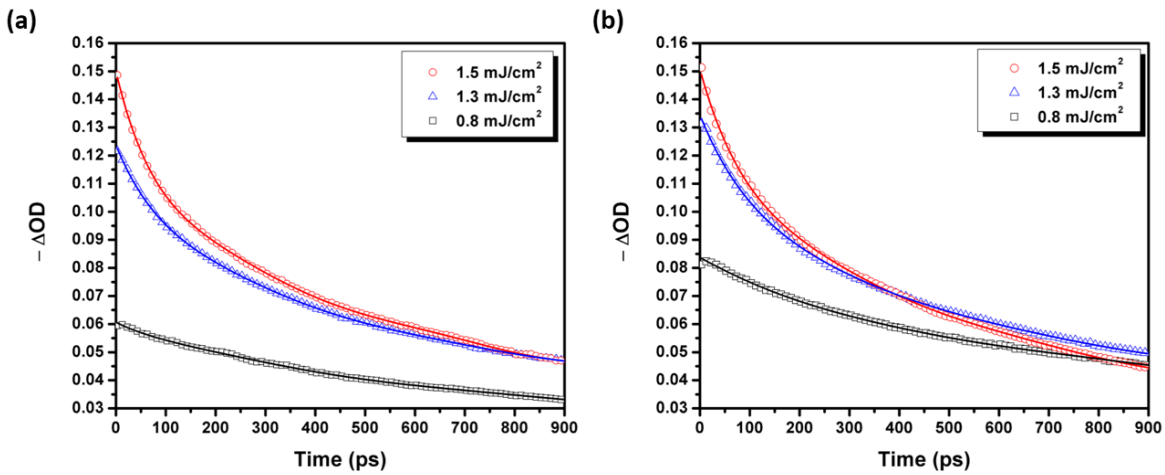

Figure 4.12: Transient band edge bleach kinetics (symbols) and their corresponding decay polynomial fits (lines) for PEDOT:PSS/$CH_3NH_3PbI_3$ **(a)** and PTAA/$CH_3NH_3PbI_3$ **(b)** configurations, photoexcited at 1026 nm with various pump fluencies.

Table 4.3: Charge carrier recombination rate constants for PEDOT:PSS/$CH_3NH_3PbI_3$ and PTAA/$CH_3NH_3PbI_3$ architectures following polynomial rate equation fitting (see text).

Fluence	PEDOT:PSS			PTAA		
(mJ cm^{-2})	k_3±0.4x10^{-14} (cm^{6}s^{-1})	k_2±0.2x10^{-12} (cm^{3}s^{-1})	k_1±0.1x10^{-7} (μs^{-1})	k_3±0.4 x10^{-14} (cm^{6}s^{-1})	k_2±0.2x10^{-13} (cm^{3}s^{-1})	k_1±0.1x10^{-7} (μs^{-1})
0.8	-	3.3x10^{-12}	3.8x10^{-7}	-	4x10^{-13}	1.5x10^{-7}
1.3	3.0x10^{-14}	1.8x10^{-11}	2.1x10^{-6}	1.8x10^{-14}	0.9x10^{-11}	1.8x10^{-6}
1.5	7.3x10^{-14}	3.6x10^{-11}	4.4x10^{-6}	3.8x10^{-14}	1.7x10^{-11}	3.1x10^{-6}

In summary, the exponential fitting approach depicted faster hole injection for the PTAA/perovskite architecture, while the higher order polynomial fitting model revealed slower kinetic rates for the charge carrier recombination processes within the perovskite. Both findings are in agreement and account plausibly for the advanced performance of the PTAA polymer solar cell device.

4.3 Conclusions

In conclusion, the introduction of PTAA enhances considerably the performance of the photovoltaic devices. Analysis of TAS data revealed considerably quicker dynamics and slower bimolecular recombination rates when PTAA polymer is used, that account plausibly for the improved PCEs of the devices in which it was incorporated. Furthermore, experiments clarified that the PCE enhancement is mostly attributed to the reduced roughness of the HTL surface, while a small fraction can be ascribed to HTL wettability. Findings of the present work pave the way towards a better understanding of how the surface roughness and wettability of the HTL polymer affects the device performance, while ongoing work focuses on discovering ways for further improvement of the stability and performance of PSCs with HTL materials of reduced hydrophilicity and smoother surfaces.

References:

1. Leguy, A. M.; Hu, Y.; Campoy-Quiles, M.; Alonso, M. I.; Weber, O. J.; Azarhoosh, P.; van Schilfgaarde, M.; Weller, M.T.; Bein, T.; Nelson, J.; Docampo, P.; Barnes, P. R. F. Reversible Hydration of $CH_3NH_3PbI_3$ in Films, Single Crystals, and Solar Cells. *Chem. Mater.* **2015**, *27*, 3397-3407.
2. Docampo, P.; Bein, T. A Long-Term View on Perovskite Optoelectronics. *Acc. Chem. Res.* **2016**, *49*, 339-346.
3. Docampo, P.; Ball, J. M.; Darwich, M.; Eperon, G. E.; Snaith, H. J. Efficient Organometal Trihalide Perovskite Planar-Heterojunction Solar Cells on Flexible Polymer Substrates. *Nat. Commun.* **2013**, *4*, 2761.
4. Zhao, C.; Chen, B.; Qiao, X.; Luan, L.; Lu, K.; Hu, B. Revealing Underlying Processes Involved in Light Soaking Effects and Hysteresis Phenomena in Perovskite Solar Cells. *Adv. Energy Mater.* **2015**, *5*, 1500279.
5. Snaith, H. J. Perovskites: The Emergence of a New Era for Low-Cost, High-Efficiency Solar Cells. *J. Phys. Chem. Lett.* **2013**, *4*, 3623-3630.
6. Gao, P.; Grätzel, M.; Nazeeruddin, M. K. Organohalide Lead Perovskites for Photovoltaic Applications. *Energy Environ. Sci.* **2014**, *7*, 2448-2463.
7. NREL Best Research-Cell Photovoltaic Efficiency Chart.
8. Zhao, Y.; Zhu, K. CH_3NH_3Cl-assisted One-Step Solution Growth of $CH_3NH_3PbI_3$: Structure, Charge-Carrier Dynamics, and Photovoltaic Properties of Perovskite Solar Cells. *J. Phys. Chem. C* **2014**, *118*, 9412-9418.
9. Pathak, S.; Sepe, A.; Sadhanala, A.; Deschler, F.; Haghighirad, A.; Sakai, N.; Goedel, K. C.; Stranks, S. D.; Noel, N.; Price, M.; Huttner, S.; Hawkins, N. A.; Friend, R. H.; Steiner, U.; Snaith, H. J. Atmospheric Influence upon Crystallization and Electronic Disorder and Its Impact on the Photophysical Properties of Organic–Inorganic Perovskite Solar Cells. *ACS Nano* **2015**, *9*, 2311-2320.
10. Bi, D.; Tress, W.; Dar, M. I.; Gao, P.; Luo, J.; Renevier, C.; Schenk, K.; Abate, A.; Giordano, F.; Baena, J. B. C.; Decoppet, J. D; Zakeeruddin, S. M.; Nazeeruddin, M. K.; Grätzel, M.; Hagfeldt, A. Efficient Luminescent Solar Cells Based on Tailored Mixed-Cation Perovskites. *Sci. Adv.* **2016**, *2*, e1501170.
11. Li, F.; Zhu, W.; Bao, C.; Yu, T.; Wang, Y.; Zhou, X.; Zou, Z. Laser-Assisted Crystallization of $CH_3NH_3PbI_3$ Films for Efficient Perovskite Solar Cells with a High Open-Circuit Voltage. *Chem. Commun.* **2016**, *52*, 5394-5397.
12. Jeon, T.; Jin, H. M.; Lee, S. H.; Lee, J. M.; Park, H. I.; Kim, M. K.; Lee, J. K.; Shin, B.; Kim, S. O. Laser Crystallization of Organic–Inorganic Hybrid Perovskite Solar Cells. *ACS Nano* **2016**, *10*, 7907-7914.
13. Kojima, A.; Teshima, K.; Shirai, Y.; Miyasaka, T. Organometal Halide Perovskites as Visible-Light Sensitizers for Photovoltaic Cells. *J. Am. Chem. Soc.* **2009**, *131*, 6050-6051.
14. Burschka, J.; Pellet, N.; Moon, S. J.; Humphry-Baker, R.; Gao, P.; Nazeeruddin, M. K.; Grätzel, M. Sequential Deposition as a Route to High-Performance Perovskite-Sensitized Solar Cells. *Nature* **2013**, *499*, 316-319.

15. Somsongkul, V.; Lang, F.; Jeong, A. R.; Rusu, M.; Arunchaiya, M.; Dittrich, T. Hole Blocking $PbI_2/CH_3NH_3PbI_3$ Interface. *Phys. Status Solidi RRL*. **2014**, *8*, 763-766.
16. Xing, G.; Mathews, N.; Lim, S. S., Yantara, N.; Liu, X.; Sabba, D.; Grätzel, M.; Mhaisalkar, S.; Sum, T. C. Low-Temperature Solution-Processed Wavelength-Tuneable Perovskites for Lasing. *Nat. Mater*. **2014**, *13*, 476−480.
17. Tan, Z. K.; Moghaddam, R.S.; Lai, M.L.; Docampo, P.; Higler, R.; Deschler, F.; Price, M.; Sadhanala, A.; Pazos, L. M.; Credgington, D.; Hanusch, F.; Bein, T.; Snaith, H. J.; Friend, R. H. Bright Light-Emitting Diodes Based on Organometal Halide Perovskite. *Nat. Nanotechnol.* **2014**, *9*, 687−692.
18. Liu, M.; Johnston, M. B.; Snaith, H. J. Efficient Planar Heterojunction Perovskite Solar Cells by Vapour Deposition. *Nature* **2013**, *501*, 395-398.
19. Chen, Q.; Zhou, H.; Hong, Z.; Luo, S.; Duan, H. S.; Wang, H. H.; Liu, Y.; Li, G.; Yang, Y. Planar Heterojunction Perovskite Solar Cells via Vapor-Assisted Solution Process. *J. Am. Chem. Soc.* **2013**, *136*, 622-625.
20. Xiao, Z.; Dong, Q.; Bi, C.; Shao, Y.; Yuan, Y.; Huang, J. Solvent Annealing of Perovskite-Induced Crystal Growth for Photovoltaic-Device Efficiency Enhancement. *Adv. Mater*. **2014**, *26*, 6503-6509.
21. Nie, W.; Blancon, J. C.; Neukirch, A. J.; Appavoo, K.; Tsai, H.; Chhowalla, M.; Alam, M. A; Sfeir, M. Y.; Katan, C.; Even, J.; Tretiak, S.; Crochet, J. J.; Gupta, G.; Mohite, A. D. Light-Activated Photocurrent Degradation and Self-Healing in Perovskite Solar Cells. *Nature Commun.* **2016**, *7*, 11574.
22. Domanski, K.; Roose, B.; Matsui, T.; Saliba, M.; Turren-Cruz, S. H.; Correa-Baena, J. P.; Carmona, C. R.; Richardson, G.; Jamie, M.; Foster, J.M.; De Angelis, F.; Ball, J. M.; Petrozza, A.; Mine, N.; Nazeeruddin, M. K.; Tress, W.; Grätzel, M.; Steiner, U.; Hagfeldt, A.; Abate, A. Migration of Cations Induces Reversible Performance Losses over Day/Night Cycling in Perovskite Solar Cells. *Energy Environ. Sci.* **2017**, *10*, 604-613.
23. Wang, Q.; Bi, C.; Huang, J. Doped Hole Transport layer for Efficiency Enhancement in Planar Heterojunction Organolead Trihalide Perovskite Solar Cells. *Nano Energy* **2015**, *15*, 275-280.
24. Kakavelakis, G.; Maksudov, T.; Konios, D.; Paradisanos, I.; Kioseoglou, G.; Stratakis, E.; Kymakis, E. Efficient and Highly Air Stable Planar Inverted Perovskite Solar Cells with Reduced Graphene Oxide Doped PCBM Electron Transporting Layer. *Adv. Energy Mater.* **2016**, *7*, 1602120.
25. Wang, L.; McCleese, C.; Kovalsky, A.; Zhao, Y.; Burda, C. Femtosecond Time-Resolved Transient Absorption Spectroscopy of $CH_3NH_3PbI_3$ Perovskite Films: Evidence for Passivation Effect of PbI_2. *J. Am. Chem. Soc.* **2014**, *136*, 12205-12208.
26. Heo, J. H.; Han, H. J.; Kim, D.; Ahn, T. K.; Im, S. H. Hysteresis-Less Inverted $CH_3NH_3PbI_3$ Planar Perovskite Hybrid Solar Cells with 18.1% Power Conversion Efficiency. *Energy Environ. Sci.* **2015**, *8*, 1602-1608.
27. Bi, C.; Wang, Q.; Shao, Y.; Yuan, Y.; Xiao, Z.; Huang, J. Non-Wetting Surface-Driven High-Aspect-Ratio Crystalline Grain Growth for Efficient Hybrid Perovskite Solar Cells. *Nat. Commun.* **2015**, *6*, 7747.

28. Stranks, S. D.; Eperon, G. E.; Grancini, G.; Menelaou, C.; Alcocer, M. J.; Leijtens, T.; Herz, L. M.; Petrozza, A.; Snaith, H. J. Electron-Hole Diffusion Lengths Exceeding 1 micrometer in an Organometal Trihalide Perovskite Absorber. *Science* **2013**, *342*, 341-344.
29. Wehrenfennig, C.; Eperon, G. E.; Johnston, M. B.; Snaith, H. J.; Herz, L. M. High Charge Carrier Mobilities and Lifetimes in Organolead Trihalide Perovskites. *Adv. Mater.* **2014**, *26*, 1584-1589.
30. Piatkowski, P.; Cohen, B.; Ramos, F. J.; Di Nunzio, M.; Nazeeruddin, M. K.; Grätzel, M.; Ahmad, S.; Douhal, A. Direct Monitoring of Ultrafast Electron and Hole Dynamics in Perovskite Solar Cells. *Phys. Chem. Chem. Phys.* **2015**, *17*, 14674-14684.
31. Ishioka, K.; Barker, B. G.; Yanagida, M.; Shirai, Y.; Miyano, K. Direct Observation of Ultrafast Hole Injection from Lead Halide Perovskite by Differential Transient Transmission Spectroscopy. *J. Phys. Chem. Lett.* **2017**, *8*, 3902-3907.
32. Corani, A.; Li, M. H.; Shen, P. S.; Chen, P.; Guo, T. F.; El Nahhas, A.; Zheng, K.; Yartsev, A.; Sundstrom, V.; Ponseca Jr, C. S. Ultrafast Dynamics of Hole Injection and Recombination in Organometal Halide Perovskite Using Nickel Oxide as p-Type Contact Electrode. *J. Phys. Chem. Lett.* **2016**, *7*, 1096-1101.
33. Song, T. B.; Chen, Q.; Zhou, H.; Jiang, C.; Wang, H. H.; Yang, Y. M.; Yang, Y. Perovskite Solar Cells: Film Formation and Properties. *J. Mater. Chem. A* **2015**, *3*, 9032-9050.
34. Huang, J. H.; Jiang, K. J.; Cui, X. P.; Zhang, Q. Q.; Gao, M.; Su, M. J.; Song, Y. Direct Conversion of $CH_3NH_3PbI_3$ from Electrodeposited PbO for Highly Efficient Planar Perovskite Solar Cells. *Sci. Rep.* **2015**, *5*, 15889.
35. McEvoy, A., Markvart, T., Castañer, L. *Practical Handbook of Photovoltaics: Fundamentals and Applications.* Elsevier, **2003**.
36. McEvoy, A. J., Castaner, L., Markvart, T. *Solar cells: Materials, Manufacture and Operation.* Academic Press, **2012**.
37. Stranks, S. D.; Burlakov, V. M.; Leijtens, T.; Ball, J. M.; Goriely, A.; Snaith, H. J. Recombination Kinetics in Organic-Inorganic Perovskites: Excitons, Free Charge, and Subgap States. *Phys. Rev. Appl.* **2014**, *2*, 034007.
38. Manser, J. S.; Kamat, P. V. Band Filling with Free Charge Carriers in Organometal Halide Perovskites. *Nat. Photonics* **2014**, *8*, 737-743.
39. La-o-vorakiat, C.; Salim, T.; Kadro, J.; Khuc, M. T.; Haselsberger, R.; Cheng, L.; Xia, H.; Gurzadyan, G. G.; Su, H.; Lam, Y. M.; Marcus, R. A.; Michel-Beyerle, M. E.; Chia, E. E. M. Elucidating the Role of Disorder and Free-Carrier Recombination Kinetics in $CH_3NH_3PbI_3$ Perovskite Films. *Nat. Commun.* **2015**, *7*, 7903.
40. Klein, J. R.; Flender, O.; Scholz, M.; Oum, K.; Lenzer, T. Charge Carrier Dynamics of Methylammonium Lead Iodide: from PbI_2-rich to Low-Dimensional Broadly Emitting Perovskites. *Phys. Chem. Chem. Phys.* **2016**, *18*, 10800-10808.
41. Zhu, Z.; Ma, J.; Wang, Z.; Mu, C.; Fan, Z.; Du, L.; Yang B.; Fan L.; Yan H.; Phillips D. L.; Yang, S. Efficiency Enhancement of Perovskite Solar Cells Through Fast Electron Extraction: The Role of Graphene Quantum Dots. *J. Am. Chem. Soc.* **2014**, *136*, 3760-3763.

42. Shao, S.; Abdu-Aguye, M.; Sherkar, T. S.; Fang, H. H.; Adjokatse, S.; Brink, G. T.; Kooi, B. J.; Koster, L. J. A.; Loi, M. A. The Effect of the Microstructure on Trap-Assisted Recombination and Light Soaking Phenomenon in Hybrid Perovskite Solar Cells. *Adv. Funct. Mater.* **2016**, *26*, 8094-8102.
43. Leijtens, T.; Stranks, S. D.; Eperon, G. E.; Lindblad, R.; Johansson, E. M.; McPherson, I. J.; Rensmo, H.; Ball, J. M.; Lee, M. M.; Snaith, H. J. Electronic Properties of Meso-Superstructured and Planar Organometal Halide Perovskite Films: Charge Trapping, Photodoping, and Carrier Mobility. *ACS Nano* **2014**, *8*, 7147-7155.
44. Leijtens, T.; Eperon, G. E.; Barker, A. J.; Grancini, G.; Zhang, W.; Ball, J. M.; Kandada, A. R. S.; Snaith H. J.; Petrozza, A. Carrier Trapping and Recombination: The Role of Defect Physics in Enhancing the Open Circuit Voltage of Metal Halide Perovskite Solar Cells. *Energy Environ. Sci.* **2016**, *9*, 3472-3481.
45. Tao, C.; Neutzner, S.; Colella, L.; Marras, S.; Kandada, A. R. S.; Gandini, M.; De Bastiani M.; Pace G.; Manna L.; Caironi, M.; Bertarelli, C.; Petrozza, A. 17.6% Stabilized Efficiency in Low-Temperature Processed Planar Perovskite Solar Cells. *Energy Environ. Sci.* **2015**, *8*, 2365-2370.
46. Bernardi, M.; Grossman, J. C. Computer Calculations Across Time and Length Scales in Photovoltaic Solar Cells *Energy Environ. Sci.* **2016**, *9*, 2197-2218.
47. Metzger, W. K. How Lifetime Fluctuations, Grain-Boundary Recombination, and Junctions Affect Lifetime Measurements and their Correlation to Silicon Solar Cell Performance. *Sol. Energy Mater. Sol. Cells* **2008**, *92*, 1123-1135.
48. Marchioro, A.; Teuscher, J.; Friedrich, D.; Kunst, M.; Van De Krol, R.; Moehl, T.; Grätzel, M.; Moser, J. E. Unravelling the Mechanism of Photoinduced Charge Transfer Processes in Lead Iodide Perovskite Solar Cells. *Nat. Photonics.* **2014**, *8*, 250-255.
49. Piatkowski, P.; Cohen, B.; Kazim, S.; Ahmad, S.; Douhal, A. How Photon Pump Fluence Changes the Charge Carrier Relaxation Mechanism in an Organic–Inorganic Hybrid Lead Triiodide Perovskite. *Phys. Chem. Chem. Phys.* **2016**, *18*, 27090-27101
50. Piatkowski, P.; Cohen, B.; Ponseca Jr, C. S.; Salado, M.; Kazim, S.; Ahmad, S.; Sundstrom, V.; Douhal, A. Unravelling Charge Carriers Generation, Diffusion, and Recombination in Formamidinium Lead Triiodide Perovskite Polycrystalline Thin Film. *J. Phys. Chem. Lett.* **2016**, *7*, 204-210.

Chapter 5

In-Situ Monitoring of the Charge Carrier Dynamics of $CH_3NH_3PbI_3$ Perovskite Crystallization Process

In this Chapter, the TAS measurements were performed in-situ during the crystallization process of the perovskite layer, in order to study the unexplored area of the charge carrier dynamics behavior directly during the formation of the perovskite layer (**Figure 5.1**).

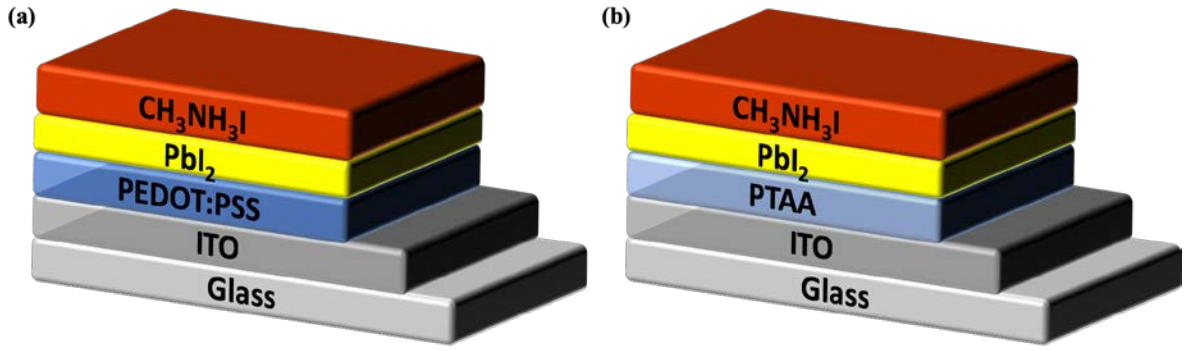

Figure 5.1: Schematic illustration of the two configurations **(a)** PEDOT:PSS/precursors and **(b)** PTAA/precursors that used for the in-situ study.

In particular, $CH_3NH_3PbI_3$ films were deposited on two types of polymeric hole transport layers (HTL), poly(3,4-ethylenedioxythiophene)-poly-(styrenesulfonate) (PEDOT:PSS) and poly-(triarylamine) (PTAA), that are known to provide different carrier transport characteristics in perovskite solar cells. In order to monitor the evolution of the perovskite charge carrier dynamics during the crystallization process, the so-formed $CH_3NH_3PbI_3$/HTL architectures were studied in-situ by TAS at three different annealing temperatures, i.e. 90, 100 and 110 ^{o}C. It is revealed that the annealing time period required in order to achieve the optimum perovskite film quality in terms of the decay dynamics strongly depends on the

annealing temperature, as well as, on the employed HTL. It is important to know exactly the required annealing period for the formation of the perovskite layer upon different HTL polymers, in order to reduce the time and energy for the fabrication of the devices, as well to diminish the materials that we use, since up to know we needed the whole device to conclude for the best perovskite layer. For both HTLs, the required period decreases as higher annealing temperature is used, while, for the more hydrophobic PTAA polymer, longer annealing periods were required in order to obtain the optimum charge carrier dynamics. The correlation of the TAS finding with the structural and morphological features of the perovskite films is analysed and provides useful insights on the charge extraction dynamics and recombination processes in perovskite optoelectronic devices.

5.1 Introduction

Although the perovskites play a crucial role in the photovoltaic research due to their unique optical and electronic properties, there is still significant lack of understanding of the charge extraction processes as well as the recombination dynamics which significantly limit the efficiency attained, compared to the theoretical predictions.[1-4] Especially, the evolution of the charge carrier dynamics upon different HTL polymers, are never studied in order to have clear evidence that the optimum perovskite layer for more efficient device, exhibits the faster charge carrier transport and slower recombination processes.

Herein, the perovskite charge carrier dynamics are monitored in-situ, during the crystallization process by means of transient absorption spectroscopy (TAS). Such approach allows us to identify the optimum annealing period for each configuration (PEDOT:PSS and PTAA/$CH_3NH_3PbI_3$), based on the revealed faster time components and slower recombination rates, i.e. critical parameters for the overall electrical performance of the

device. On the contrary, in a typical manner, the optimum annealing period for the crystallization process is determined empirically upon XRD patterns or only after completing the photovoltaic device fabrication by measuring the efficiency of the device, i.e. without taking into account the charge extraction properties between the perovskite/HTL interlayer. Namely, the charge extraction properties were investigated at three different thermal annealing temperatures applied during the TAS measurement, i.e. 90 ^{o}C, 100 ^{o}C and 110 ^{o}C (**Table 5.1**), while employing two different HTL polymers, i.e. the more hydrophilic, PEDOT:PSS, and the more hydrophobic, PTAA. All TAS measurements were performed entirely under inert conditions within a specially designed homemade cell to exclude any ambient-induced degradation effects. It is well known that the charge carrier dynamics and recombination rates, probed by TAS, are strongly correlated with the electrical performance of PSC devices[1,5-9] and also, the nature of the employed HTL polymer affects the charge extraction processes and thus the photovoltaic efficiency.[1,5,7,8,10-21]

Particularly, we observe that in case of PTAA/$CH_3NH_3PbI_3$ architectures, the charge carrier extraction and injection processes are significantly faster compared to the corresponding time components of the PEDOT:PSS/$CH_3NH_3PbI_3$ system, i.e. regardless the selected crystallization temperatures. Moreover, we found that the annealing time period required to achieve optimum perovskite film quality, in terms of the decay dynamics, strongly depends on the crystallization temperature, as well as, on the HTL. For both HTLs, the required annealing time period decreases as a higher annealing temperature is used, whereas strikingly, for the more hydrophobic PTAA polymer, longer annealing periods are required in order to reach the optimum charge carrier dynamics. The TAS findings are correlated with the structural and morphological characteristics of the so-formed perovskite films, investigated by x-ray diffraction (XRD), scanning electron microscopy (SEM) and absorption

spectroscopy. As a consequence, insights on carrier transport properties and extraction dynamics are acquired, which are useful towards the fabrication of high-quality perovskite layers for optoelectronic devices.

Table 5.1: HTL/$CH_3NH_3PbI_3$ Sample Configurations and Corresponding Synthesis Parameters.

Samples	HTL polymers	Crystallization parameters	Annealing Temperature
1	PEDOT:PSS	Thermal Annealing	100 ^oC
2	PEDOT:PSS	In-situ TAS Annealing	90 ^oC
3	PEDOT:PSS	In-situ TAS Annealing	100 ^oC
4	PEDOT:PSS	In-situ TAS Annealing	110 oC
5	PTAA	Thermal Annealing	100 ^oC
6	PTAA	In-situ TAS Annealing	90 ^oC
7	PTAA	In-situ TAS Annealing	100 ^oC
8	PTAA	In-situ TAS Annealing	110 ^oC

5.2 Results and Discussion

5.2.1 Structural and Morphological characterization

It is well known that the PCE of the PSCs is strongly correlated with the crystalline properties of the perovskite absorber and is notably affected by the grain boundaries, grain size and the perovskite phase.[22] **Figure 5.2** presents the XRD patterns for the different IS perovskite layers deposited onto the two HTLs used here. All patterns are dominated by two main peaks at 14° and 28.4°, corresponding to the (110) and (220) lattice planes of $CH_3NH_3PbI_3$, respectively.[12,22-25] The much weaker peak at 31.8° is attributed to the (310) lattice plane, while the (220) crystal reflection that is expected at 24.4° is not observed. Also, the peak at 12.5°, corresponding to an excess PbI_2, is present in all XRD graphs. Some studies have already shown that the residual or unreacted PbI_2 can decrease the surface states and defects in the perovskite layer.[26-28] Furthermore, the slightly over-stoichiometric PbI_2 can

enhance the electrical characteristics and the electric quality of the PSCs through the passivation effect.[13,28,29] It can be concluded that all XRD profiles of the perovskite layers formed on the two HTLs used, exhibit the same peaks, however as the thermal annealing temperature rises the intensity of PbI_2 peak marginally increases, while the intensity of the peak corresponding to (110) lattice plane at 14° slightly decreases for PEDOT:PSS/$CH_3NH_3PbI_3$ configuration, while increases for PTAA/$CH_3NH_3PbI_3$ architecture. It is also noted that, regardless the temperature, the IS samples of the PEDOT:PSS/$CH_3NH_3PbI_3$ system present weaker PbI_2 peaks compared to the corresponding TA ones (**Figure 5.2**),[5] while the PTAA/$CH_3NH_3PbI_3$ IS samples always show a stronger PbI_2 peak (**Figure 5.2**).[5] The $CH_3NH_3PbI_3/PbI_2$ peak ratios for all IS samples are summarized in **Table 5.2** and it is clear that the highest ratio for PEDOT:PSS/$CH_3NH_3PbI_3$ configuration is 2.83 and is observed at 90 ^oC, while for PTAA/ $CH_3NH_3PbI_3$ architecture is 1.63 and is observed at 110 ^oC.

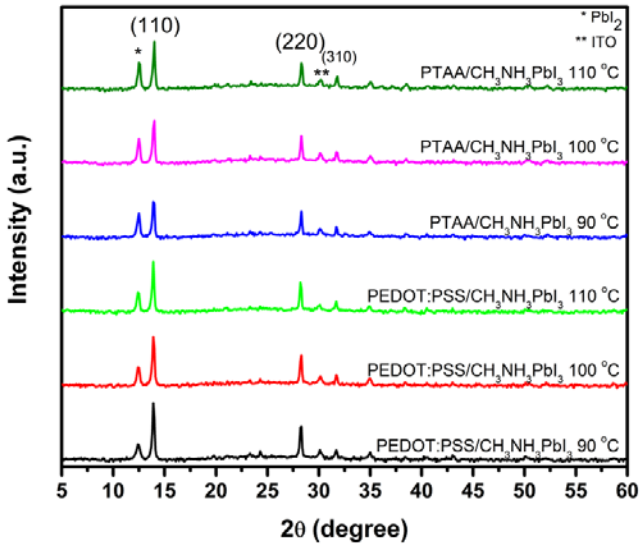

Figure 5.2: XRD patterns of the PEDOT:PSS/$CH_3NH_3PbI_3$ and PTAA/$CH_3NH_3PbI_3$ architectures at all studied temperatures.

Table 5.2: $CH_3NH_3PbI_3/PbI_2$ peak ratios from XRD patterns for all IS studied samples.

Architecture	Annealing Temperature	$CH_3NH_3PbI_3/PbI_2$ Peak Ratio
PEDOT:PSS/ $CH_3NH_3PbI_3$	90 ^oC	2.83
PEDOT:PSS/ $CH_3NH_3PbI_3$	100 ^oC	2.21
PEDOT:PSS/ $CH_3NH_3PbI_3$	110 ^oC	2.20
PTAA/ $CH_3NH_3PbI_3$	90 ^oC	1.37
PTAA/ $CH_3NH_3PbI_3$	100 ^oC	1.58
PTAA/ $CH_3NH_3PbI_3$	110 ^oC	1.63

In order to explore the morphological differences of the various perovskite layers prepared, SEM imaging presented in **Figure 5.3**, was employed. In particular, **Figure 5.3(a,e)** show the SEM images of the TA perovskite layers grown onto the PEDOT:PSS and PTAA, respectively, whereas **Figure 5.3(b-d)** and **Figure 5.3(f-h)** illustrate the SEM images for the IS samples at all studied temperatures. It should be mentioned that the SEM images for IS samples, were captured following the annealing time period that the optimum decay time components were observed, as it will be described below.

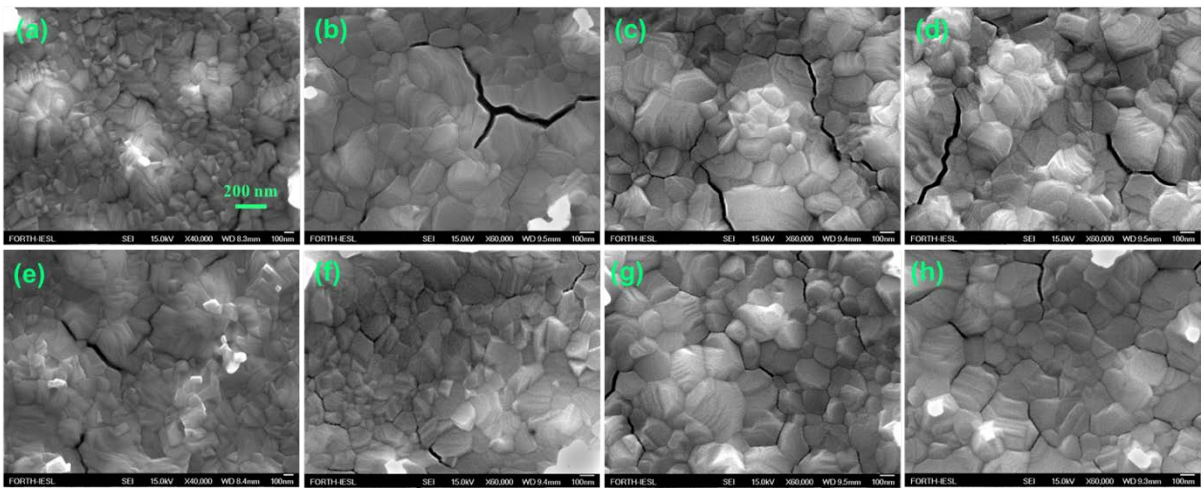

Figure 5.3: SEM images for the PEDOT:PSS/$CH_3NH_3PbI_3$ configuration thermal annealing (a) at 90 ^oC (b), 100 ^oC (c), 110 ^oC (d) and for PTAA/$CH_3NH_3PbI_3$ architecture thermal annealing (e) at 90 ^oC (f), 100 ^oC (g) and 110 ^oC (h), respectively.

In agreement to previous findings,[5,11] inspection of **Figure 5.3(a)** and **Figure 5.3(e)** shows that, in the case of TA samples, a larger perovskite grain size is obtained for the PTAA architectures. However, when one considers the IS samples, the perovskite grain size in case of PEDOT:PSS polymer is larger than the one grown on PTAA. Moreover, in the case of PEDOT:PSS/$CH_3NH_3PbI_3$ system, the perovskite grain size for the TA sample (**Figure 5.3(a)**) is always smaller when compared to that of IS samples, regardless the annealing temperature; in particular, larger grains are obtained at 90 ^oC. Rather differently, in the case of PTAA/$CH_3NH_3PbI_3$ IS samples the perovskite grains are larger for the two higher in-situ annealing temperatures i.e. 100 ^oC and 110 ^oC, compared to the grain size of the TA sample. This can be attributed to the slightly different thermal crystallization history among the TA and the IS samples employed for the in-situ TAS studies.

The corresponding AFM images of the PEDOT:PSS and PTAA polymer surfaces are shown in **Figure 5.4(a,b)**. The average roughness values estimated from these images are equal to 0.942 and 0.451 nm for the PEDOT:PSS and PTAA, respectively. Furthermore, in **Figure 5.4(c,d)** one can see that the absorbance spectra exhibit the two distinct features at 490 nm and 760 nm attributed to optical transitions within the dual valence band structure of $CH_3NH_3PbI_3$.[7,8,10,12,14] For all studied IS samples as well as for the TA samples for each employed HTL polymer, there is no noticeable shift for the two characteristics absorption features (**Figure 5.4c,d**). Notably, in the case of more hydrophilic PEDOT:PSS the absorption intensity of both TA and IS sample is approximately equal, while when the more hydrophobic PTAA polymer is employed, the intensity for TA sample is significantly higher

compared with the corresponding IS samples. This is additional evidence, that the in-situ crystallization is not favored upon using the more hydrophobic PTAA polymer.

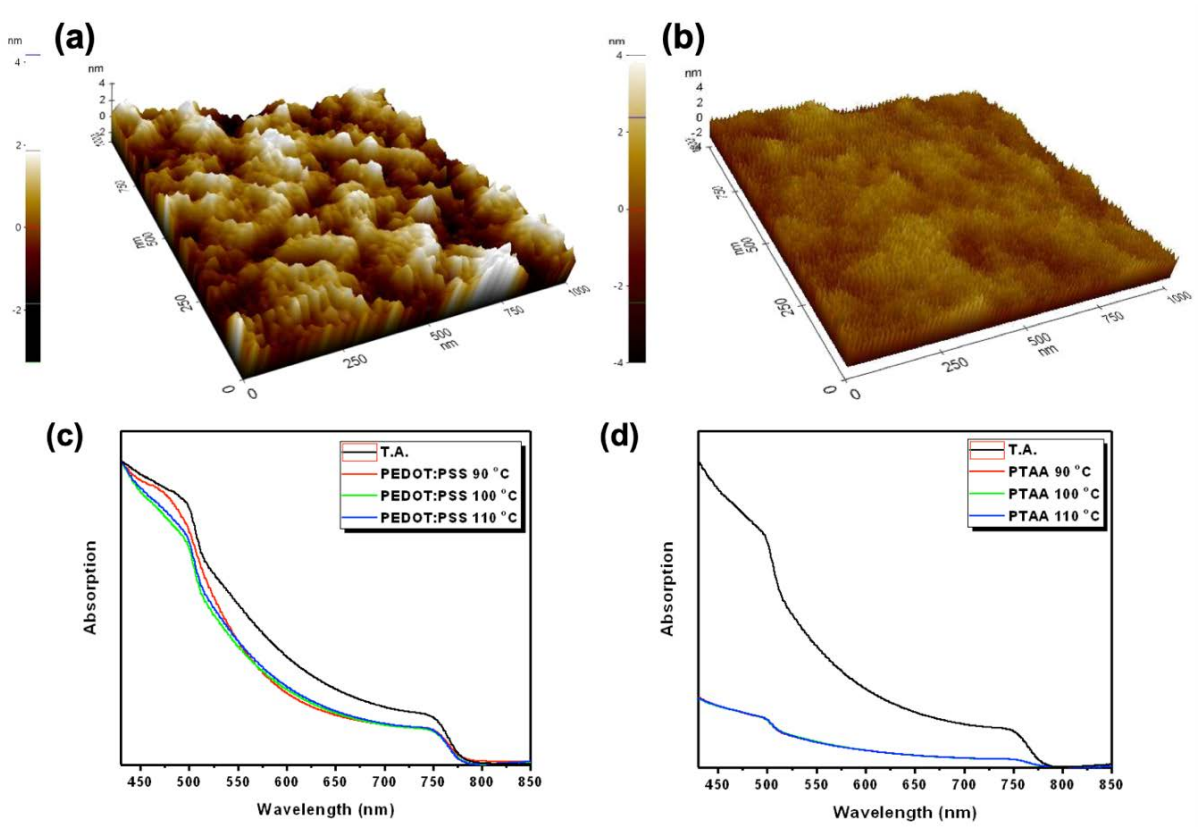

Figure 5.4: AFM measurements of the PEDOT:PSS (a) and PTAA (b) polymers. Absorption spectra for PEDOT:PSS/$CH_3NH_3PbI_3$ (c) and PTAA/$CH_3NH_3PbI_3$ (d) configurations for TA and IS samples.

5.2.2 TAS studies

Understanding the carrier transport properties at the HTL/perovskite interfaces is considerably important towards the enhancement of the performance of PSCs. It is well known that TAS is a powerful tool in order to extract information regarding charge carrier dynamics and recombination processes.[1,5-11,13-21] In order to shed light on the crystallization process of both PEDOT:PSS/$CH_3NH_3PbI_3$ and PTAA/$CH_3NH_3PbI_3$ configurations, we performed in-situ TAS measurement at three different annealing temperatures, i.e. 90, 100 and 110 ^{o}C. It is necessary to mention that the TAS measurements for the reference TA

samples were performed at room temperature, while in-situ measurements in the IS samples were obtained at the aforementioned three temperatures following crystallization (**Table 5.1**).

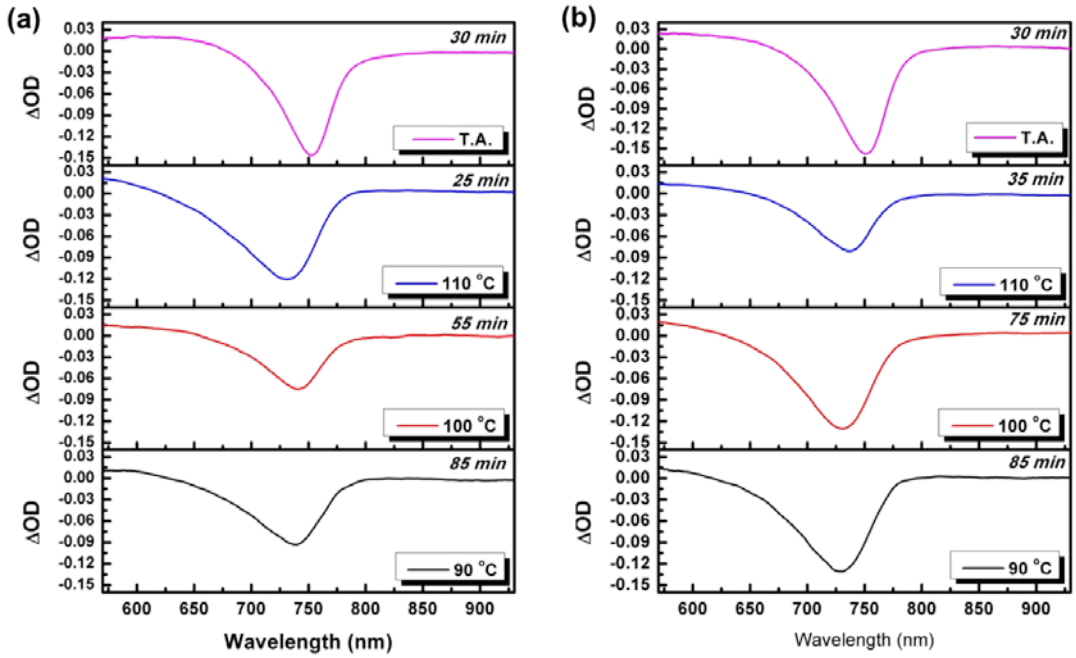

Figure 5.5: Typical TAS spectra of ΔOD as a function of wavelength at t=0 ps, for 90, 100 and 110 ^{o}C and Reference (Thermal Annealing at 100 ^{o}C on hot plate – TA) for Glass/ITO/PEDOT:PSS/$CH_3NH_3PbI_3$ (a) and for Glass/ITO/PTAA/$CH_3NH_3PbI_3$ (b) configurations following photoexcitation at 1026 nm with a pump fluence of 1.5 mJ cm^{-2}.

Figure 5.5 displays typical TAS spectra of delta optical density (ΔOD) as a function of wavelength at t=0 ps for the IS samples formed at the three studied temperatures, as well as for the TA samples, following photoexcitation at 1026 nm with a pump fluence of 1.5 mJ cm-2. ΔOD is the change in absorption of the perovskite layer after photoexcitation and is calculated with the **Equation 2.1**.

The main ΔOD peak at ~740 nm is attributed to the transient photo-induced bleaching of the band edge transition, while a photo-induced transient absorption (PIA) in the range of 530-700 nm is additionally observed.[5,10-12] As we can see in **Figure 5.5**, there is a blue shift of the ΔOD peak for all IS samples compared to the reference TA ones, attributed to the different

thermal annealing procedures used for the IS and TA sample formation. Frost et al. have already shown the dependence of the $CH_3NH_3PbI_3$ bandgap on temperature changes. In particular, the bandgap of the perovskite increases as the lattice enlarges due to the increase of temperature.[30] This is the result of the splitting of the bonding and antibonding orbitals of $CH_3NH_3PbI_3$. Thus, the thermal extension of the lattice, due to temperature rise, affects the conduction band minimum as well as the valence band maximum leading to an overall bandgap increase.

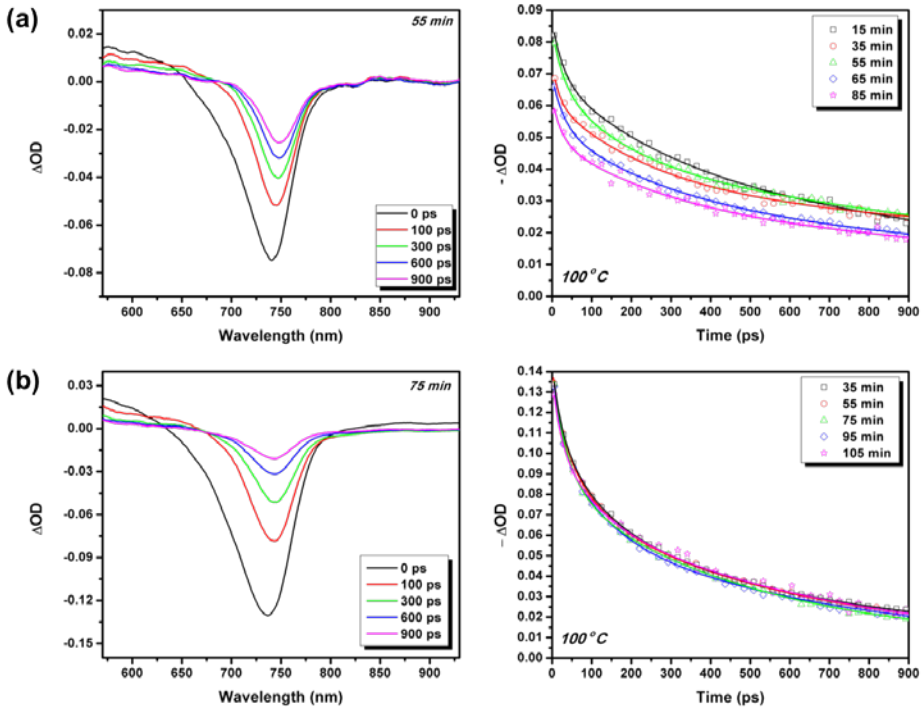

Figure 5.6: Typical TAS spectra of ΔOD as a function of wavelength and delay time of the PEDOT:PSS/$CH_3NH_3PbI_3$ (a) and PTAA/ $CH_3NH_3PbI_3$ (b) structures and corresponding ΔOD vs wavelength plots at various time delays following photoexcitation at 1026 nm with a pump fluence of 1.5 mJ cm^{-2} at 100 ^oC.

The time-resolved relaxation dynamics were thoroughly investigated following both an exponential[5,6,8,9,11,15,19,20] and polynomial fitting analysis.[1,5,7,11,13,14,16-18] From the exponential fitting analysis we have the ability to determine the critical time components of the charge

carrier transport processes between the perovskite film and the employed HTL polymers, while the polynomial one provides information on the kinetic rates for the charge carrier dynamics processes that occur in the perovskite film. **Figure 5.6** displays the typical ΔOD versus wavelength plots at various time delays for the two studied configurations at 100 ^{o}C, and the corresponding three-exponential fittings based on the **Equation 4.1**.

Furthermore, **Figure 5.7(a)** and **Figure 5.7(b)** depict the transient band edge bleach kinetics and the corresponding decay three-exponential fittings at 90 ^{o}C (left) and 110 ^{o}C (right) for PEDOT:PSS/$CH_3NH_3PbI_3$ and PTAA/$CH_3NH_3PbI_3$ configurations, respectively. The resolution of each measurement is 1 ps, but for the sake of presentation clarity, we used skip point 12 for all relaxation plots. All kinetic fit parameters for the two studied systems, as obtained at each temperature, are summarized in **Table 5.3** and **Table 5.4**; while the analysis for the error bars is describe in the **Appendix**.

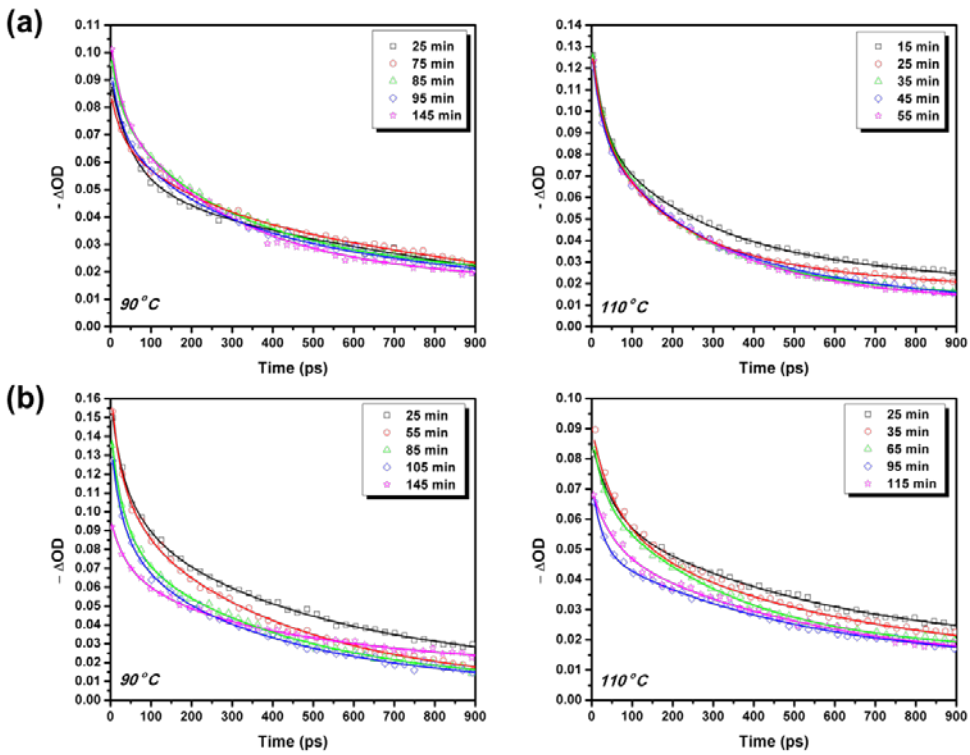

Figure 5.7: Transient band edge bleach kinetics (symbols) and the corresponding three-exponential fittings (lines) for the PEDOT:PSS/$CH_3NH_3PbI_3$ **(a)** and for PTAA/$CH_3NH_3PbI_3$ **(b)** architectures at 90 ^oC and 110 ^oC, photoexcited at 1026 nm with a pump fluence of 1.5 mJ cm^{-2}.

Table 5.3: Time Components for the PEDOT:PSS/$CH_3NH_3PbI_3$ Architectures Following Exponential Fitting ([a] Taken from (5)).

Minutes	λ_{max} (nm)	τ_1 (ps) ± 2 ps	τ_2 (ps) ± 8 ps	τ_3 (ps) ± 0.5x10^7 ps
[a]Thermal Annealing @ 100 ^oC				
30	753	43	257	1.2x10^5
In-situ TAS Annealing @ 90 ^oC				
25	738	45	185	2.7x10^7
75	737	25	210	1.7x10^7
85	738	22	105	3.2x10^7
95	739	25	235	8.6x10^6
145	737	25	276	2.1x10^7
In-situ TAS Annealing @ 100 ^oC				
15	742	29	321	6.8x10^6
35	744	29	267	1.5x10^7
55	742	22	190	1.3x10^7
65	737	31	310	8.0x10^7
85	743	35	303	1.2x10^7
In-situ TAS Annealing @ 110 ^oC				
15	731	29	257	1.5x10^7
25	731	22	210	8.7x10^6
35	731	24	225	1.9x10^7
45	731	24	230	1.7x10^7
55	731	24	257	1.4x10^7

Table 5.4: Time Components for the PTAA/$CH_3NH_3PbI_3$ Architectures Following Exponential Fitting ([a] Taken from (5)).

Minutes	λ_{max} (nm)	τ_1 (ps) ± 2 ps	τ_2 (ps) ± 8 ps	τ_3 (ps) ± 13 ps
[a]Thermal Annealing @ 100 °C				
30	750	10	101	717
In-situ TAS Annealing @ 90 °C				
25	741	21	69	506
55	737	18	53	418
85	732	17	48	418
105	731	21	74	444
145	739	29	110	540
In-situ TAS Annealing @ 100 °C				
35	737	20	85	508
55	736	22	83	574
75	734	21	60	504
95	734	21	124	833
105	740	22	102	660
In-situ TAS Annealing @ 110 °C				
25	736	50	522	522
35	737	19	63	429
65	736	30	338	338
95	739	26	503	503
115	739	51	510	510

In particular, the fast time component (τ_1) is attributed to the charge carrier trapping at the perovskite grain boundaries and perovskite/HTL interfaces[5,11,12] and not generally to the perovskite defects.[31,32] It represents the time required for the transition of an excited electron from the conduction band to the trap states. Smaller τ_1 times indicate quicker traps filling, leading to larger splitting in the quasi-Fermi energy levels resulting in the enhanced open-

circuit Voltage (V_{OC}) of the device. The V_{OC} is defined as the difference between the quasi-Fermi energies of electrons and holes in the solar cell under illumination. The quicker traps filling and the more efficient free charge carrier injection lead to considerably enhanced electrical characteristics of the perovskite films.[33,34] It's worth mentioning that τ_1 component is not only affected by the density of trap states, but also from their depth as well.[35] Notably, for the PEDOT:PSS/$CH_3NH_3PbI_3$ system at 90 ^oC, τ_1 decreases from 45 ps after an annealing time of 25 min of to 22 ps after 85 min and then increases again to 25 ps after 95 min where it stabilizes (**Table 5.3**). Similarly, for the sample annealed at 100 ^oC τ_1 drops from 29 ps after an annealing time of 15 min to 22 ps after 55 min and then rises up to 35 ps after 85 min (**Table 5.3**). Accordingly, τ_1 for sample annealed at 110 ^oC drops from 29 ps after an annealing time of 15 min to 22 ps after 25 min, and finally, stabilizes at 24 ps after 35 min (**Table 5.3**). These results reveal that, while the annealing period progresses, τ_1 decreases until the optimum (faster) value of 22 ps, which is indicative of the best quality perovskite film, and then increases again suggesting that further annealing is not favorable for the crystalline quality of the $CH_3NH_3PbI_3$ films.

The second-time component (τ_2) represents the time required for a hole injection from the perovskite layer to the HTL polymer including the corresponding time for the hole diffusion to the perovskite/HTL interface.[5,11,12] It is well-known that the faster the hole injection the better the electrical characteristics of the respective devices.[9,36] According to our results, at 90 ^oC, τ_2 drops from 185 ps after annealing time of 25 min to 105 ps after 85 min and then increases to 276 ps after 145 min of total annealing time. At 100 ^oC τ_2 decreases from 321 ps after annealing time of 15 min to 190 ps after 55 min, respectively, and then rises to 303 ps after 85 min of annealing. The same trend is observed at 110 ^oC, as τ_2 decreases from 257 ps to 210 ps after annealing time of 25 min and then increases to 257 ps after 55 min. Similar to

τ_1, τ_2 is following the same trend and reaches its optimum (lowest) value at the same annealing time period for the three studied temperatures. These annealing time periods are identified equal to 85, 55, and 25 min for the annealing temperatures of 90 ^oC, 100 ^oC, and 110 ^oC, respectively.

It should be noted that the IS PEDOT:PSS/$CH_3NH_3PbI_3$ samples exhibit significant faster τ_2 time components compared to the τ_2 of the TA samples (**Table 5.3**).[5] Thus, the IS samples are expected to exhibit potentially better electrical characteristics that the TA ones, which complies with the observed higher relative peak intensity ratio $CH_3NH_3PbI_3/PbI_2$ in the XRD patterns of **Figure 5.2** (**Table 5.2**). It is well known that the excess of PbI_2 is harmful for the composition and optical properties of the perovskite film, while it can be beneficial for the electrical performance.[24,26-29] **Table 5.3** also lists the third long-life time component (τ_3), which is representative of the exciton recombination time.[5,11,12] For all studied temperatures and annealing periods, the τ_3 time component was found to be of the same order of magnitude, i.e. decades of μs.

In the case of PTAA/$CH_3NH_3PbI_3$ system at 90 ^oC τ_1 decreases from 21 ps after annealing time of 25 min to 17 ps after 85 min and then increases to 29 ps after 145 min, while at 100 ^oC τ_1 remains constant at around 21 ps (**Table 5.4**). Moreover, τ_1 at 110 ^oC drops from 50 ps to 19 ps after annealing time of 25 min and 35 min, respectively, and then increases to 51 ps after 115 min (**Table 5.4**). While, τ_2 at 90 ^oC, drops from 69 ps after annealing time of 25 min to 48 ps after 85 min and then increases to 110 ps after 145 min. At 100 ^oC τ_2 decreases from 85 ps after annealing time of 35 min to 60 ps after 75 min, and then rises to 102 ps after 105 min. A similar trend is observed at 110 ^oC, where τ_2 decreases from 522 ps to 63 ps after annealing time of 35 min and then increases to 510 ps after 115 min. Therefore, for the

PTAA/$CH_3NH_3PbI_3$ system, the optimum annealing time periods for both τ_1 and τ_2 time components are found to be the same regardless the annealing temperature. Besides this, the optimum annealing time periods are revealed to be longer compared to the corresponding periods for the PEDOT:PSS/$CH_3NH_3PbI_3$ system. Thus, for the case of PTAA polymer longer annealing periods are required in order to achieve optimum charge transfer dynamics, at least for the two higher crystallization temperatures of 100 ^oC and 110 ^oC. Namely, the optimum annealing time periods are identified equal to 85, 75, and 35 min for the annealing temperatures of 90 ^oC, 100 ^oC, and 110 ^oC, respectively. Finally, **Table 5.4** includes the τ_3 time component (recombination time) for PTAA/perovskite configuration. For all studied temperatures and annealing time periods, this time component was found to be of the same order of magnitude (hundreds of picoseconds).

It should be emphasized that at the optimum annealing time periods, the PTAA/$CH_3NH_3PbI_3$ IS samples exhibit faster τ_2 time component compared to that of the TA samples (**Table 5.4**). Such faster charge carrier dynamics are accompanied by a significantly lower $CH_3NH_3PbI_3/PbI_2$ XRD peak ratio (**Figure 4.2** and **Figure 5.2** and **Table 5.2**). Therefore, in the case of the more hydrophobic PTAA polymer, the in-situ TAS annealing process results to excessive presence of residual PbI_2.

We perform also the well-established polynomial fitting model based on the rate **Equation 4.2**. Wehrenfennig et al.[7] have reported on the correlation between the k_2 bimolecular recombination rate and the efficiency of the PSCs. It is particularly proposed that slower k_2 rates are indicative of longer free-charge carrier diffusion lengths, that consequently result in better performance of the planar heterojunction devices.

Table 5.5 lists the kinetic rates for the PEDOT:PSS/$CH_3NH_3PbI_3$ system for the TA and IS samples at the optimum crystallization annealing time period, while **Table 5.6** includes the corresponding rates for the PTAA/$CH_3NH_3PbI_3$ system. The errors for the recombination rates for both configurations, are calculated from the fitting procedure with the same way as in exponential fitting model (**Appendix**). It is clear that all the IS samples exhibit smaller k_2 rates compared to those of TA ones. Moreover, the slower bimolecular recombination rates for both configurations occurs at 90 ^oC, which complies with the faster τ_2 time component of the PEDOT:PSS/$CH_3NH_3PbI_3$ and PTAA/$CH_3NH_3PbI_3$ systems (**Table 5.5** and **Table 5.6**). The above findings are also in agreement with the larger grains size and the higher $CH_3NH_3PbI_3/PbI_2$ peak ratio obtained from the XRD patterns in case of PEDOT:PSS/$CH_3NH_3PbI_3$ at 90 ^oC. On the contrary, in the case of PTAA/$CH_3NH_3PbI_3$, the larger grains size and the higher $CH_3NH_3PbI_3/PbI_2$ peak ratio are observed at 110 ^oC, while the faster carrier injection and slower bimolecular recombination rate are observed at 90 ^oC. These results indicate that for the PTAA/$CH_3NH_3PbI_3$ configuration, the perovskite layer crystallinity and the corresponding charge carrier dynamics are more affected by the thermal crystallization history, compared to the PTAA/$CH_3NH_3PbI_3$ configuration.

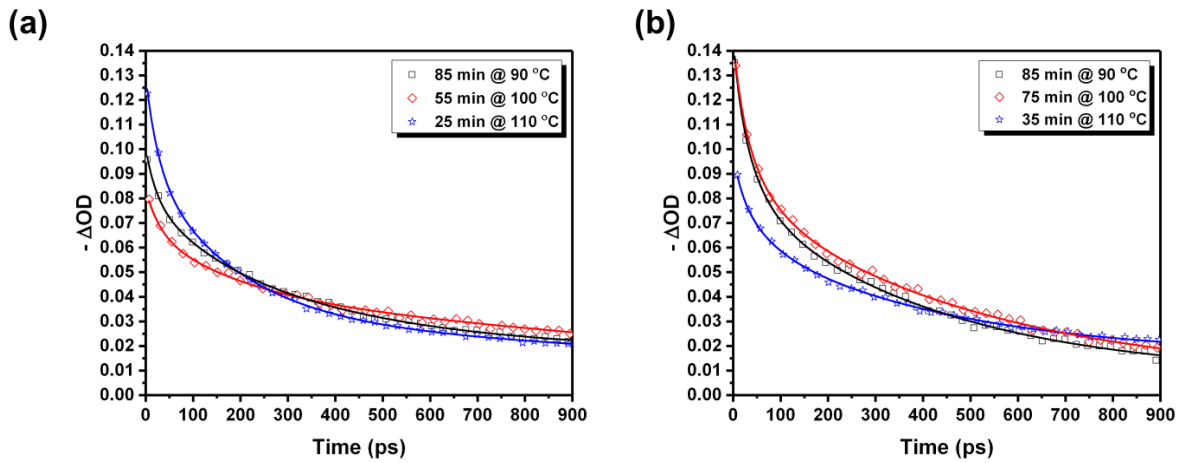

Figure 5.8: Transient band edge bleach kinetics (symbols) and the corresponding polynomial fittings PEDOT:PSS/$CH_3NH_3PbI_3$ (a) and for PTAA/$CH_3NH_3PbI_3$ (b) at the optimum crystallization period, photoexcited at 1026 nm with a pump fluence of 1.5 mJ cm^{-2}.

Table 5.5: Recombination Rate Constants for the PEDOT:PSS/$CH_3NH_3PbI_3$ Architectures Following Polynomial Fitting ([a] Taken from (5)).

Minutes	λ_{max} (nm)	$k_3 \pm 0.4x10^{-16}$ (cm^6s^{-1})	$k_2 \pm 0.2x10^{-12}$ (cm^3s^{-1})	$k_1 \pm 0.1x10^{-7}$ (μs^{-1})
[a]Thermal Annealing @ 100 °C				
30	753	$7.3x10^{-14}$	$3.6x10^{-11}$	$4.4x10^{-6}$
In-situ TAS Annealing @ 90 °C				
85	738	$7.4x10^{-16}$	$2.4x10^{-12}$	$1.2x10^{-7}$
In-situ TAS Annealing @ 100 °C				
55	742	4.5×10^{-16}	$3.3x10^{-12}$	$8.7x10^{-7}$
In-situ TAS Annealing @ 110 °C				
25	731	$1.2x10^{-15}$	$3.6x10^{-12}$	$2.2x10^{-7}$

Table 5.6: Recombination Rate Constants for the PTAA/$CH_3NH_3PbI_3$ Architectures Following Polynomial Fitting ([a] Taken from (5)).

Minutes	λ_{max} (nm)	$k_3 \pm 0.4x10^{-15}$ (cm^6s^{-1})	$k_2 \pm 0.2x10^{-12}$ (cm^3s^{-1})	$k_1 \pm 0.1x10^{-6}$ (μs^{-1})
[a]Thermal Annealing @ 100 °C				
30	750	$3.8x10^{-14}$	$1.7x10^{-11}$	$3.1x10^{-6}$
In-situ TAS Annealing @ 90 °C				
85	732	$1.8x10^{-15}$	$2.2x10^{-12}$	$1.8x10^{-6}$
In-situ TAS Annealing @ 100 °C				
75	734	$1.7x10^{-15}$	$4.8x10^{-12}$	$1.7x10^{-6}$
In-situ TAS Annealing @ 110 °C				
35	737	$3.4x10^{-15}$	$4.1x10^{-12}$	$3.4x10^{-6}$

In summary, it was found that, all IS samples for both configurations tested exhibited faster charge carrier dynamics and slower recombination rates compared with the corresponding TA samples. Namely, in the case of PEDOT:PSS/$CH_3NH_3PbI_3$ the faster charge carrier

dynamics and slower recombination rates are obtained at 90 ^{o}C which is in agreement with the best obtained crystalline quality of the perovskite film as revealed from the XRD pattern (highest $CH_3NH_3PbI_3/PbI_2$ peak ratio), and larger perovskite grain sizes as emerged from SEM studies. On the contrary, in the case of PTAA/$CH_3NH_3PbI_3$ architecture, the highest $CH_3NH_3PbI_3/PbI_2$ peak ratio and larger perovskite grain sizes are observed are 110 ^{o}C, whereas the faster carrier dynamics and slower recombination rates are exhibited at 90 ^{o}C. Based on the above it is revealed that the different thermal history of the in-situ (IS) TAS crystallization process does not affect the formation of the perovskite film upon employing the more hydrophilic PEDOT:PSS polymer as HTL. Rather differently, a discrepancy is noticed in the case of PTAA/perovskite configuration as the optimum charge extraction processes and crystalline morphology are obtained at different temperatures. It is worth to stress out, that this effect is not observed when the typical thermal annealing route is followed for the same architectures. Furthermore, when the more hydrophilic PEDOT:PSS is employing as HTL, faster annealing periods are required in order to achieve the most efficient charge extraction properties at each temperature, compared with the corresponding period for PTAA/$CH_3NH_3PbI_3$ architecture.

5.3 Conclusions

In this Chapter, in order to study the effect of the surface nature of the employed HTL polymers in the crystallization of the perovskite, we monitored in-situ the evolution of charge extraction dynamics of $CH_3NH_3PbI_3$ films throughout the crystallization process that took place at three different thermal annealing temperatures by means of TAS. It was found that the different crystallization procedure and different thermal history for the in-situ (IS) samples seem to favor the formation of the perovskite layer deposited onto the more hydrophilic PEDOT:PSS polymer. On the contrary, when the more hydrophobic PTAA

polymer is used, the in-situ crystallization routes disrupt the crystallization of the perovskite film. As a consequence, longer annealing periods are required in order to achieve the most efficient charge extraction properties. Therefore, the duration of thermal annealing for developing perovskite films with optimum charge extraction dynamics strongly depends on the surface nature of the employed HTL polymer.

References:

1. Draguta, S.; Christians, J. A.; Morozov, Y. V.; Mucunzi, A.; Manser, J. S.; Kamat, P. V.; Luther, J. M.; Kuno, M. A Quantitative and Spatially Resolved Analysis of the Performance-Bottleneck in High Efficiency, Planar Hybrid Perovskite Solar Cells. *Energy Environ. Sci.* **2018**, *11*, 960.
2. Sherkar, T. S.; Momblona, C.; Gil-Escrig, L.; Ávila, J.; Sessolo, M.; Bolink, H. J.; Koster, L. J. A. Recombination in Perovskite Solar Cells: Significance of Grain Boundaries, Interface Traps, and Defect Ions. *ACS Energy Lett.* **2017**, *2*, 1214-1222.
3. Sha, W. E.; Ren, X.; Chen, L.; Choy, W. C. The Efficiency Limit of $CH_3NH_3PbI_3$ Perovskite Solar Cells. *Appl. Phys. Lett.* **2015**, *106*, 221104.
4. Sandberg, O. J.; Sundqvist, A.; Nyman, M.; Österbacka, R. Relating Charge Transport, Contact Properties, and Recombination to Open-Circuit Voltage in Sandwich-Type Thin-Film Solar Cells. Phys. Rev. Appl. **2016**, *5*, 044005.
5. Serpetzoglou, E.; Konidakis, I.; Kakavelakis, G.; Maksudov, T.; Kymakis, E.; Stratakis, E. Improved Carrier Transport in Perovskite Solar Cells Probed by Femtosecond Transient Absorption Spectroscopy. *ACS Appl. Mater. Interfaces*, **2017**, *9*, 43910-43919.
6. Kakavelakis, G.; Maksudov, T.; Konios, D.; Paradisanos, I.; Kioseoglou, G.; Stratakis, E.; Kymakis, E. Efficient and Highly Air Stable Planar Inverted Perovskite Solar Cells with Reduced Graphene Oxide Doped PCBM Electron Transporting Layer. *Adv. Energy Mater.* **2016**, *7*, 1602120.
7. Wehrenfennig, C.; Eperon, G. E.; Johnston, M. B.; Snaith, H. J.; Herz, L. M. High Charge Carrier Mobilities and Lifetimes in Organolead Trihalide Perovskites. *Adv. Mater.* **2014**, *26*, 1584.
8. Ishioka, K.; Barker, B. G.; Yanagida, M.; Shirai, Y.; Miyano, K. Direct Observation of Ultrafast Hole Injection from Lead Halide Perovskite by Differential Transient Transmission Spectroscopy. *J. Phys. Chem. Lett.* **2017**, *8*, 3902.
9. Zhu, Z.; Ma, J.; Wang, Z.; Mu, C.; Fan, Z.; Du, L.; Yang B.; Fan L.; Yan H.; Phillips D. L.; Yang, S. Efficiency Enhancement of Perovskite Solar Cells Through Fast Electron Extraction: The Role of Graphene Quantum Dots. *J. Am. Chem. Soc.* **2014**, *136*, 3760.
10. Stranks, S. D.; Eperon, G. E.; Grancini, G.; Menelaou, C.; Alcocer, M. J. P.; Leijtens, T.; Herz, L. M.; Petrozza, A.; Snaith, H. J. Electron-Hole Diffusion Lengths Exceeding 1 micrometer in an Organometal Trihalide Perovskite Absorber. *Science* **2013**, *342*, 341− 344.
11. Konidakis, I.; Maksudov, T.; Serpetzoglou, E.; Kakavelakis, G.; Kymakis. E.; Stratakis, E. Improved Charge Carrier Dynamics of $CH_3NH_3PbI_3$ Perovskite Films Synthesized by Means of Laser- assisted Crystallization. *ACS Appl. Energy Mater.* **2018**, *1*, 5101-5111.
12. Wang, L.; McCleese, C.; Kovalsky, A.; Zhao, Y.; Burda, C. Femtosecond Time-Resolved Transient Absorption Spectroscopy of $CH_3NH_3PbI_3$ Perovskite Films: Evidence for Passivation Effect of PbI_2. *J. Am. Chem. Soc.* **2014**, *136*, 12205-12208.

13. Klein, J. R.; Flender, O.; Scholz, M.; Oum, K.; Lenzer, T. Charge Carrier Dynamics of Methylammonium Lead Iodide: from PbI_2-rich to Low-Dimensional Broadly Emitting Perovskites. *Phys. Chem. Chem. Phys*. **2016**, *18*, 10800.
14. Manser, J. S.; Kamat, P. V. Band Filling with Free Charge Carriers in Organometal Halide Perovskites. *Nat. Photonics* **2014** *8*, 737.
15. Corani, A.; Li, M. H.; Shen, P. S.; Chen, P.; Guo, T. F.; El Nahhas, A.; Zheng, K.; Yartsev, A.; Sundstrom, V.; Ponseca Jr, C. S. Ultrafast Dynamics of Hole Injection and Recombination in Organometal Halide Perovskite Using Nickel Oxide as p-Type Contact Electrode. *J. Phys. Chem. Lett* **2016**, *7*, 1096.
16. Stranks, S. D.; Burlakov, V. M.; Leijtens, T.; Ball, J. M.; Goriely, A.; Snaith, H. J. Recombination Kinetics in Organic-Inorganic Perovskites: Excitons, Free Charge, and Subgap States. *Phys. Rev. Appl.* **2014**, *2*, 034007.
17. Piatkowski, P.; Cohen, B.; Ramos, F. J.; Di Nunzio, M.; Nazeeruddin, M. K.; Grätzel, M.; Ahmad, S.; Douhal, A. Direct Monitoring of Ultrafast Electron and Hole Dynamics in Perovskite Solar Cells. *Phys. Chem. Chem. Phys*. **2015**, *17*, 14674.
18. La-o-vorakiat, C.; Salim, T.; Kadro, J.; Khuc, M. T.; Haselsberger, R.; Cheng, L.; Xia, H.; Gurzadyan, G. G.; Su, H.; Lam, Y. M.; Marcus, R. A.; Michel-Beyerle, M. E.; Chia, E. E. M. Elucidating the Role of Disorder and Free-Carrier Recombination Kinetics in $CH_3NH_3PbI_3$ Perovskite Films. *Nat. Commun*. **2015**, *6*, 7903.
19. Ghosh, T.; Aharon, S.; Etgar, L.; Ruhman, S. Free Carrier Emergence and Onset of Electron–Phonon Coupling in Methylammonium Lead Halide Perovskite Films. *J. Am. Chem. Soc*. **2017**, *139*, 18262.
20. Zhai, Y.; Sheng; C. X.; Zhang, C.; Vardeny, Z. V. Ultrafast Spectroscopy of Photoexcitations in Organometal Trihalide Perovskites. *Adv. Funct. Mater*. **2016**, *26*, 1617.
21. Leng, J.; Liu, J.; Zhang, J.; Jin, S. Decoupling Interfacial Charge Transfer from Bulk Diffusion Unravels its Intrinsic Role for Efficient Charge Extraction in Perovskite Solar Cells. *J. Phys. Chem. Lett.* **2016**, *7*, 5056-5061.
22. Li, F.; Zhu, W.; Bao, C.; Yu, T.; Wang, Y.; Zhou, X.; Zou, Z. Laser-assisted Crystallization of $CH_3NH_3PbI_3$ Films for Efficient Perovskite Solar Cells with a High Open-Circuit Voltage. *Chem. Commun.* **2016**, *52*, 5394.
23. Chen, Q.; Zhou, H.; Hong, Z.; Luo, S.; Duan, H. S.; Wang, H. H.; Liu, Y.; Li, G.; Yang, Y. Planar Heterojunction Perovskite Solar Cells via Vapor-Assisted Solution Process. *J. Am. Chem. Soc*. **2013**, *136*, *622*.
24. Chen, Q.; Zhou, H.; Song, T. B.; Luo, S.; Hong, Z.; Duan, H. S.; Dou, L.; Liu, Y. Yang, Y. Controllable Self-Induced Passivation of Hybrid Lead Iodide Perovskites Toward High Performance Solar Cells. *Nano Lett.* **2014**, *14*, 4158.
25. Huang, J. H.; Jiang, K. J.; Cui, X. P.; Zhang, Q. Q.; Gao, M.; Su, M. J.; Song, Y. Direct Conversion of $CH_3NH_3PbI_3$ from Electrodeposited PbO for Highly Efficient Planar Perovskite Solar Cells. *Sci. Rep.* **2015**, *5*, 15889.
26. Pathak, S.; Sepe, A.; Sadhanala, A.; Deschler, F.; Haghighirad, A.; Sakai, N.; Goedel, K. C.; Stranks, S. D.; Noel, N.; Price, M.; et al. Atmospheric Influence upon Crystallization and Electronic Disorder and Its Impact on the Photophysical

Properties of Organic–Inorganic Perovskite Solar Cells. *ACS Nano* **2015**, *9*, 2311-2320.

27. Somsongkul, V.; Lang, F.; Jeong, A. R.; Rusu, M.; Arunchaiya, M.; Dittrich, T. Hole Blocking $PbI_2/CH_3NH_3PbI_3$ Interface. *Phys. Status Solidi RRL*. **2014**, *8*, 763.
28. Bi, D.; Tress, W.; Dar, M. I.; Gao, P.; Luo, J.; Renevier, C.; Schenk, K.; Abate, A.; Giordano, F.; Baena, J. B. C.; Decoppet, J. D; Zakeeruddin, S. M.; Nazeeruddin, M. K.; Graetzel, M.; Hagfeldt, A. Efficient Luminescent Solar Cells Based on Tailored Mixed-Cation Perovskites. *Sci. Adv*. **2016**, *2*, e1501170.
29. Zhang, T.; Guo, N.; Li, G.; Qian, X.; Zhao, Y. A. Controllable Fabrication of Grain Boundary PbI_2 Nanoplates Passivated Lead Halide Perovskites for High Performance Solar Cells. Nano Energy, **2016**, *26*, 50-56.
30. Frost, J. M.; Butler, K. T.; Brivio, F.; Hendon, C. H.; Van Schilfgaarde, M.; Walsh, A. (2014). Atomistic Origins of High-Performance in Hybrid Halide Perovskite Solar Cells. *Nano Lett.* **2014**, *14*, 2584.
31. Pydzińska, K.; Karolczak, J.; Szafrański, M.; Ziółek, M. Differences in Photoinduced Optical Transients in Perovskite Absorbers for Solar Cells. *RSC Adv.* **2018**, *8*, 6479-6487.
32. Snaider, J. M.; Guo, Z.; Wang, T.; Yang, M.; Yuan, L.; Zhu, K.; Huang, L. Ultrafast Imaging of Carrier Transport across Grain Boundaries in Hybrid Perovskite Thin Films. *ACS Energy Lett.* **2018**, *3*, 1402-1408.
33. Shao, S.; Abdu-Aguye, M.; Sherkar, T. S.; Fang, H. H.; Adjokatse, S.; Brink, G. T.; Kooi, B. J.; Koster, L. J. A.; Loi, M. A. The Effect of the Microstructure on Trap-Assisted Recombination and Light Soaking Phenomenon in Hybrid Perovskite Solar Cells. *Adv. Funct. Mater*. **2016**, *26*, 8094.
34. Leijtens, T.; Stranks, S. D.; Eperon, G. E.; Lindblad, R.; Johansson, E. M.; McPherson, I. J.; Rensmo, H.; Ball, J. M.; Lee, M. M.; Snaith, H. J. Electronic Properties of Meso-Superstructured and Planar Organometal Halide Perovskite Films: Charge Trapping, Photodoping, and Carrier Mobility. *ACS Nano* **2014**, *8*, 7147.
35. Leijtens, T.; Eperon, G. E.; Barker, A. J.; Grancini, G.; Zhang, W.; Ball, J. M.; Kandada, A. R. S.; Snaith H. J.; Petrozza, A. Carrier Trapping and Recombination: The Role of Defect Physics in Enhancing the Open Circuit Voltage of Metal Halide Perovskite Solar Cells. *Energy Environ. Sci.* **2016**, *9*, 3472.
36. Tao, C.; Neutzner, S.; Colella, L.; Marras, S.; Kandada, A. R. S.; Gandini, M.; De Bastiani, M.; Pace, G.; Manna, L.; Caironi, M.; Bertarelli, C.; Petrozza, A. 17.6% Stabilized Efficiency in Low-Temperature Processed Planar Perovskite Solar Cells. *Energy Environ. Sci.* **2015**, *8*, 2365−2370.

Chapter 6

Charge Carrier Dynamics in Different Perovskite Crystal Phases

In this Chapter, TAS measurements in various perovskite/HTL configurations were performed at temperatures below room temperature, in order to shed light on the charge carrier dynamics of different perovskite crystalline phases, while considering also the effect of the employed HTL polymer (**Figure 6.1**).

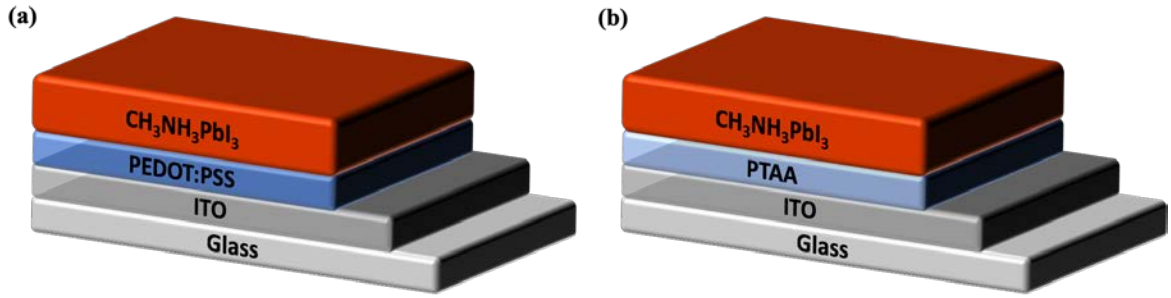

Figure 6.1: Schematic illustration of the two configurations **(a)** PEDOT:PSS/$CH_3NH_3PbI_3$ and **(b)** PTAA/$CH_3NH_3PbI_3$ that used in this study.

In this study, $CH_3NH_3PbI_3$ films were deposited on PEDOT:PSS and PTAA, that are known offering different charge carrier dynamics in perovskite solar cells and in perovskite/HTL architecture, as well (**Chapter 4**). Namely, perovskite/HTL configurations were studied at 85, 120 and 180 K in order to explore the dynamics of the orthorhombic and the tetragonal phases of perovskite films deposited on PEDOT:PSS and PTAA polymers. It is revealed that the charge carrier dynamics (hole injection and free carrier recombination) are strongly depended from the pervoskite crystal phase, as well as, from the employing hole transport material.

6.1 Introduction

A very crucial and unexplored area in the field of the perovskite solar cells, is the charge carrier dynamics in different crystal phases that the $CH_3NH_3PbI_3$ presents. The understanding of this effect is necessary for low temperature applications, such as the use of the PSCs in satellites or in space stations and to realize the behavior of the perovskite layer even at conditions with low temperatures. In particular, the lattice of the methylammonium lead iodide is orthorhombic below of 167 K, tetragonal from 167 K up to 327 K and cubic from 327 K and above.[1] As we reach the transition temperature of 167 K, the main peak is attributed to the orthorhombic phase, but we can detect also the peak from the tetragonal phase. It is well known, that the methylammonium cations in the perovskite A-site, in the tetragonal and cubic phases, show free rotation, resulting in the increase in the dielectric function, while in the orthorhombic phase, the organic cations are not free to rotate.[2,3] This free rotation is attributed to exciton binding energy,[4,5] charge carrier transport and recombination,[4-12] and to intraband relaxation.[13-15]

Nevertheless, there is still significant lack of understanding how the hole transport materials affect the charge extraction processes as well as the recombination dynamics on different crystal phases of the perovskite layer. Milot et al.[12] and Dirol[16] have studied the charge carrier dynamics in variable temperature only in bare glass and thick sapphire windows substrate, respectively, without take into account the influence of the HTL into the charge carrier dynamics.

In this Chapter, the charge carrier dynamics of the perovskite film are studied at variable low temperatures by means of transient absorption spectroscopy. This approach allows us to explore how the different perovskite crystal phases upon two different HTL polymers

(**Figure 6.1**) affect the charge carrier transport and recombination rates for each configuration based on the extracted time components and recombination rates. Namely, the charge carrier properties were studied at three different low temperatures, i.e. 85 K, 120 K and 180 K, while employing two different HTL polymers, i.e. the more hydrophilic, PEDOT:PSS, and the more hydrophobic, PTAA.

6.2 Results and Discussion

6.2.1 Temperature-Dependent Absorption Peak

Before starting to explore the charge carrier dynamics of the PEDOT:PSS/MAPI and PTAA/MAPI configurations, we have to evidence that at low temperatures we are able to detect both perovskite crystal phases, the orthorhombic and the tetragonal. **Figure 6.2** shows the absorption peaks wavelength that are extracted from the typical TAS spectra at t = 0 ps as a function temperature, i.e. the latter spectra depicted in Figures 6.3 and 6.4. It becomes apparent that both configurations exhibit the same trend for both orthorhombic and tetragonal phases. In particular, the characteristic peak of the orthorhombic phase drops from 737 nm to 730 nm for PEDOT:PSS/MAPI configuration and from 727 nm to 724 nm for PTAA/MAPI architecture, when the temperature increases from 85 K to 120 K, where the both perovskite crystal phases coexist. This widening of the bandgap is in contrast with the Varshni behavior that standard tetrahedral semiconductors show, in which the bandgap presents a redshift with the increase in temperature.[17,18] Rather differently, the obtained redshift (from 120 K to 85 K) can be explained by the fact that cooling the MAPI below the transition temperature, the methylammonium (MA) cations it is possible to kinetically trap in disordered configuration in an ordered orthorhombic phase of $CH_3NH_3PbI_3$, resulting to decrease the bandgap of the perovskite layer.[18,19]

Furthermore, when the temperature increases further from 120 K to 155 K, the absorption peak that is attributed to the tetragonal phase, increases from 766 nm to 770 nm for PEDOT:PSS/MAPI configuration and from 760 nm to 767 nm for PTAA/MAPI architecture. The obtained redshift is indicative for the change from the orthorhombic to the tetragonal phase, and is a result of changes in methylammonium disorder and spin-orbit coupling.[19-21] Moreover, when the temperature increases from 155 K to 215 K, the absorption peak decreases from 770 nm to 757 nm for the first architecture, and from 767 nm to 753 for the latter. Dar et al. have shown that the MA-ordered domains (T < transition temperature) have larger bandgap than the MA-disordered domains (at the tetragonal phase), which is in agreement with our experimental results (**Figure 6.2**) comparing the orthorhombic with the tetragonal phase; and also, that blueshift of the absorption peak in the tetragonal phase is due to the thermal expansion of the $CH_3NH_3PbI_3$ lattice.[22]

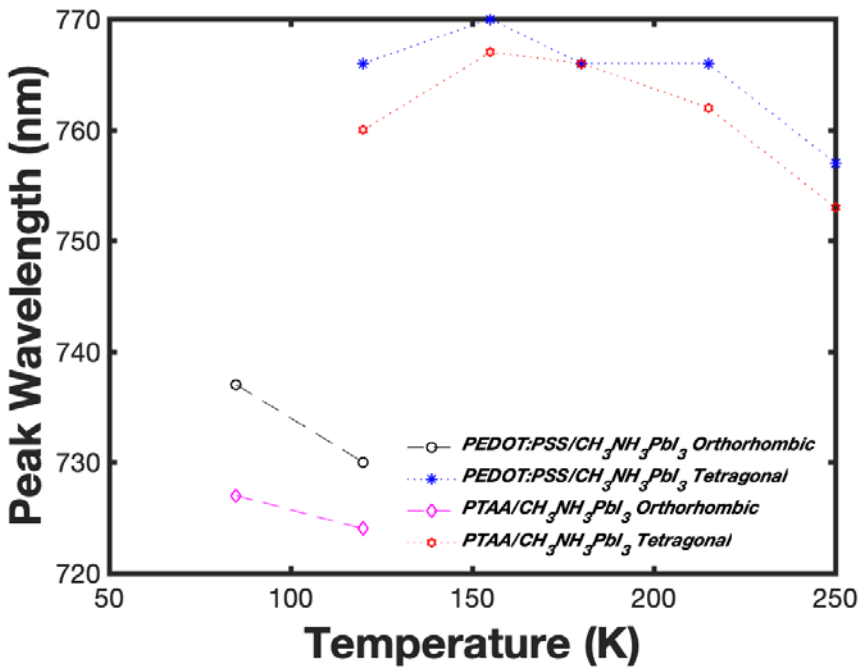

Figure 6.2: Absorption peaks wavelength as a function of temperature for both configuration for studied temperatures, extracted from TAS spectra at t = 0 ps (see text).

6.2.2 Temperature-Dependent Time-Resolved Absorption Spectroscopy

It is very important to understand the charge carrier dynamics of the perovskite solar cells and how the employing hole transport layer affect them, in different perovskite crystal structure. The understanding of this effect is necessary for low temperature applications, such as the use of the PSCs in satellites or in space stations and to realize the behavior of the perovskite layer even at conditions with low temperatures. For this purpose, we monitor the dynamics at 85 K (orthorhombic phase), at 120 K, where the two phases coexist (orthorhombic and tetragonal), and at 180 K (tetragonal phase).

Figure 6.3 and **Figure 6.4** display the typical TAS spectra of delta optical density as a function of wavelength at various delay times, for PEDOT:PSS/$CH_3NH_3PbI_3$ and PTAA/$CH_3NH_3PbI_3$, respectively, following photoexcitation at 1026 nm with pump fluence of 1 mJ cm^{-2}. ΔOD is the change in absorption of the perovskite layer after photoexcitation and is calculated with the **Equation 2.1**.

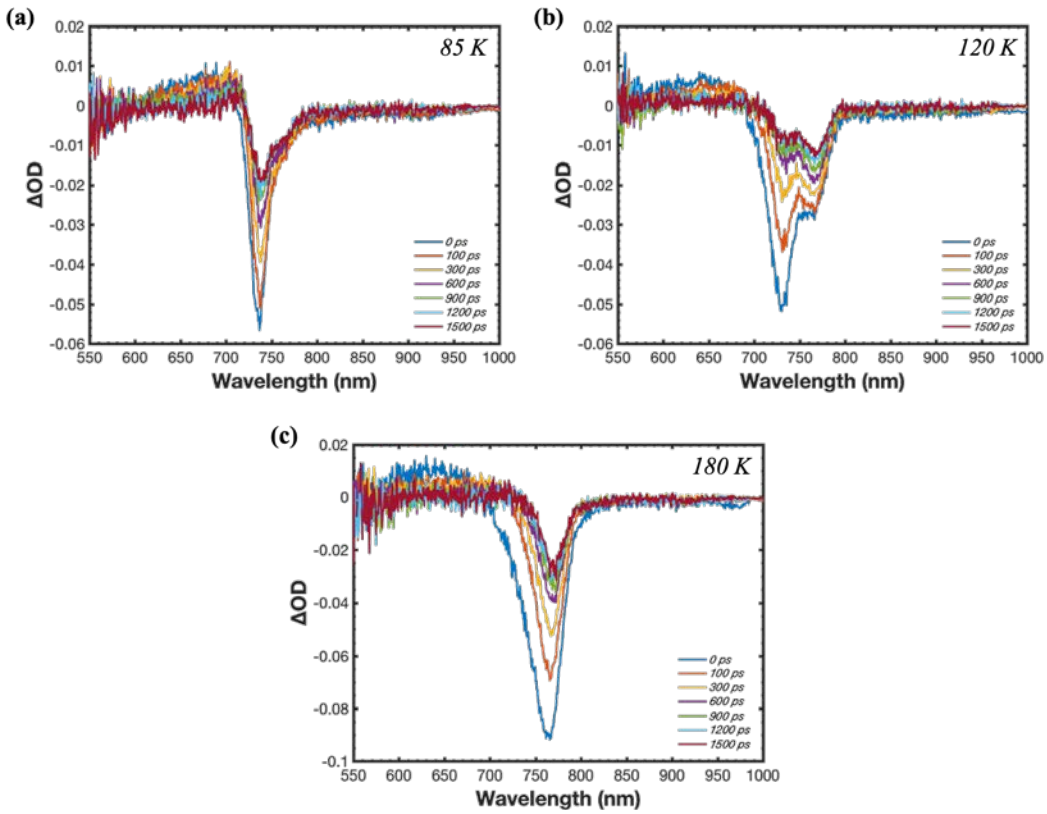

Figure 6.3: Delta optical density versus wavelength at various delay times for PEDOT:PSS/$CH_3NH_3PbI_3$ architecture at **(a)** 85 K, **(b)** 120 K and **(c)** 180 K.

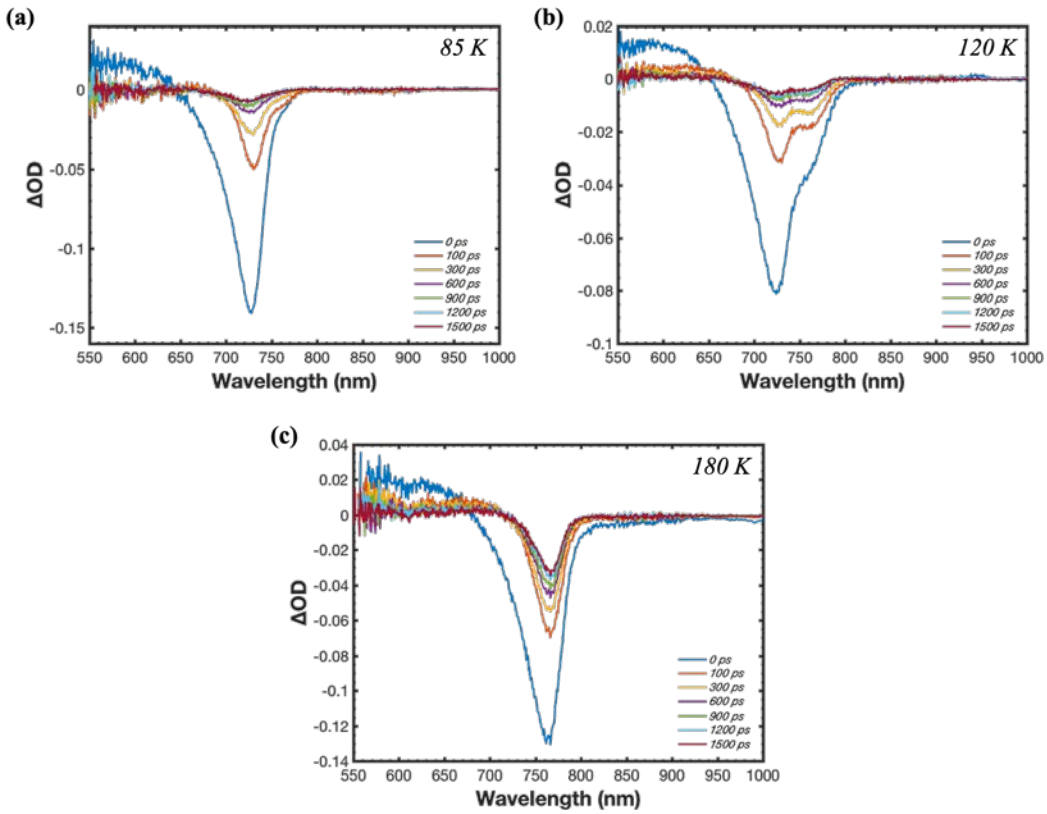

Figure 6.4: Delta optical density versus wavelength at various delay times for PTAA/$CH_3NH_3PbI_3$configuration at (a) 85 K, (b) 120 K and (c) 180 K.

The main ΔOD peaks at ~735 nm (**Figure 6.3(a), (b)** and **Figure 6.4(a), (b)**) and at ~760 nm (**Figure 6.3(b), (c)** and **Figure 6.4(b), (c)**) are attributed to the transient photo-induced bleaching of the band edge transition of the orthorhombic and the tetragonal phase, respectively. While a photo-induced transient absorption (PIA) in the range of 550-700 nm is additionally observed.

We perform the fitting analysis, using the two well established models, namely, the three-exponential (**Equation 4.1**)[23-31] and high-order polynomial model (**Equation 4.2**).[23,27,31-38] The kinetic time components, as well as the bimolecular recombination rate (k_2) for three studied temperatures, i.e. 85 K, 120 K and 180 K, for PEDOT:PSS/$CH_3NH_3PbI_3$ and PTAA/$CH_3NH_3PbI_3$ configurations are summarized in **Table 6.1.**

Table 6.1 displays the τ_1 time components, which is attributed to the charge carrier trapping at the perovskite grain boundaries and perovskite/HTL interfaces.[23,27,31] In case of PEDOT:PSS/$CH_3NH_3PbI_3$ the τ_1 increases as the temperature rises, meaning that the trapping becomes slower and/or the density of the traps has increased. On the other hand, in case of PTAA/$CH_3NH_3PbI_3$ the τ_1 is similar for all studied temperatures, implying that it is independent of the perovskite crystal phase.

Table 6.1: Time Components and Bimolecular Recombination Rate (k_2) for the PEDOT:PSS/$CH_3NH_3PbI_3$ and PTAA/$CH_3NH_3PbI_3$ architectures.

Tempe-rature	PEDOT:PSS					PTAA				
	λ_{max} (nm)	$\tau_1 \pm 2$ (ps)	$\tau_2 \pm 8$ (ps)	$\tau_3 \pm 13$ (ps)	$k_2 \pm 0.2 \times 10^{-10}$ ($cm^3 s^{-1}$)	λ_{max} (nm)	$\tau_1 \pm 2$ (ps)	$\tau_2 \pm 8$ (ps)	$\tau_3 \pm 13$ (ps)	$k_2 \pm 0.2 \times 10^{-10}$ ($cm^3 s^{-1}$)
85	737	6.1	562	562	9.9×10^{-10}	727	6.2	296	296	9.1×10^{-10}
120	730	12	171	962	9.9×10^{-10}	724	5.7	64	324	3.8×10^{-10}
	766	16.7	449	995	1.3×10^{-9}	760	7.3	137	362	6.6×10^{-10}
180	752	14.7	266	933	1.2×10^{-10}	766	5.7	57	1839	1.0×10^{-10}

The second-time component (τ_2) represents the time required for a hole injection from the perovskite to the HTL polymer.[23,27,31]We can see that for both phases (orthorhombic at ~730 nm and tetragonal at ~760 nm) the hole injection time component (τ_2) decreases as the temperature increases. In particular, for PEDOT:PSS/$CH_3NH_3PbI_3$ architecture in the orthorhombic phase, the τ_2 is decreased by almost a factor 5, from 562 ps to 171 ps, when the temperature increases from 85 K to 120 K. While, in tetragonal phase, the hole injection time is reduced around two times from 449 ps to 266 ps, when the temperature rises from 120 K to 180 K. Similar trends are also observed in PTAA/$CH_3NH_3PbI_3$ configurations. For the peak of the orthorhombic phase the τ_2 is decreased by a factor 5, from 296 ps to 64 ps, and for the

tetragonal phase the hole injection time decreased by almost a factor 3, from 137 ps to 57 ps. **Table 6.1** lists also the third-time component (τ_3), which is representative of the electron-hole recombination. The τ_3 is increased as the temperature increases, meaning that the free carriers are available longer periods in the perovskite film in order to approach the perovskite/HTL interface and inject into the transport layer polymer.

Finally, **Table 6.1** includes the bimolecular recombination rate which has been extracted from the high-order polynomial model (see previous Chapters). For the PEDOT:PSS/$CH_3NH_3PbI_3$ configuration, in the orthorhombic phase k2 is equal for both temperatures (85K and 120 K) at $9.9x10^{-10}$ cm^3s^{-1}, while in tetragonal phase it decreases by an order of magnitude, from $1.3x10^{-9}$ cm^3s^{-1} to $1.2x10^{-10}$ cm^3s^{-1}, as the temperature increases from 120 K to 180 K. In the PTAA/$CH_3NH_3PbI_3$ architecture, in the orthorhombic phase, the k_2 decreases around by a factor 3, from $9.1x10^{-10}$ cm^3s^{-1} to $3.8x10^{-10}$ cm^3s^{-1}, as the temperature rises from 85 K to 120 K; and in tetragonal phase is decreased 6 times from $6.6x10^{-10}$ cm^3s^{-1} at 120 K to $1.0x10^{-10}$ cm^3s^{-1} at 180 K. Furthermore, another observation from **Table 6.1** shows, that PTAA/$CH_3NH_3PbI_3$ architecture reveal faster hole injection (τ_2) and slower bimolecular recombination rate (k_2) for all studied temperatures compared with the PEDOT:PSS/$CH_3NH_3PbI_3$ configuration, which is in agreement with our previous publication.[23]

Based on the above, the shorter hole injection and slower bimolecular recombination rate in case of PTAA are attributed to larger grains, and better energy alignment between the perovskite and the HTL, and in larger free charge carriers diffusion lengths, as we have already explained in **Chapter 4**. Also, we observe that the effect of the temperature on the obtained dynamics is notable for both HTL configurations, in agreement with Milot et al.[12]

where they have shown that the bimolecular recombination rate reduces as the temperature rises, as a result of electron-phonon interactions. In general, the bimolecular recombination rate (k_2) is expected to reduce with decreasing the charge-carrier mobility, because in affected by the average velocity of approach into the Coulomb capture radius. These results, reveal that the influence of the employing hole transport layer as well as the temperature is significant for the hole injection and for the bimolecular recombination rate, as well.

In summary, it was found that as the temperature increases from 85 K to 120K, thus moving from single orthorhombic towards the coexistence of orthorhombic and tetragonal phases, and from 120 K to 180 K (towards single tetragonal phase) the hole injection and the bimolecular recombination rate decrease, for both PEDOT:PSS/$CH_3NH_3PbI_3$ and PTAA/$CH_3NH_3PbI_3$ configurations. Moreover, even at low temperatures where the orthorhombic phase is present, the impact of the employing hole transport layer is critical, because it is found to strongly influence the charge carrier dynamics and the recombination rates, which are known to be directly related with the efficiency of the perovskite solar cells.

6.3 Conclusions

In this Chapter, in order to explore the uninvestigated area of the charge carrier dynamics at different phases of the perovskite film upon two different HTL polymers, the TAS measurements were performed at low variable temperature. In particular, in three studied temperatures, at 85 K (orthorhombic phase), at 120 K (coexistence of the orthorhombic and the tetragonal phase) for each peak, and at 180 K (tetragonal phase) the PTAA/MAPI architecture exhibits faster hole injection from the perovksite layer to the HTL and slower recombination rate (k_2) compared with the PEDOT:PSS/MAPI configuration. Moreover, as the temperature increases for each perovskite crystal phase (orthorhombic and tetragonal), the

τ_2 time components and k_2 bimolecular recombination rate decrease, for both configurations. Thus, it was found that the charge carrier dynamics in low temperature, is not only affected by the employing hole transport layer, as we have already shown for the room temperature measurements,[23] but are strongly touched and by the different perovskite crystal phases.

References:

1. Liu, Y.; Yang, Z.; Liu, S. Recent Progress in Single-Crystalline Perovskite Research Including Crystal Preparation, Property Evaluation, and Applications. *Adv. Sci.* **2018**, *5*, 1700471.
2. Poglitsch, A.; Weber, D. Dynamic Disorder in Methylammo-niumtrihalogenoplumbates (II) Observed by Millimeter-Wave Spectroscopy. *J. Chem. Phys*. **1987**, *87*, 6373-6378.
3. Wasylishen, R. E.; Knop, O.; Macdonald, J. B. Cation Rotation in Methylammonium Lead Halides. *Solid State Commun.* **1985**, *56*, 581-582.
4. Even, J.; Pedesseau, L.; Katan, C. Analysis of Multivalley and Multibandgap Absorption and Enhancement of Free Carriers Related to Exciton Screening in Hybrid Perovskites. J. *Phys. Chem. C* **2014**, *118*, 11566!11572.
5. D'Innocenzo, V.; Grancini, G.; Alcocer, M. J. P.; Kandada, A. R. S.; Stranks, S. D.; Lee, M. M.; Lanzani, G.; Snaith, H. J.; Petrozza, A. Excitons versus Free Charges in Organo-Lead Tri-Halide Perovskites. *Nat. Commun.* **2014**, *5*, 3586.
6. Yi, H. T.; Wu, X.; Zhu, X.; Podzorov, V. Intrinsic Charge Transport across Phase Transitions in Hybrid Organo-Inorganic Perovskites. *Adv. Mater*. **2016**, *28*, 6509-6514.
7. Chin, X. Y.; Cortecchia, D.; Yin, J.; Bruno, A.; Soci, C. Lead Iodide Perovskite Light-Emitting Field-Effect Transistor. *Nat. Commun.* **2015**, *6*, 7383.
8. Biewald, A.; Giesbrecht, N.; Bein, T.; Docampo, P.; Hartschuh, A.; Ciesielski, R. Temperature-Dependent Ambipolar Charge Carrier Mobility in Large-Crystal Hybrid Halide Perovskite Thin Films. *ACS Appl. Mater. Interfaces* **2019**, *11*, 20838-20844.
9. Etienne, T.; Mosconi, E.; De Angelis, F. Dynamical Origin of the Rashba Effect in Organohalide Lead Perovskites: A Key to Suppressed Carrier Recombination in Perovskite Solar Cells? J. *Phys. Chem. Lett.* **2016**, *7*, 1638-1645.
10. Eperon, G. E.; Jedlicka, E.; Ginger, D. S. Biexciton Auger Recombination Differs in Hybrid and Inorganic Halide Perovskite Quantum Dots. J. *Phys. Chem. Lett.* **2018**, *9*, 104-109.
11. Zhu, H.; Trinh, M. T.; Wang, J.; Fu, Y.; Joshi, P. P.; Miyata, K.; Jin, S.; Zhu, X. Y. Organic Cations Might Not Be Essential to the Remarkable Properties of Band Edge Carriers in Lead Halide Perovskites. *Adv. Mater.* **2017**, *29*, 1603072.
12. Milot, R. L.; Eperon, G. E.; Snaith, H. J.; Johnston, M. B.; Herz, L. M. Temperature-dependent charge-carrier dynamics in $CH_3NH_3PbI_3$ perovskite thin films. *Adv. Funct. Mater.* **2015**, *25*, 6218-6227.
13. Madjet, M. E.; Berdiyorov, G. R.; El-Mellouhi, F.; Alharbi, F. H.; Akimov, A. V.; Kais, S. Cation Effect on Hot Carrier Cooling in Halide Perovskite Materials. *J. Phys. Chem. Lett.* **2017**, *8*, 4439-4445.
14. Zhu, H.; Miyata, K.; Fu, Y.; Wang, J.; Joshi, P. P.; Niesner, D.; Williams, K. W.; Jin, S.; Zhu, X.-Y. Screening in Crystalline Liquids Protects Energetic Carriers in Hybrid Perovskites. *Science* **2016**, *353*, 1409-1413.
15. Chen, J.; Messing, M. E.; Zheng, K.; Pullerits, T. Cation- Dependent Hot Carrier Cooling in Halide Perovskite Nanocrystals. J. Am. Chem. Soc. **2019**, *141*, 3532-3540.
16. Diroll, B. T. Temperature-Dependent Intraband Relaxation of Hybrid Perovskites. *J. Phys. Chem. Lett.* **2019**, *10*, 5623-5628.
17. Varshni, Y. P. Temperature dependence of the energy gap in semiconductors. *Physica*, **1967**, *34*, 149-154.

18. Dar, M. I.; Jacopin, G.; Meloni, S.; Mattoni, A.; Arora, N.; Boziki, A.; Zakeeruddin, S. M.; Rothlisberger, U.; Grätzel, M. Origin of unusual bandgap shift and dual emission in organic-inorganic lead halide perovskites. *Sci. Adv.* **2016**, *2*, e1601156.
19. Baikie, T.; Fang, Y. N.; Kadro, J. M.; Schreyer, M.; Wei, F. X.; Mhaisalkar, S. G.; Grätzel, M.; White, T. J. Synthesis and crystal chemistry of the hybrid perovskite $(CH_3NH_3)PbI_3$ for solid-state sensitised solar cell applications. *J. Mater. Chem. A* **2013**, *1*, 5628-5641.
20. Even, J.; Pedesseau, L.; Katan, C.; Kepenekian, M.; Lauret, J. S.; Sapori, D.; Deleporte, E. (2015). Solid-state physics perspective on hybrid perovskite semiconductors. *J. Phys. Chem. C* **2015**, *119*, 10161-10177.
21. Even, J.; Pedesseau, L.; Jancu, J. M.; Katan, C. DFT and k·p modelling of the phase transitions of lead and tin halide perovskites for photovoltaic cells. *Phys. Status Solidi RRL* **2014**, *8*, 31-35.
22. Filippetti, A.; Delugas, P.; Saba, M. I.; Mattoni, A. Entropy-suppressed ferroelectricity in hybrid lead-iodide perovskites. *J. Phys. Chem. Lett.* **2015**, *6*, 4909-4915.
23. Serpetzoglou, E.; Konidakis, I.; Kakavelakis, G.; Maksudov, T.; Kymakis, E.; Stratakis, E. Improved Carrier Transport in Perovskite Solar Cells Probed by Femtosecond Transient Absorption Spectroscopy. *ACS Appl. Mater. Interfaces*, **2017**, *9*, 43910-43919.
24. Kakavelakis, G.; Maksudov, T.; Konios, D.; Paradisanos, I.; Kioseoglou, G.; Stratakis, E.; Kymakis, E. Efficient and Highly Air Stable Planar Inverted Perovskite Solar Cells with Reduced Graphene Oxide Doped PCBM Electron Transporting Layer. *Adv. Energy Mater.* **2016**, *7*, 1602120.
25. Ishioka, K.; Barker, B. G.; Yanagida, M.; Shirai, Y.; Miyano, K. Direct Observation of Ultrafast Hole Injection from Lead Halide Perovskite by Differential Transient Transmission Spectroscopy. *J. Phys. Chem. Lett.* **2017**, *8*, 3902.
26. Zhu, Z.; Ma, J.; Wang, Z.; Mu, C.; Fan, Z.; Du, L.; Yang B.; Fan L.; Yan H.; Phillips D. L.; Yang, S. Efficiency Enhancement of Perovskite Solar Cells Through Fast Electron Extraction: The Role of Graphene Quantum Dots. *J. Am. Chem. Soc.* **2014**, *136*, 3760.
27. Konidakis, I.; Maksudov, T.; Serpetzoglou, E.; Kakavelakis, G.; Kymakis. E.; Stratakis, E. Improved Charge Carrier Dynamics of $CH_3NH_3PbI_3$ Perovskite Films Synthesized by Means of Laser- assisted Crystallization. *ACS Appl. Energy Mater.* **2018**, *1*, 5101-5111.
28. Corani, A.; Li, M. H.; Shen, P. S.; Chen, P.; Guo, T. F.; El Nahhas, A.; Zheng, K.; Yartsev, A.; Sundstrom, V.; Ponseca Jr, C. S. Ultrafast Dynamics of Hole Injection and Recombination in Organometal Halide Perovskite Using Nickel Oxide as p-Type Contact Electrode. *J. Phys. Chem. Lett* **2016**, *7*, 1096.
29. Ghosh, T.; Aharon, S.; Etgar, L.; Ruhman, S. Free Carrier Emergence and Onset of Electron–Phonon Coupling in Methylammonium Lead Halide Perovskite Films. *J. Am. Chem. Soc.* **2017**, *139*, 18262.
30. Zhai, Y.; Sheng; C. X.; Zhang, C.; Vardeny, Z. V. Ultrafast Spectroscopy of Photoexcitations in Organometal Trihalide Perovskites. *Adv. Funct. Mater.* **2016**, *26*, 1617.

31. Serpetzoglou, E.; Konidakis, I.; Maksudov, T.; Panagiotopoulos, A.; Kymakis, E.; Stratakis, E. In-situ Monitoring of the Charge Carrier Dynamics of $CH_3NH_3PbI_3$ Perovskite Crystallization Process. *J. Mater. Chem. C* **2019**, *7*, 12170-12179.
32. Draguta, S.; Christians, J. A.; Morozov, Y. V.; Mucunzi, A.; Manser, J. S.; Kamat, P. V.; Luther, J. M.; Kuno, M. A Quantitative and Spatially Resolved Analysis of the Performance-Bottleneck in High Efficiency, Planar Hybrid Perovskite Solar Cells. *Energy Environ. Sci.* **2018**, *11*, 960.
33. Wehrenfennig, C.; Eperon, G. E.; Johnston, M. B.; Snaith, H. J.; Herz, L. M. High Charge Carrier Mobilities and Lifetimes in Organolead Trihalide Perovskites. *Adv. Mater.* **2014**, *26*, 1584.
34. Klein, J. R.; Flender, O.; Scholz, M.; Oum, K.; Lenzer, T. Charge Carrier Dynamics of Methylammonium Lead Iodide: from PbI_2-rich to Low-Dimensional Broadly Emitting Perovskites. *Phys. Chem. Chem. Phys*. **2016**, *18*, 10800.
35. Manser, J. S.; Kamat, P. V. Band Filling with Free Charge Carriers in Organometal Halide Perovskites. *Nat. Photonics* **2014** *8*, 737.
36. Stranks, S. D.; Burlakov, V. M.; Leijtens, T.; Ball, J. M.; Goriely, A.; Snaith, H. J. Recombination Kinetics in Organic-Inorganic Perovskites: Excitons, Free Charge, and Subgap States. *Phys. Rev. Appl.* **2014**, *2*, 034007.
37. Piatkowski, P.; Cohen, B.; Ramos, F. J.; Di Nunzio, M.; Nazeeruddin, M. K.; Grätzel, M.; Ahmad, S.; Douhal, A. Direct Monitoring of Ultrafast Electron and Hole Dynamics in Perovskite Solar Cells. *Phys. Chem. Chem. Phys*. **2015**, *17*, 14674.
38. La-o-vorakiat, C.; Salim, T.; Kadro, J.; Khuc, M. T.; Haselsberger, R.; Cheng, L.; Xia, H.; Gurzadyan, G. G.; Su, H.; Lam, Y. M.; Marcus, R. A.; Michel-Beyerle, M. E.; Chia, E. E. M. Elucidating the Role of Disorder and Free-Carrier Recombination Kinetics in $CH_3NH_3PbI_3$ Perovskite Films. *Nat. Commun*. **2015**, *6*, 7903.
39. He, J.; Fang, W. H.; Long, R. Weak Temperature-Dependent Hole Injection and Electron–hole Recombination at the $CH_3NH_3PbI_3$/NiO Heterojunction: A Time-Domain Ab Initio Study. *J. Mater. Chem. A* **2020**, *8*, 607-615.

Chapter 7

Future Plans

Future work will mainly focus on the fundamental mechanisms in the perovskite solar cells (PSCs), in 2D-TMD/perovskite and 2D-TMD/2d-TMD heterojunction photovoltaics. There are several ideas to be evaluated towards an in-depth understanding of the processes that take place in devices under photoexcitation, aiming to shed light on the charge carrier dynamics, resulting to improve the stability and the performance of the solar cells. A brief explanation of the basic future experimental work includes:

- Effect of the electron transport layer (ETL) in the perovskite solar cells. The main purpose of this idea is to explore the influence of the employing ETL to the performance of the PSCs and the correlation of the charge carrier dynamics with the electrical characteristics of the devices. For a complete study, we will explore the ultrafast phenomena in a typical TAS configuration, i.e. glass/FTO/ETL/perovskite and also in a complete planar inverted device, i.e. glass/ITO/HTL/perovskite/ETL. For the first case, we will be able to extract useful information about the electron injection from the perovskite to the ETL and the recombination of the electron and holes in the bulk perovskite and in the ETL/perovskite interface. Moreover, we will explore how the ETL affects these processes and influences the performance of the devices. For the latter architecture, we will be able to obtain useful information about the importance of the employing HTL and ETL and which of these layers is more crucial.
- TAS measurements in PSCs under operation conditions. The aim for this study is to fully understand and shed light on the degradation effect of the perovskite solar cells and how the operation conditions affect the charge carrier dynamics of the devices.

For this idea, we will perform TAS measurements, while at the same time we will illuminate the device under inert conditions with an Air Mass 1.5 Global (AM 1.5G) solar simulator at an intensity of 100 mW cm^{-2}. Thus, we will explore the evolution of the charge carrier dynamics of the devices and how these are degraded due to the continuous illumination.

- Charge carrier dynamics in 2D-TMD/perovskite and 2D-TMD/2D-TMD heterojunctions photovoltaic. The scope of this work is to study the charge carrier dynamics in in both configurations in order to shed light the complex processes that take place in the interface of the 2D-TMD material with the perovskite or in 2D-TMD/2D-TMD material, such as charge-carrier generation, extraction, transport and collection, each of affect the performance of the device.

Appendix

Exponential Fitting Analysis

As we have already discussed in the main text of this thesis, there are two well-established fitting models to fit our data. Herein, the detailed procedure to extract the error bars in the case of three-exponential are described. Firstly, we choose the appropriate equation and fitting model (*ExpDec3*). Before we fit our data, we narrow the range of τ_1 and τ_2 and y_0. Specifically, we narrow the time ranges for τ_1, τ_2, from 10 ps up to 30 ps and from 30 ps up to 200 ps, respectively, for both configurations in order to obtain fast and efficient hole injection from the perovskite layer to hole transport layer. Moreover, we narrow also the constant, y_0, of our equation between 0 and the lowest value of ΔOD, because in the time range of our setup is impossible not to have excited electrons in the conduction band of the perovskite layer.

Additionally, in **Table A1.1, Table *A1.2*** we present the further analysis at optimum annealing period at 90 ^{o}C for both configurations, showing that tri-exponential fitting model that we use, is the best fit for our data with the requirement that time decay components have fitted values lying within a physically explainable range. We have to mention that the same trend observed also for 100 ^{o}C and 110 ^{o}C for both architectures. Especially, in **Table A1.1, Table A1.2 (a)** we show the optimum fitting without any fixed term (fitting software internal algorithm provides best fit, only from a mathematical point of view). **Table A1.1, Table A1.2 (b)** present the time components in which the y_0 and τ_1 are fixed in the values from the optimum fitting. We obtain that the deviation of τ_2 and τ_3 is within the error that we have already presented in the revised manuscript. Moreover, **Table A1.1, Table A1.2 (c)** show the corresponding fitting when only τ_2 is fixed in the optimum value. With this

procedure, we take unrealistic τ_1 and τ_3 for the perovskite solar cell. Finally, in **Table A1.1, Table A1.2 (d, f)** we present the time components when the τ_3 is fixed with lower and higher compared with the τ_3 value extracting from the optimum value, respectively. In both cases the τ_2 value is too slow to present the hole injection from the perovskite to the hole transport layer.

(a) Model	ExpDec3
Equation	$y = A_1*\exp(-x/\tau_1) + A_2*\exp(-x/\tau_2) + A_3*\exp(-x/\tau_3) + y_0$
Plot	deltaOD
y_0	0.01753 ± 6.10E-4
τ_1	21.85 ± 1.89
τ_2	105.16 ± 7.45
τ_3	3.2E7 ± 12.60
Adj. R-Square	0.9983

(b) Model	ExpDec3
Equation	$y = A_1*\exp(-x/\tau_1) + A_2*\exp(-x/\tau_2) + A_3*\exp(-x/\tau_3) + y_0$
Plot	deltaOD
y_0	0.018 ± 0
τ_1	22 ± 0
τ_2	97.83 ± 6.45
τ_3	3.1E7 ± 4.89
Adj. R-Square	0.9983

(c) Model	ExpDec3
Equation	$y = A_1*\exp(-x/\tau_1) + A_2*\exp(-x/\tau_2) + A_3*\exp(-x/\tau_3) + y_0$
Plot	deltaOD
y_0	0.01298 ± 0.00637
τ_1	577.19 ± 7.1E6
τ_2	22 ± 0
τ_3	577.22 ± 6.36E6
Adj. R-Square	0.9958

(d) Model	ExpDec3
Equation	$y = A_1*\exp(-x/\tau_1) + A_2*\exp(-x/\tau_2) + A_3*\exp(-x/\tau_3) + y_0$
Plot	deltaOD
y_0	0.01303 ± 0.00379
τ_1	26.3 ± 1.3
τ_2	980.1 ± 422.1
τ_3	1.4E7 ± 0
Adj. R-Square	0.9982

(e) Model	ExpDec3
Equation	$y = A_1*\exp(-x/\tau_1) + A_2*\exp(-x/\tau_2) + A_3*\exp(-x/\tau_3) + y_0$
Plot	deltaOD
y_0	0.001835 ± 0.0013
τ_1	21.85 ± 1.96
τ_2	105.3 ± 7.94
τ_3	3.2E7 ± 0
Adj. R-Square	0.9983

(f) Model	ExpDec3
Equation	$y = A_1*\exp(-x/\tau_1) + A_2*\exp(-x/\tau_2) + A_3*\exp(-x/\tau_3) + y_0$
Plot	deltaOD
y_0	0.01507 ± 4.4E-4
τ_1	24.51 ± 1.54
τ_2	204.34 ± 13.59
τ_3	8.4E7 ± 0
Adj. R-Square	0.9983

Table A1.1: Fitting analysis at optimum annealing period at 90 °C for PEDOT:PSS/$CH_3NH_3PbI_3$ configuration, **(a)** the optimum fitting, **(b)** y_0 and τ_1 are fixed, **(c)** τ_2 is fixed, and **(d-f)** τ_3 is fixed.

(a) Model	ExpDec3
Equation	$y = A_1*\exp(-x/\tau_1) + A_2*\exp(-x/\tau_2) + A_3*\exp(-x/\tau_3) + y_0$
Plot	deltaOD
y_0	0.00758 ± 5.48E-4
τ_1	17.02 ± 1.95
τ_2	48.27 ± 7.85
τ_3	418.91 ± 12.60
Adj. R-Square	0.9978

(b) Model	ExpDec3
Equation	$y = A_1*\exp(-x/\tau_1) + A_2*\exp(-x/\tau_2) + A_3*\exp(-x/\tau_3) + y_0$
Plot	deltaOD
y_0	0.01 ± 0
τ_1	17 ± 0
τ_2	40.09 ± 2.79
τ_3	371.2 ± 2.3
Adj. R-Square	0.9977

(c) Model	ExpDec3
Equation	$y = A_1*\exp(-x/\tau_1) + A_2*\exp(-x/\tau_2) + A_3*\exp(-x/\tau_3) + y_0$
Plot	deltaOD
y_0	0.0055 ± 0.0029
τ_1	467.2 ± 8.1E5
τ_2	48 ± 0
τ_3	467.2 ± 7.4E5
Adj. R-Square	0.9971

(d) Model	ExpDec3
Equation	$y = A_1*\exp(-x/\tau_1) + A_2*\exp(-x/\tau_2) + A_3*\exp(-x/\tau_3) + y_0$
Plot	deltaOD
y_0	0.0053 ± 0.0025
τ_1	33.03 ± 1.2
τ_2	575.9 ± 132.9
τ_3	250 ± 0
Adj. R-Square	0.9977

(e) Model	ExpDec3
Equation	$y = A_1*\exp(-x/\tau_1) + A_2*\exp(-x/\tau_2) + A_3*\exp(-x/\tau_3) + y_0$
Plot	deltaOD
y_0	0.00758 ± 1.3E-4
τ_1	17.02 ± 4.81
τ_2	48.29 ± 5.10
τ_3	419 ± 0
Adj. R-Square	0.9978

(f) Model	ExpDec3
Equation	$y = A_1*\exp(-x/\tau_1) + A_2*\exp(-x/\tau_2) + A_3*\exp(-x/\tau_3) + y_0$
Plot	deltaOD
y_0	0.0046 ± 0.0011
τ_1	32.61 ± 1.35
τ_2	239.96 ± 40.24
τ_3	600 ± 0
Adj. R-Square	0.9977

Table A1.2: Fitting analysis at optimum annealing period at 90 °C for PTAA/$CH_3NH_3PbI_3$ configuration, **(a)** the optimum fitting, **(b)** y_0 and τ_1 are fixed, **(c)** τ_2 is fixed, and **(d-f)** τ_3 is fixed.

In order to eliminate any doubts about the fitting uncertainties in **Table A1.3Table A1.4** we present the lower and upper limit for each time component for both configuration. In case of PEDOT:PSS/$CH_3NH_3PbI_3$ architecture the errors for the τ_1, τ_2 and τ_3 are 2 ps, 8 ps and 0.5E7 ps, respectively. While in case of PTAA/$CH_3NH_3PbI_3$ configuration the errors for the τ_1, τ_2 and τ_3 are 2 ps, 8 ps and 13 ps, respectively. Within these limits we obtain values for time components that are reasonable for the operation of the perovskite solar cell. Firstly, we initiate an upper and a lower limit of τ_1 at values that are physically explainable. The lower and upper limit of τ_1 take values for τ_2 and τ_3. If they are not realistic, we further reduce the upper and lower limits of τ_1, until we reach the value range of τ_1 that gives realistic results for τ_2, τ_3. So, the τ_1 value gives me the error for τ_2 and τ_3 time components. In this way, we have an empirical adaptation that has a physical explanation and is actually shifted.

	Lower Limit	Upper Limit
y_0	Fixed at 0.01753	
τ_1	21 ps	24 ps
τ_2	97 ps	113 ps
τ_3	2.7E7 ps	3.5E7 ps

Table A1.3: Lower and Upper Limits for time components for PEDOT:PSS/$CH_3NH_3PbI_3$ architecture.

	Lower Limit	Upper Limit
y_0	Fixed at 0.0075	
τ_1	15 ps	19 ps
τ_2	40 ps	56 ps
τ_3	407 ps	431 ps

Table A1.4: Lower and Upper Limits for time components for PTAA/$CH_3NH_3PbI_3$ architecture.